Dalitz Analysis of D0 to K0(S) Pi+ Pi- and Measurement of the CKM Angle Gamma in Charged B+- Decays to D(*) K+- Decays

Ben Y.P. Lau

SLAC-R-872

Prepared for the Department of Energy
under contract number DE-AC02-76SF00515

Dalitz analysis of $D^0 \rightarrow K_S^0\pi^+\pi^-$ and measurement of the CKM angle γ in $B^\pm \rightarrow D^{(*)}K^\pm$ decays

Ben Y.P. Lau

A DISSERTATION PRESENTED TO THE FACULTY
OF PRINCETON UNIVERSITY
IN CANDIDACY FOR THE DEGREE
OF DOCTOR OF PHILOSOPHY

RECOMMENDED FOR ACCEPTANCE
BY THE DEPARTMENT OF PHYSICS

November 2006

Introduction

Despite more than thirty years having elapsed since the discovery of *CP* violation, our understanding about the source and the nature of this phenomenon is still very limited. In the standard model of particle physics, *CP* violation is due to the presence of an non-irreducible weak phase in the Cabibbo-Kabayashi-Maskawa(CKM) matrix. Up to now, all the experimental results are in good agreement with the standard model. However, it is important for us to over-constrain the CKM quark-mixing matrix and explore the possibility of new physics beyond the standard model. The B meson provides an ideal place to measure *CP* violation due to its heavy mass and potentially large *CP*-violating effects. In particular, the angle γ of the Unitary Triangle relating the elements of the CKM matrix is extremely crucial in terms of *CP* violation and constraints on the new physics models.

Various methods using $B^- \to D^0 K^-$ decays have been proposed to measure γ based on the interference between the V_{cb} and V_{ub} amplitudes. Despite the simple concept, the measurement turns out to be experimentally challenging due to the small branching fraction and the small value of r_B, the amplitude ratio between the two contributing Feynman diagrams.

In this thesis a novel technique to measure γ in $B^- \to D^{(*)} K^-$ decay using a Dalitz plot analysis of $D^0 \to K_s \pi^+ \pi^-$ is presented. Until the turn on of LHC_b [1]

later in the decade, this remains the most promising method to measure γ.

This thesis is roughly separated into two parts. The first part involves a study of hadron spectroscopy and the Dalitz plot analysis of the $D^0 \rightarrow K_S^0\pi^+\pi^-$. The second part of the thesis involves the measurement of γ in $B^- \rightarrow D^{(*)}K^-$ using the results of the $D^0 \rightarrow K_S^0\pi^+\pi^-$dalitz plot analysis.

Acknowledgements

I am gratefuly to all the people who have helped me in numerous ways to complete this work.

First, I must thank my thesis advisor, Prof. Stew Smith and Jim Olsen. This thesis work would not have been possible without their patient guidance. I was fortunate to have Stew as my advisor during my five years here, as he gave me a lot of freedom to do whatever I like and he will help me whenever I had any difficulties.

Jim Olsen has been another mentor to me. Under his guidance, I not only learnt how to do an analysis, but also the importance of the critical thinking. His famous motteo: “Don’t trust anyone, and even don’t trust yourself” has a great impact on me.

The measurements presented in this thesis are the results of many close collaboration of many people, including Gianluca Cavoto, Marcello Giorgi, Luigi Li Gioi, Fernando Martinez-Vidal, Nicola Neri, Jim Olsen, Elisabetta Prencipe, Matteo Rama, Marie-Helene Schune and Achille Stocchi. I must thank Fernando Martinez-Vidal in particular as he made significant contribution to this analysis, and we had a wonderful collaboration together.

In particular, I must thank Gianluca Cavoto (INFN Roma), Achille Stocchi and Marie-Helene Schune (LAL Orsay), and Fernando Martinez (IFIC Spain) for their kind hospitality during the visit in year 2004 and year 2005, where we had excellent joint collaboration and fun time together.

I am very grateful to Prof. Mike Pennington who taught me a lot of physics in hadron spectroscopy. I will never forget our fruitful discussion in the *BABAR* dalitz workshop in 2004. I thank Prof. Andrey Sarantsev who provided me many inputs on the K-matrix theory and results. I thank for Jinwei Wu for his early guidance on the subject on Dalitz plot. I also thank for Antimo Palano, Brian Meadows and Marco Pappagallo where we had lengthy discussion on the scalar mesons.

There have been several people affiliated with my study in graduate school at Princeton. TingFai Ng, Francis Tam and Jones Wan, are my best friends in Princeton, and I am continually grateful for their friendships and the conversations we had about science, careers, and life. I will always remembered our times in small world coffee at Princeton and the wonderful times together in our apartment at Lawrenceville.

I have also learned a lot from many current and former Princeton colleagues at SLAC. Jed Beidiesa, Nick Danielson, Sasha Telnov, where I had a chance to learn more about the culture in US, and boarden my horizon outside physics.

Many other faculty have been great teachers and friends over the years—Kam-Biu Luk from University of California, Berkeley and Bob Mckeown, from California Institute of Technology, has arise my interest in particle physics. Hon-Ming Lai and Ming-Chung Chu, from Chinese University of Hong Kong, were my advisors during my undergraduate studies.

I must also thank to all my friends where I met at Princeton and Stanford. I am continually grateful for the friendships, the support and encouragment during my years at Stanford and Princeton.

Finally, my family has been of the utmost importance to me. Thanks for my parents for their kind understanding, their love and the support.

Contents

1 *CP* violation in the standard model **1**

1.1 Overview of *CP* violation 1

1.1.1 *CP* violation in the standard model 2

1.1.2 Three types of *CP* violation 4

1.2 Measuring $\boldsymbol{\gamma}$ in $\boldsymbol{B^- \rightarrow D^0 K^-}$ decays 11

1.2.1 The GLW method 12

1.2.2 The ADS method 14

1.2.3 The Dalitz method 15

1.3 CKM γ and constraints on new physics 18

2 The PEP-II and *BABAR* Detector **20**

2.1 Overview 20

2.2 PEP-II and the *BABAR* Detector 21

2.3 Overview of *BABAR* detector 22

2.4 Silicon Vertex Tracker(SVT) 25

2.5 Drift Chamber(DCH) 29
2.6 Detector of Internally Reflected Cherenkov Light(DIRC) 33
2.7 Electromagnetic Calorimeter(EMC) 36
2.8 Instrumented Flux Return(IFR) 40

3 Hadron Spectroscopy 47

3.1 Outline 47
3.2 Introduction to Dalitz plot 48
3.3 BW lineshape 50
  3.3.1 Non-relativistic BW – time dependence 51
  3.3.2 Matrix element $|\mathcal{M}|$ from field theory approach 52
3.4 Relativistic BW propagators 53
3.5 Spin Formalism 55
  3.5.1 Zemach Tensor vs Helicity model 57
3.6 Blatt-Weisskopf penetration factors 60
3.7 Hadron Spectroscopy and K-matrix Theory 61
  3.7.1 K-matrix theory 62
  3.7.2 P-vector formalism 67
3.8 K-matrix examples 68
3.9 Model dependence of BW parameters 77

4 $D^0 \to K_S^0\pi^+\pi^-$Dalitz plot analysis **85**

4.1 Introduction 85

4.2 $D^0 \to K_S^0\pi^+\pi^-$ selection 87

4.3 Background composition 89

4.3.1 Dalitz background parameterization 92

4.4 Efficiency and momentum resolution 94

4.4.1 Efficiency 94

4.4.2 Mass resolution 94

4.5 Decay Amplitude 96

4.5.1 The Isobar model 96

4.5.2 The K-matrix Model 98

4.6 Likelihood function and fit procedure 105

4.7 Results 106

4.7.1 Isobar Model 106

4.7.2 The K-matrix Model 107

5 Analysis of $B^- \to D^{(*)}K^-$ decays **113**

5.1 Introduction 113

5.2 $B^- \to D^{(*)0}K^-$ Selection 114

5.2.1 Comparison of data and Monte Carlo 115

5.3 Background composition 117

5.3.1 Background from $e^+e^- \to q\bar{q}$ continuum light-quark 118

5.3.2 Background from $B \to D\pi$ decays 120

5.3.3 Background from $B \to 4\pi$ 121

5.3.4 Real D^0 from $e^+e^- \to c\bar{c}$ 122

5.3.5 Random flavor-tagging kaon for signal events 124

5.4 $B^- \to D^0\pi^-$ as control sample 124

5.5 Efficiency over the Dalitz plot 125

5.6 Background Dalitz shape 127

5.7 Likelihood fit procedure 128

5.7.1 Signal yield determination 130

6 Measurement of γ in $B^- \to D^{(*)}K^-$ decays **134**

6.1 Introduction 134

6.2 The Dalitz PDF 135

6.2.1 Cartesian vs. polar coordinates 135

6.2.2 Modification of PDF for D^*K events 137

6.3 Sensitivity to γ accross the Dalitz plot 139

6.4 Fits to control samples 140

6.5 Results of CP parameters 142

6.5.1 Frequentist interpretation 144

6.6 Experimental systematic uncertainties 146

6.6.1 General systematics from shape variables 147

6.6.2 Background composition 149

6.6.3 Systematics from Dalitz shapes 149

6.6.4 Other systematics 150

6.6.5 Systematics from the Dalitz model 151

6.7 Dalitz model systematic uncertainties 152

6.7.1 The procedure to determine the model systematics 154

7 Summary and Future Outlook 158

7.1 Constraint on the ($\bar{\rho}$, $\bar{\eta}$) plane 158

7.2 Future outlook 161

7.2.1 Future improvements 161

7.3 Conclusion 164

A Miscellaneous Formulae 167

A.1 Breit-Wigner – partial wave phase shifts 167

A.2 Gounaris-Sakurai(GS) parameterization 168

A.3 Modification of PDF for DK^* events 169

Chapter 1

CP violation in the standard model

1.1 Overview of *CP* violation

Despite the fact that *CP* violation was first discovered in 1964 in K-meson decays [2], the source and the nature of this phenomenon remains one of the open problems in particle physics. The abbreviation *CP* stands for simultaneous charge conjugation C and parity reversal P operations. Charge conjugation interchanges particles with antiparticles, while parity P reverses space coordinates $(t, \overrightarrow{x}) \rightarrow (t, -\overrightarrow{x})$. In fact, discovery of *CP* violation, despite being a small effect 10^{-3}, was clearly visible in the early kaon experiments. Even larger effects were expected, and confirmed, in the B system.

In the standard model, *CP* violation arises from the presence of an irreducible phase in the Cabibbo-Kobayashi-Maskawa(CKM) quark-mixing matrix. However, there are 18 unknown parameters in the standard model which cannot be calculated from field theory and must be measured experimentally[3]. Due to its large mass and potentially large *CP*-violating effects, B mesons provide an ideal system to constrain the standard model.

1.1.1 *CP* violation in the standard model

The standard model electroweak Hamiltonian can be written as:

$$H_W = -\frac{g}{\sqrt{2}}(\bar{u}_L, \bar{c}_L, \bar{t}_L)\gamma^\mu V_{CKM} \begin{pmatrix} d_L \\ s_L \\ b_L \end{pmatrix} W_\mu^\dagger + h.c., \tag{1.1}$$

where V_{CKM} is the Cabibbo-Kobayashi-Maskawa matrix:

$$V_{CKM} = \begin{pmatrix} V_{ud} & V_{us} & V_{ub} \\ V_{cd} & V_{cs} & V_{cb} \\ V_{td} & V_{ts} & V_{tb} \end{pmatrix}. \tag{1.2}$$

There are various ways to parameterize this matrix. In the standard form there are just three generalized Cabibbo angles $(\theta_1, \theta_2, \theta_3)$ and one phase factor δ

$$V_{CKM} = \begin{pmatrix} c_1 & s_1c_3 & s_1s_3 \\ -s_1c_2 & c_1c_2c_3 - s_2s_3e^{i\delta} & c_1c_2s_3 + s_2c_3e^{i\delta} \\ -s_1s_2 & c_1s_2c_3 + c_2s_3e^{i\delta} & c_1s_2s_3 - c_2c_3e^{i\delta} \end{pmatrix}, \tag{1.3}$$

where c_i stands for $\cos\theta_i$ and s_i stands for $\sin\theta_i$. Although this is the original form of the CKM parameterization, the physics is more transparent in the following less well-known form:

$$V_{CKM} = \begin{pmatrix} 1 & 0 & 0 \\ 0 & c_2 & -s_2 \\ 0 & s_2 & c_2 \end{pmatrix} \begin{pmatrix} c_1 & -s_1 & 0 \\ s_1 & c_1 & 0 \\ 0 & 0 & 1 \end{pmatrix} \begin{pmatrix} 1 & 0 & 0 \\ 0 & 1 & 0 \\ 0 & 0 & -e^{i\delta} \end{pmatrix} \begin{pmatrix} 1 & 0 & 0 \\ 0 & c_3 & s_3 \\ 0 & -s_3 & c_3 \end{pmatrix}, \tag{1.4}$$

which can be viewed as a product of Eulerian rotation matrices and an irreducible phase matrix. The explicit dependence on δ corresponds to *CP* violation in the standard model. Since V_{CKM} is unitary, $VV^\dagger = 1$, we have

$$\sum_i V_{ij} V^*_{ik} = 0. \tag{1.5}$$

There are six such equations, each representing a triangle in the complex plane. Two of these equations have sides of similar magnitude:

$$V_{ud}V^*_{ub} + V_{cd}V^*_{cb} + V_{td}V^*_{tb} = 0, \tag{1.6}$$

$$V_{ud}V^*_{td} + V_{us}V^*_{ts} + V_{ub}V^*_{tb} = 0. \tag{1.7}$$

The most popular parameterization used is the so-called Wolfenstein parameterization[4], which consists of four parameters (λ, A, ρ, η) with λ as the expansion parameter:

$$V_{CKM} = \begin{pmatrix} 1-\lambda^2/2 & \lambda & A\lambda^3(\rho - i\eta) \\ -\lambda & 1-\lambda^2/2 & A\lambda^2 \\ A\lambda^3(1-\rho-i\eta) & -A\lambda^2 & 1 \end{pmatrix} + O(\lambda^4). \tag{1.8}$$

Here, $\lambda = \sin\theta \approx 0.22$ and θ is the Cabibbo angle. The parameters A, ρ and η are real numbers of order unity. A non-zero value for η is required for breaking of CP symmetry in the standard model. With the Wolfenstein parameterization, Eq. 1.7 can be represented as a triangle in the complex (ρ,η) plane, as shown in Fig. 1.1.

The three angles of the Unitary Triangle are denoted by α, β and γ:

$$\alpha \equiv arg\left[-\frac{V_{td}V_{tb}^*}{V_{ub}V_{ub}^*}\right], \quad \beta \equiv arg\left[-\frac{V_{cd}V_{cb}^*}{V_{td}V_{tb}^*}\right], \quad \gamma \equiv arg\left[-\frac{V_{ud}V_{ub}^*}{V_{cd}V_{cb}^*}\right], \tag{1.9}$$

and the lengths of the two complex sides are

$$R_b \equiv \sqrt{\bar{\rho}^2 + \bar{\eta}^2} = \frac{1-\lambda^2/2}{\lambda}\frac{|V_{ub}|}{|V_{cb}|}, \qquad R_t \equiv \sqrt{(1-\bar{\rho}^2) + \bar{\eta}^2} = \frac{1}{\lambda}\frac{|V_{td}|}{|V_{cb}|}. \tag{1.10}$$

1.1.2 Three types of *CP* violation

There are three types of *CP* violation observable in B decays, namely:

- *CP* violation in decay;

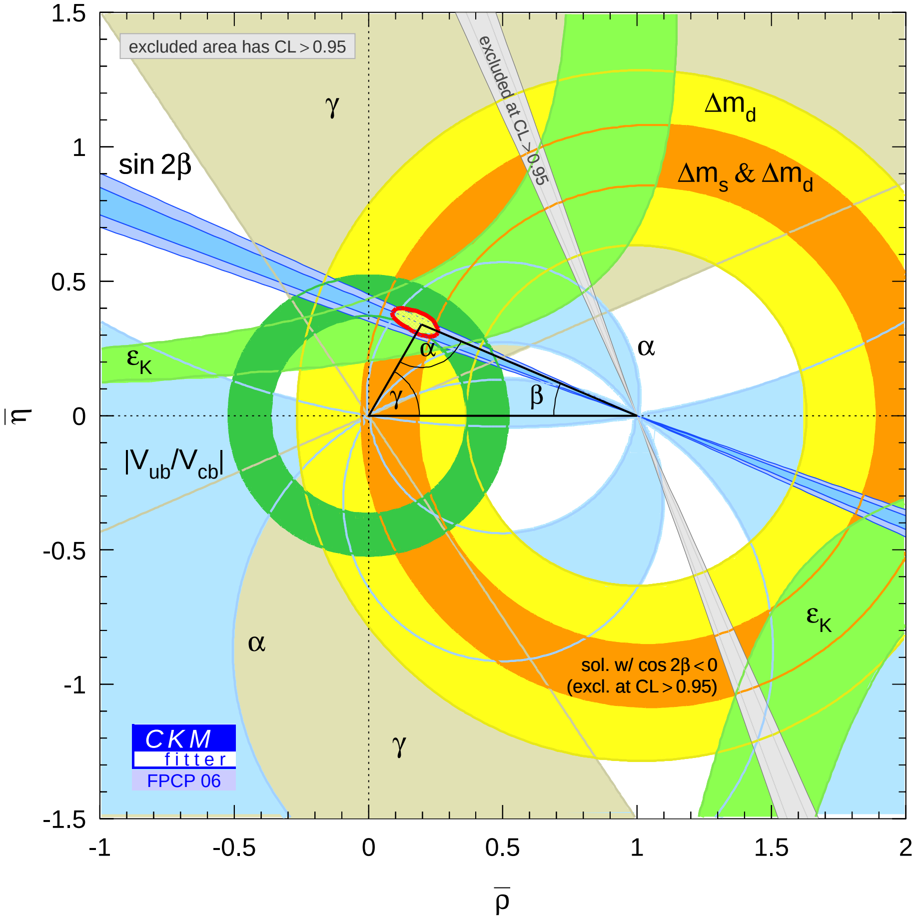

Figure 1.1: The Unitary Triangle, the color bands correspond to experimental constrains on $\bar{\rho}$ and $\bar{\eta}$ plane.

- CP violation in mixing;
- CP violation in the interference between decays with and without mixing.

Each type of CP violation is explained in detail below.

CP violation in decay

CP violation in decay, often referred to as direct *CP* violation, measures the difference in the decay rates for a particle and an antiparticle to the corresponding charge-conjugate final states:

$$A_{CP} \equiv \frac{\mathcal{B}(\bar{B} \to \bar{f}) - \mathcal{B}(B \to f)}{\mathcal{B}(\bar{B} \to \bar{f}) + \mathcal{B}(B \to f)}. \tag{1.11}$$

This type of *CP* violation is possible only if at least two different amplitudes contribute to the overall decay rate and they have non-zero relative weak and strong phase. Historically, Direct *CP* violation was first observed in neutral-kaon decays[5][6][7][8] at the level of a few parts per million, and recently has been observed in neutral B-meson decays to the $K\pi$ final state [9] at a much higher level ($|A_{CP}| = 0.13 \pm 0.03$). Fig 1.2 shows the m_{ES} distribution for the $K^+\pi^-$ (solid histogram) and $K^-\pi^+$ (dashed histogram) from the *BABAR* analysis.

CP violation in mixing

The other two types of *CP* violation involve $B^0 - \bar{B}^0$ mixing. The first one, *CP* violation via mixing, often referred to as indirect *CP* violation, results from second-

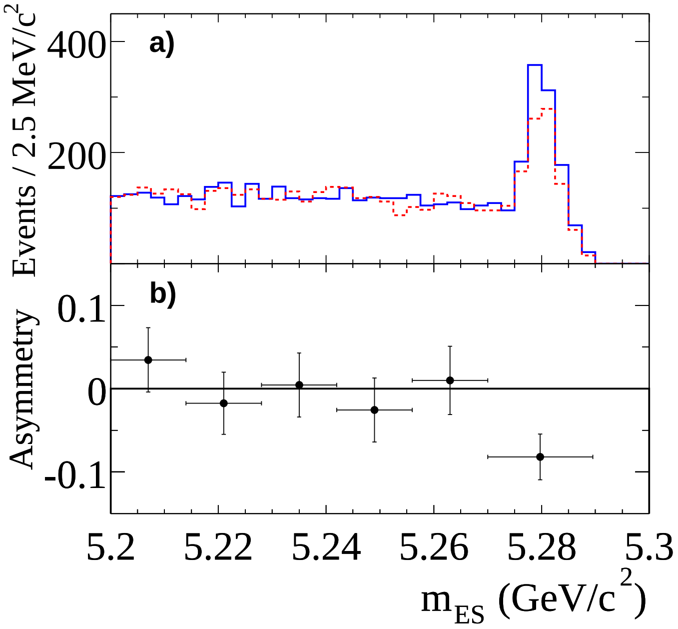

Figure 1.2: (a) Distribution of m_{ES} enhanced in $K^+\pi^-$ (solid histogram) and $K^-\pi^+$ (dashed histogram). (b) Asymmetry $\mathcal{A}_{K\pi}$ calculated for ranges of m_{ES}. The asymmetry in the highest m_{ES} bin is somewhat diluted by the presence of background.

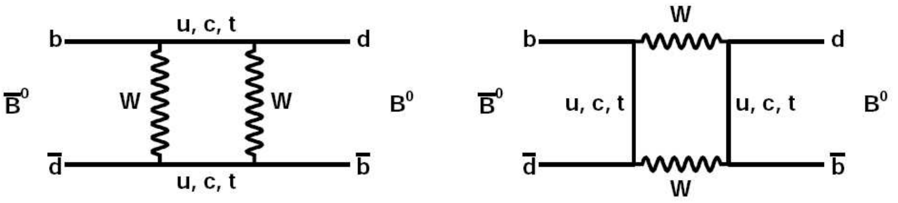

Figure 1.3: Second-order weak processes that gives rise to $B^0 - \bar{B}^0$ mixing

order weak processes such as those shown in Fig. 1.3. The B^0 and $\bar{B}^0$ mesons, which are flavor eigenstates, are not mass eigenstates. If we denote the mass eigenstates by B_H and B_L, they are linear superpositions of the flavor eigenstates:

$$\begin{aligned} |B_L\rangle &= p|B^0\rangle + q|\bar{B}^0\rangle && (1.12) \\ |B_H\rangle &= p|B^0\rangle - q|\bar{B}^0\rangle, && (1.13) \end{aligned}$$

where p and q are complex coefficients satisfying the normalization condition $|p|^2 + |q|^2 = 1$. The time evolution of an arbitrary linear combination of the flavor eigenstates

$$a|B^0\rangle + b|\bar{B}^0\rangle \qquad (1.14)$$

can be described by the time-dependent Schrödinger equation:

$$i\frac{d}{dt}\begin{pmatrix} a \\ b \end{pmatrix} = H\begin{pmatrix} a \\ b \end{pmatrix} \equiv \begin{pmatrix} H_{11} & H_{12} \\ H_{21} & H_{22} \end{pmatrix}\begin{pmatrix} a \\ b \end{pmatrix} \equiv \left(M - \frac{i}{2}\Gamma \right)\begin{pmatrix} a \\ b \end{pmatrix}, \qquad (1.15)$$

where M and Γ are 2×2 Hermitian matrices that originate from mixing and decay, respectively. Note that CPT invariance guarantees $H_{11} = H_{22}$, while the elements H_{12} and H_{21} are particularly important for *CP* violation, since they are the amplitudes for mixing and they are zero if there is no $B^0 - \bar{B}^0$ mixing. Furthermore, *CP* symmetry requires $\frac{|q|}{|p|} = 1$. Consequently, there is *CP* violation in mixing if $\frac{|q|}{|p|} \neq 1$. The current world average of the asymmetry measurements gives [10]

$$\left|\frac{q}{p}\right| = 1.0013 \pm 0.0034, \tag{1.16}$$

which is consistent with unity. *CP* violation in mixing is expected to be small $O(10^{-3})$ since it involves second-order weak processes.

CP violation between mixing and decay

The final form of *CP* violation arises from interference between mixing and decay processes. For example, this can be observed in decay of either B^0 and $\bar{B}^0$ to the same final state, which is a *CP* eigenstate ($f = \bar{f}$). If we define A_f to be the amplitude of the decay $B^0 \to f$ and $\bar{A}_f$ to be the amplitude of the decay $\bar{B}^0 \to \bar{f}$, the time-dependent asymmetry is

$$\begin{aligned} A_{CP}(t) &= \frac{\Gamma(\bar{B}^0 \to f_{CP})(t) - \Gamma(B^0 \to f_{CP})(t)}{\Gamma(B^0 \to f_{CP})(t) + \Gamma(\bar{B}^0 \to f_{CP})(t)} \\ &= \frac{2Im(\lambda_f)}{1+|\lambda_f|^2} \sin \Delta m_B t - \frac{1-|\lambda_f|^2}{1+|\lambda_f|^2} \cos \Delta m_B t \\ &= S \sin(\Delta m \Delta t) - C \cos(\Delta m \Delta t), \end{aligned} \tag{1.17}$$

where $\lambda_f = \frac{q}{p}\frac{\bar{A}}{A_f}$. The cosine term arises from direct *CP* violation and it vanishes if $|\lambda_f| = 1$. The sine term is due to interference between decays with and without mixing and it vanishs if $Im(\lambda_f) = 0$. The classic example is the decay channel in $B^0 \to J/\psi K_S$, since it proceeds mainly via the tree diagram and there is negligible contribution from *CP* violation in decay. Therefore, we expect $|\lambda_f| = 1$ and *CP* violation only arises from the sine term, $Im(\lambda_{J/\psi K_S})$. Hence,

$$\begin{aligned} Im(\lambda_{J/\psi K_S}) &= \sin 2\beta, \text{ and} \quad (1.18) \\ A_{CP}(t) &= \sin 2\beta \sin \Delta m_B t. \quad (1.19) \end{aligned}$$

Both *BABAR* [11] and Belle [12] collaborations have measured $\sin 2\beta$ using a combination of charmonium modes including $J/\psi K_S$. The latest results are as follow [1]:

$$\begin{aligned} \sin 2\beta &= 0.722 \pm 0.040 \pm 0.023 \qquad \text{BaBar} \quad (1.20) \\ \sin 2\beta &= 0.652 \pm 0.039 \pm 0.020 \qquad \text{Belle} \quad (1.21) \\ \sin 2\beta &= 0.685 \pm 0.028 \qquad \text{HFAG average} \quad (1.22) \end{aligned}$$

The non-zero value of $\sin 2\beta$ clearly establishes *CP* violation in B-meson decays. Fig. 1.4 shows the time-dependent *CP* violation for charmonium decays based on 232 million $B\overline{B}$ pairs collected by the BaBar detector at SLAC.

---

[1] Latest update: HFAG Winter 2006 results.

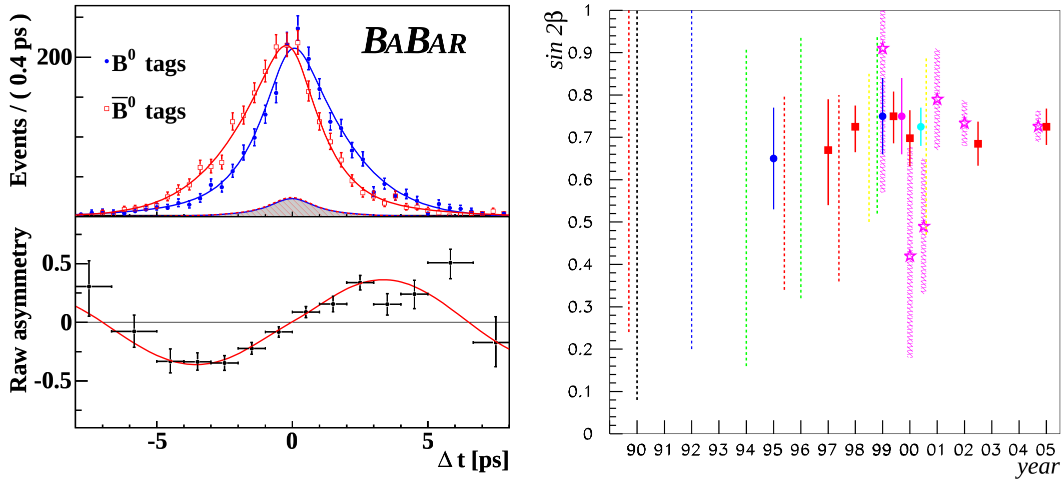

Figure 1.4: **Left:** The time-dependent *CP* violation for charmonium decays based on 232 million $B\overline{B}$ pairs collected by the BaBar detector at SLAC. **Right:** The evolution of $\sin 2\beta$. This parameter was unknown prior to 1995, but 10 years later it is a precision measurement. [13]

1.2 Measuring γ in $B^- \to D^0 K^-$ decays

The measurement of γ is often regarded as being very difficult from an experimental point of view. Nevertheless, it can be measured using interference in the decay amplitudes of the channels $B^+ \to D^0 K^+$ and $B^+ \to \overline{D}^0 K^+$, [2] as they are proportional to the CKM elements V_{ub} and V_{cb} and sensitive to the weak phase $\gamma = arg(\frac{V^*_{ub}V_{cs}}{V^*_{cb}V_{us}})$. Figure 1.5 shows the corresponding Feynman diagram for the $b \to c\overline{u}s$ and $b \to u\overline{c}s$ processes. The amplitude for $B^+ \to D^0 K^+$ decay is suppressed with respect to the amplitude of $B^+ \to \overline{D}^0 K^+$, as the ratio between the two amplitudes, is small due to

---

[2] Charge-conjugate modes are implied thought-out this thesis.

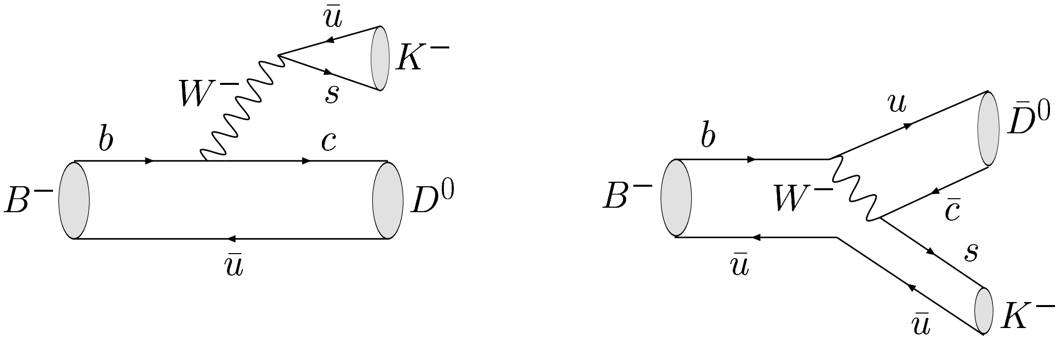

Figure 1.5: Diagrams contributing to $B^- \to D^0 K^-$ decay. The left diagram proceeds via $b \to c\overline{u}s$ transition, while the right diagram proceeds via $b \to u\overline{c}s$ transition and is both doubly-Cabibbo and color suppressed.

the CKM factors:

$$\frac{|V_{ub}^* V_{cs}|}{|V_{cb}^* V_{us}|} \approx 0.39. \tag{1.23}$$

If we define the quantity r_B as the ratio between the two amplitudes:

$$r_B = \left| \frac{A(B^+ \to D^0 K^+)}{A(B^+ \to \overline{D}^0 K^+)} \right|, \tag{1.24}$$

the expected value from current measurements is approximately 0.1. Different methods have been proposed for the measurement of γ using the interference of the channel in $b \to c\overline{u}s$ and $b \to u\overline{c}s$, the most common one are the GLW, ADS, and the Dalitz method.

1.2.1 The GLW method

The Gronau-London-Wyler (GLW) method [14] is the first method proposed to measure γ using $B^- \to D^0 K^-$ decay. This method uses the decay $B^\pm \to D^0_\pm K^\pm$, where

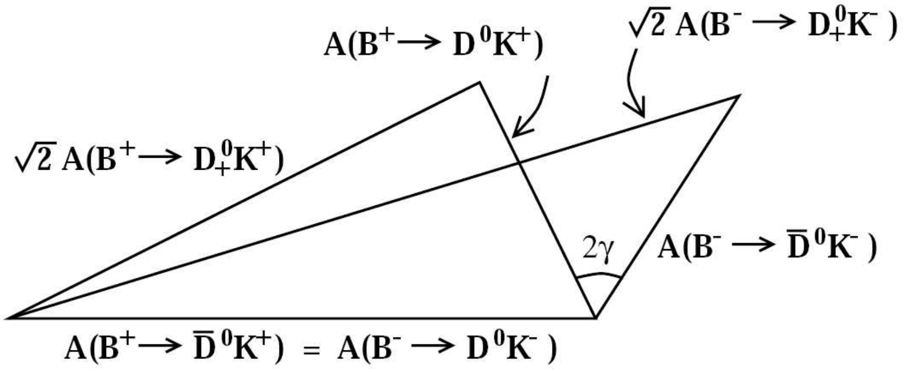

Figure 1.6: Triangle relations among $B^- \to D^0K^-$decay amplitude.

$D^0_\pm$ decay into *CP* eigenstates. They are reconstructed from final states with even *CP* like $\pi^+\pi^-$ and K^+K^-, or odd *CP* like $K^0_S\pi^0$. As the *CP* eigenstate $|D^0_\pm\rangle$ of the neutral D meson system with *CP* eigenvalues ±1 is given by

$$|D^0_\pm\rangle = \frac{1}{\sqrt{2}}(|D^0\rangle \pm |\overline{D}^0\rangle), \tag{1.25}$$

the $B^\pm \to D^0_+K^\pm$ amplitudes can be expressed as

$$\sqrt{2}A(B^+ \to D^0_+K^+) = A(B^+ \to D^0K^+) + A(B^+ \to \overline{D}^0K^+) \tag{1.26}$$

$$\sqrt{2}A(B^- \to D^0_+K^-) = A(B^- \to \overline{D}^0K^-) + A(B^- \to D^0K^-). \tag{1.27}$$

These relations, which are exact, can be represented as two triangles in the complex plane. To measure γ with this technique, one would measure the following four quantities.

$$
\begin{aligned}
R_{CP^\pm} &= \frac{\Gamma(B^+ \to D^0_{CP^\pm}K^+) + \Gamma(B^- \to D^0_{CP^\pm}K^-)}{\Gamma(B^+ \to D^0K^+) + \Gamma(B^- \to \overline{D}^0K^-)} \qquad (1.28)\\
&= 1 + r_B^2 \pm 2r_B^2 \cos\gamma\cos\delta_B\\
A_{CP^\pm} &= \frac{\Gamma(B^+ \to D^0_{CP^\pm}K^+) - \Gamma(B^- \to D^0_{CP^\pm}K^-)}{\Gamma(B^+ \to D^0K^+) + \Gamma(B^- \to \overline{D}^0K^-)} \qquad (1.29)\\
&= 2r_B \sin\gamma \sin\delta_B / R_{CP^\pm}.
\end{aligned}
$$

Here, r_B and δ_B are the amplitude and strong phase difference between the $b \to c$ and $b \to u$ amplitudes. The main disadvantage of the GLW method is the low overall branching fraction of these decays, and the eight-fold ambiguity in γ.

1.2.2 The ADS method

The Atwood-Dunietz-Soni (ADS) method [15] uses the $B^+ \to D^0K^+$ and $B^+ \to \overline{D}^0K^+$ decays, with the D^0 decaying into flavor eigenstates. Either it can be decayed via the color allowed B decay followed by the doubly- Cabibbo-suppressed(DCS)D decay, or via color-suppressed B decay followed by the Cabibbo-allowed(CAD) D decay. In this way, one can look at the interference between two amplitudes having the same order of magnitude. Experimentally, one would like to measure the R_{ADS}

and A_{ADS}, defined as:

$$\begin{aligned} R_{ADS} &= \frac{\Gamma(B^- \to [f]_D K^-) + \Gamma(B^+ \to [\overline{f}]_D K^+)}{\Gamma(B^- \to [\overline{f}]_D K^-) + \Gamma(B^+ \to [f]_D K^+)} \qquad (1.30) \\ &= r_D^2 + r_B^2 \pm 2 r_B r_D \cos\gamma \cos(\delta_B + \delta_D) \\ A_{ADS} &= \frac{\Gamma(B^- \to [f]_D K^-) - \Gamma(B^+ \to [\overline{f}]_D K^+)}{\Gamma(B^- \to [\overline{f}]_D K^-) + \Gamma(B^+ \to [f]_D K^+)} \qquad (1.31) \\ &= 2 r_B r_D \sin\gamma \sin(\delta_B + \delta_D)/R_{ADS}, \end{aligned}$$

which are functions of γ, r_B and δ_B. A particular final state of the D^0 decay $K^-\pi^+$ is used in this analysis, which leads to two additional parameters:

$$r_D = \left| \frac{A(D^0 \to K^+\pi^-)}{A(D^0 \to K^-\pi^+)} \right| \qquad (1.32)$$

and an additional strong phase shift δ_D from the D decay. Again, the limiting factor in this method is that the product of the branching ratios of the B and D decays are very small, and it is limited from the statistics. Figure 1.7 shows the m_{ES} distribution of the signal events in the ADS analysis [16]. No significant signal was found.

1.2.3 The Dalitz method

The Dalitz method was first proposed by Giry, Grossman, Soffer and Zupan [17], and uses the $B^- \to DK^-$ decays followed by the multi-body D decay. The advantage of this method compared to the GLW or ADS method is two-fold: first, it involves the entire resonant sub-structure of the three-body D decay, and second, the result has

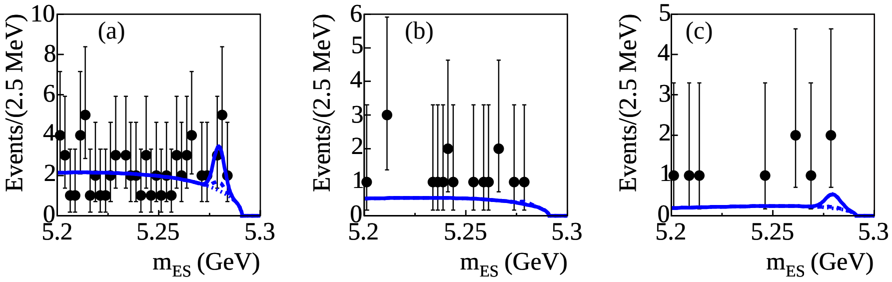

Figure 1.7: m_{ES} distributions for candidate signal events in the ADS method. (a) $\overline{D}K$ events. (b) $\overline{D}^{*}K$ events with $D^{*} \to D\pi^{0}$. (c) $\overline{D}^{*}K$ events with $D^{*} \to D\gamma$, no significant signal was found.

only a two-fold discrete ambiguity $(\gamma, \gamma+\pi)$, compared to the four-fold ambiguity in the ADS and GLW method.

The γ analysis with the Dalitz method is performed using the $D^0 \to K^0_S\pi^+\pi^-$ decay. Although in principle other D decay channels such as $D^0 \to K_sK^+K^-$ can be used, $D^0 \to K^0_S\pi^+\pi^-$ has a larger branching fraction and an extremely rich structure on the Dalitz plot that gives large interference effects.

Consider the following decay chain:

$$B^- \to D^0K^- \to (K_s\pi^+\pi^-)_{D^0}K^-. \tag{1.33}$$

At leading order, two Feynman diagrams contribute to this decay:

$$A(B^- \to D^0K^-) \;=\; A_B, \text{ and} \tag{1.34}$$

$$A(B^- \to \overline{D}^0K^-) \;=\; A_B r_B e^{i(\delta_B-\gamma)}, \tag{1.35}$$

where δ_b is the strong phase difference between two amplitudes and γ is the usual

CKM angle. Since we are interested in the D^0 decaying into multi-body final states, we define the D meson decay amplitude as:

$$f_D(s_{12}, s_{13}) = A(D^0 \rightarrow K_s(p_1)\pi^+(p_2)\pi^-(p_3)), \tag{1.36}$$

where $s_{ij} = (p_i + p_j)^2$ and p_1, p_2, p_3 are the four-momenta of the K_s, π^+, π^-, respectively. Therefore, we can write the amplitude of the whole decay as

$$A(B^- \rightarrow (K_s\pi^+\pi^-)_{D^0}K^-) = f_D(s_{12}, s_{13}) + r_B e^{i(\delta_B - \gamma)} f_D(s_{13}, s_{12}), \tag{1.37}$$

and the corresponding CP-conjugate part is given by:

$$A(B^+ \rightarrow (K_s\pi^+\pi^-)_{D^0}K^+) = f_D(s_{13}, s_{12}) + r_B e^{i(\delta_B + \gamma)} f_D(s_{12}, s_{13}). \tag{1.38}$$

Note that under CP transformation the strong phase difference δ_b remains the same since the strong interaction does not violate CP, while the weak phase γ changes sign. However, to determine γ one needs the functional dependence of both the moduli and the phases of the D^0 meson decay amplitude, $f_D(s_{12}, s_{13})$. In this thesis we will present the model-dependent approach, which uses a high-statistics tagged D sample, $D^{*-} \rightarrow D^0\pi^-$, with $D^0 \rightarrow K_S^0\pi^+\pi^-$. This D sample can be used to extract the moduli and the phase of $f_D(s_{12}, s_{13})$ using the Dalitz plot technique. This will be presented in the Ch. 4. Although in principle one can use a model-independent approach [17], this method will not be feasible with the limited statistics currently available in *BABAR*.

1.3 CKM γ and constraints on new physics

Since the $B^- \to D^0 K^-$ decay is dominated by tree-level processes, the determination of γ is expected to be unaffected by new physics (NP). However, surprisingly the measurement of γ might help us to understand physics beyond the standard model through comparisons with higher-order virtual processes. For many extensions of the standard model, new particles enter into the virtual loop diagrams(also known as "penguins"), with the possibility to change the *CP* parameters. Therefore, together with the measurement of V_{ub}/V_{cb}, which can be determined from semi-leptonic decay and also is not affected by new physics, the measurement of γ provides a constraint in the $\bar{\rho} - \bar{\eta}$ plane that must be fulfilled by any new physics model. This is a very powerful constraint to exclude new physics models. Figure 1.8 shows the regions selected by these two constraints.

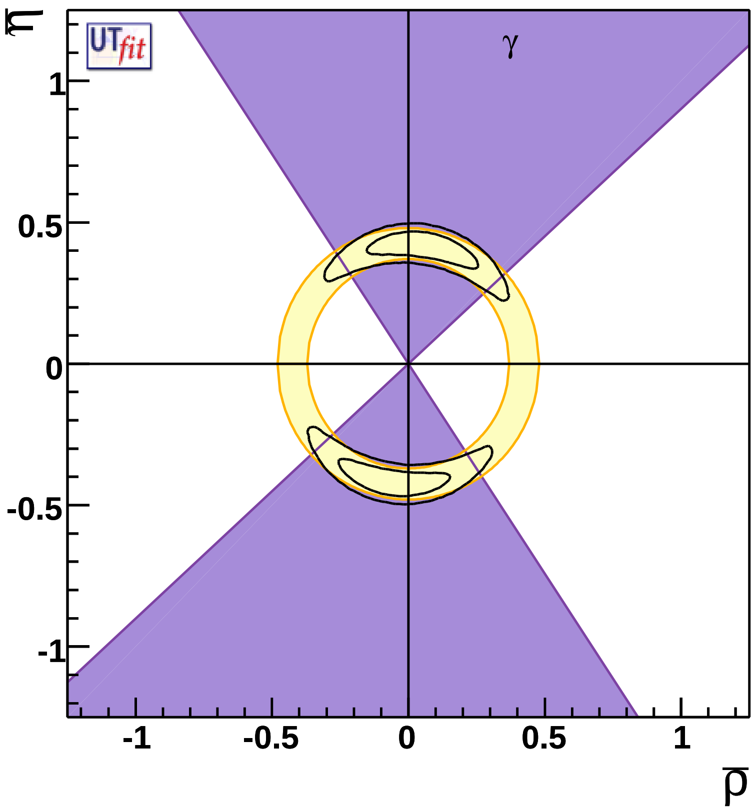

Figure 1.8: Regions of the $\bar{\rho} - \bar{\eta}$ plane selected by the constraints imposed by the determination of V_{ub}/V_{cb} and γ from tree-level processes.

Chapter 2

The PEP-II and *BABAR* Detector

2.1 Overview

The *BABAR* detector [18], located at the Stanford Linear Accelerator Center (SLAC), Menlo Park, California, is a general multi-purpose detector with large acceptance, good tracking, and excellent particle ID capability to measure different physics processes. The primary goal of this experiment is to measure *CP* violation in B meson decay. Although CLEO, was built more than 20 years ago, *BABAR* has the unique feature that the beam energies are asymmetric, so the B mesons acquire a large boost in the lab frame. This large boost enables the B-meson decay times to be inferred from their measured decay lengths.

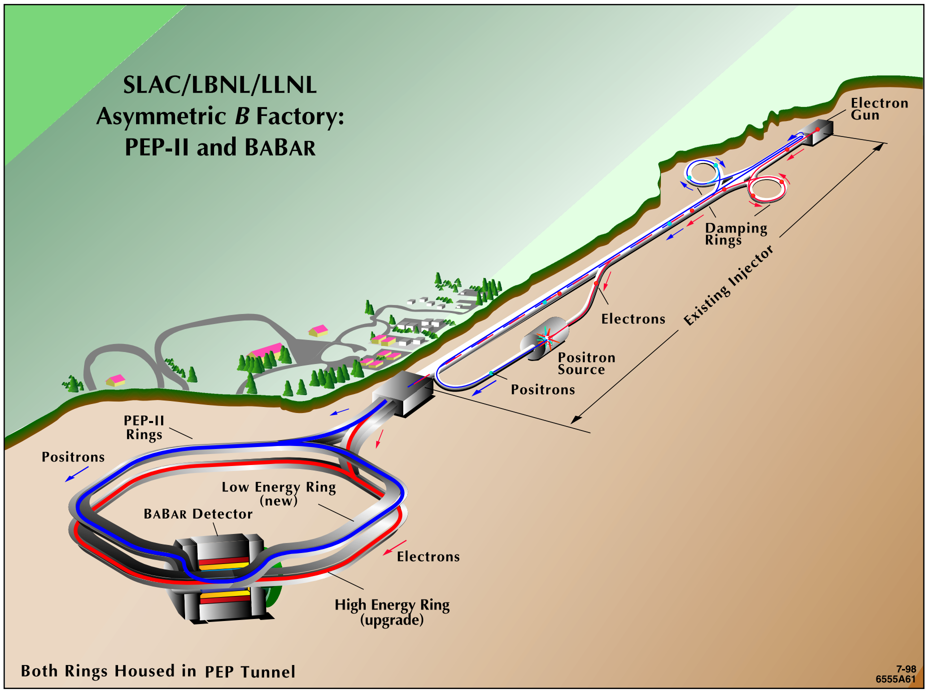

Figure 2.1: The Stanford linear accelerator with the PEP-II storage rings and the *BABAR* detector.

2.2 PEP-II and the *BABAR* Detector

The PEP-II B Factory is an asymmetric-energy electron-positron collider operating at the center of mass(c.m.) energy of 10.58 GeV, corresponding to the mass of the $\Upsilon(4S)$ resonance (which dominantly decays into $B\overline{B}$). It consists of two 2.2-km-circumference storage rings: the high energy electron ring (HER) and the low energy positron ring (LER). Fig. 2.1 shows the linac and the BaBar detector, and Table 2.1 gives the parameters of these storage rings.

The asymmetry in beam energies leads to a lorentz boost to the c.m. frame of $\beta\gamma = 0.56$, which makes it possible to reconstruct the decay vertices of the two B mesons that are produced. This unique feature allow all the time-dependent CP

Parameters	Design	Peak Luminosity
Current HER/LER (mA)	750/2140	1875/2900
Number of bunches	1722	1722
RMS size of the luminous region σ_x (μm)	110	120
RMS size of the luminous region σ_y (μm)	3.3	3.5
β_y^* (mm)	15	11-12
Luminosity (10^{33} cm^{-2}s^{-1})	3.0	12.07
Integrated luminosity (pb^{-1}/day)	130	910.7

Table 2.1: PEP-II beam parameters. The peak luminosity was on 18, August 2006.

measurements.

The $\Upsilon(4S)$ decays dominantly into B^+B^- and $B^0\bar{B}^0$ pairs, and for the process $e^+e^- \rightarrow \Upsilon(4S) \rightarrow B^0\bar{B}^0$ is approximately 1.1 nb. Figure. 2.2 shows the cross section for e^+e^- annihilation into hadrons as a function of c.m. energy, as measured by the CLEO Collaboration.

Some fraction (around 12%) of the data, referred to off-resonance data, are taken at a c.m. energy 40 MeV below the $\Upsilon(4S)$ resonance. This data, which is taken below the $B\bar{B}$ production threshold, is used for studies of non-resonant $e^+e^- \rightarrow q\bar{q}$ background.

Figure 2.3 shows the total integrated luminosity recorded since the start of the experiment. The peak luminosity achieved by PEP-II is $1.2 \times 10^{34} cm^{-2}s^{-1}$.

2.3 Overview of *BABAR* detector

The *BABAR* detector consists of five major sub-detectors. The Silicon Vertex Tracker (SVT) and the Drift Chamber (DCH) make up the *BABAR* tracking system. The SVT is the first component of the tracking system, providing precise measurements

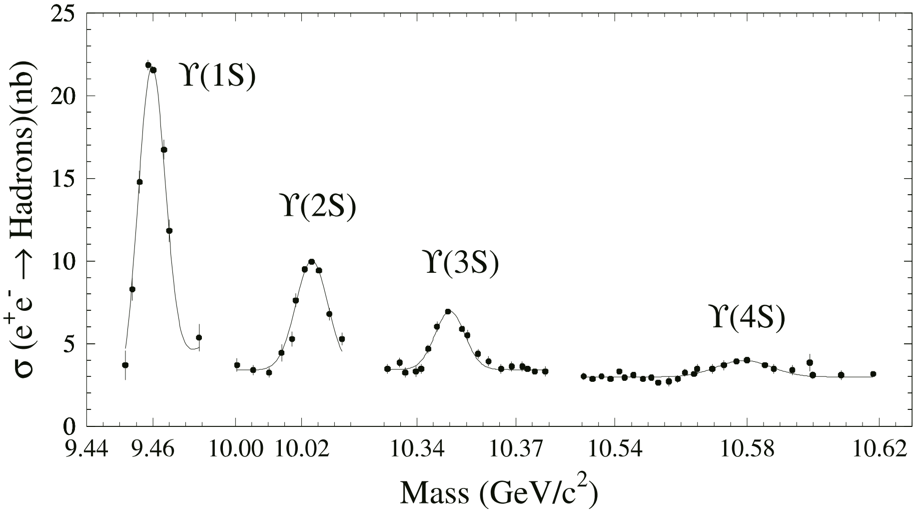

Figure 2.2: The rate of particle production as a function of energy in the region of various Upsilon states as measured by the CLEO collaboration.

of decay vertex positions and detection of low momentum charged particles.

The DCH serves as the outer component of the tracking system. The main purpose of DCH is the momentum measurement for charged particles. In addition, it provides the ionization energy loss per unit length (dE/dx) measurements for use in particle identification (PID).

The Detector of Internally Reflected Cherenkov light (DIRC) is a novel device providing separation of pions, kaons and protons from 500 MeV to 4.5 GeV.

The CsI(Tl) Electromagnetic Calorimeter (EMC) provides measurements of energy deposited by charged and neutral particles from 20 MeV to 4 GeV, which allows detection of photons and electrons. π^0 can be reconstructed from photon tracks as $\pi^0 \to \gamma\gamma$ dominantly.

The outermost detector is the Instrumented Flux Return (IFR). This system is

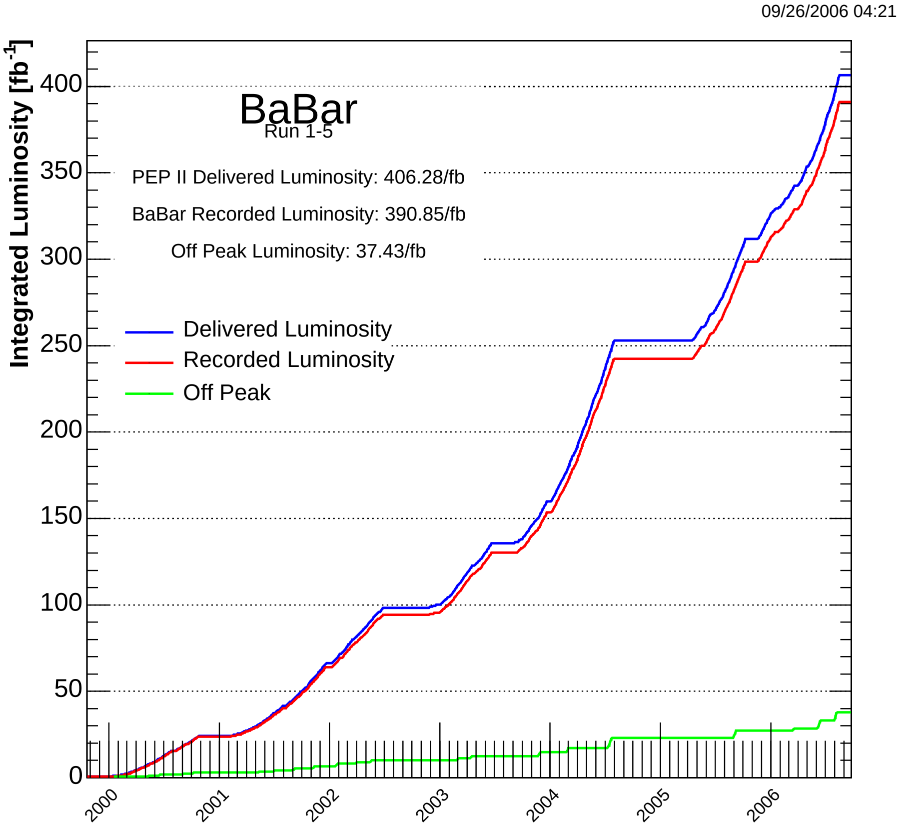

Figure 2.3: Total integrated luminosity delivered by PEP-II and recorded by the *BABAR* detector.

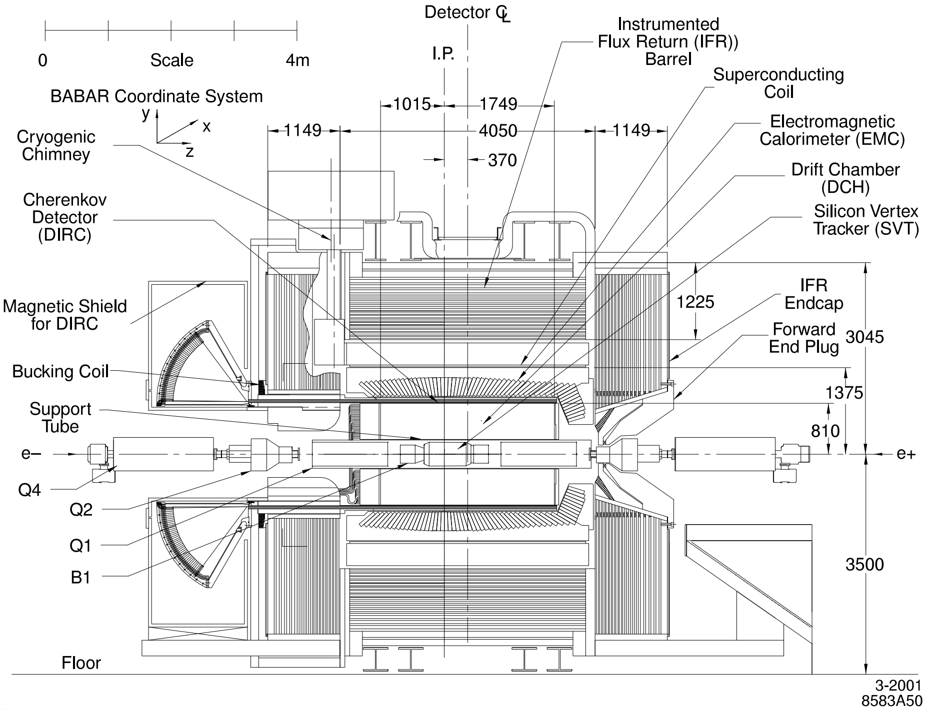

Figure 2.4: *BABAR* detector longitudinal section.

primarily used for identification of muons and neutral hadrons such as K_L. Besides IFR, the whole detector is surrounded by an uniform magnetic field of 1.5 T field strength which is used for the momentum measurements of the charged particles. Figure 2.4 shows a longitudinal section through the *BABAR* detector, while Fig 2.5 shows an end view. Each detector component is described in detail in the following subsections.

2.4 Silicon Vertex Tracker(SVT)

The Silicon Vertex Tracker(SVT) is the innermost component of the *BABAR* detector, which allows precise reconstruction of charged particle trajectories and the decay

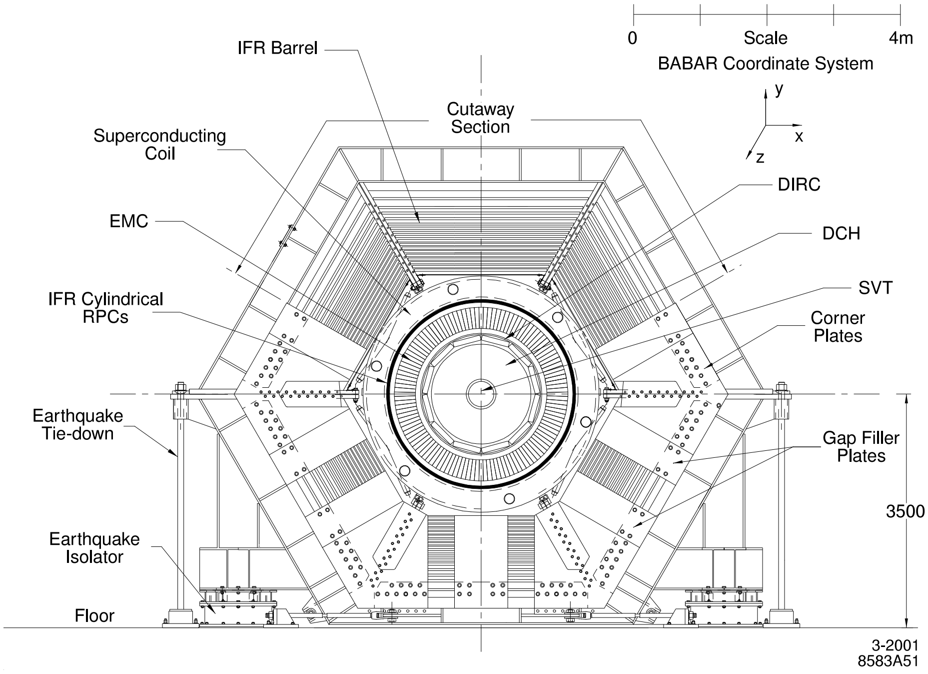

Figure 2.5: *BABAR* detector end view.

vertices near the interaction region. The SVT was designed to meet the following physical requirements:

- It must provide spatial z-resolution at least $80 \mu m$ to allow time-dependent *CP* asymmetry measurements; [1]
- Provide standalone tracking for particles with low transverse momentum; [2]
- Long mean-time-to-failure, as SVT is inaccessible during normal operation;
- It must be able to stand over 2 Mrad of ionizing radiation.

These physical requirements led to the choice of the SVT having five layers of double-sided silicon strip sensors made up of 52 modules. Figure 2.7 shows the lon-

---

[1] This number is obtained from Monte Carlo studies.

[2] The drift chamber alone cannot reliably measure p_T below 120 MeV due to 1.5T magnetic field.

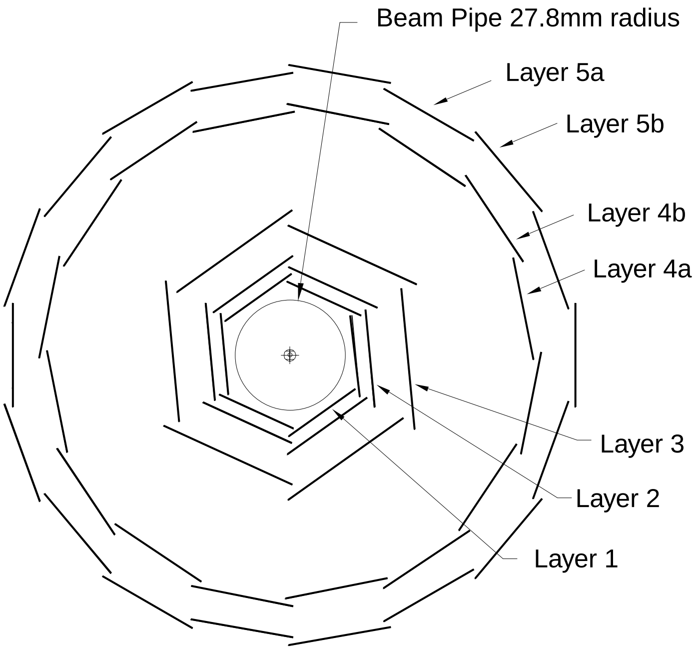

Figure 2.6: Tranverse section of the SVT.

gitudinal section of the SVT.

SVT layout

The design consists of five layers of double silicon strip sensors, divided azimuthally into modules, as shown in Fig. 2.6. The first three innermost layers run parallel to the beam pipe, which provide impact parameter measurements of charged tracks with high resolution.

The outer layers are placed closer to the Drift Chamber(DCH) to improve the alignment between SVT and DCH. Also, the two outer layers are arranged into arches(see Fig. 2.7) to minimize the amount of silicon required to cover the solid angle.

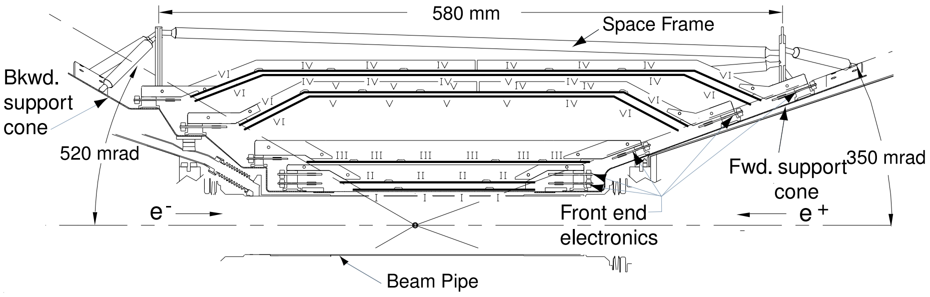

Figure 2.7: Side-view of the SVT.

SVT sensor

Each module is made up of four to eight 300μm-thick high-resistivity (6-15kΩ cm) n-type silicon wafers, with n^+ and p^+ strips running orthogonally on opposite sides. The ϕ strips run parallel to the beam direction and the z strips are oriented transversely to the beam axis. The total active silicon area is 0.96m^2, covering 90% of the solid angle in the *c.m.* frame.

Monitoring and calibration

Since stable operation of the SVT is essential, various parameters are carefully monitored continuously. Temperature and humidity are maintained by external cooling of the beam pipe with chilled water and a flow of dry air though the support tube. The relative position of the SVT has been determined from an optical survey during assembly. Global SVT alignment is performed every 2-3 hours and new calibration constants are determined by minimizing the difference between track parameters obtained with SVT-only and DCH-only fits.

Besides the global alignment of the SVT, local alignment is sometimes necessary

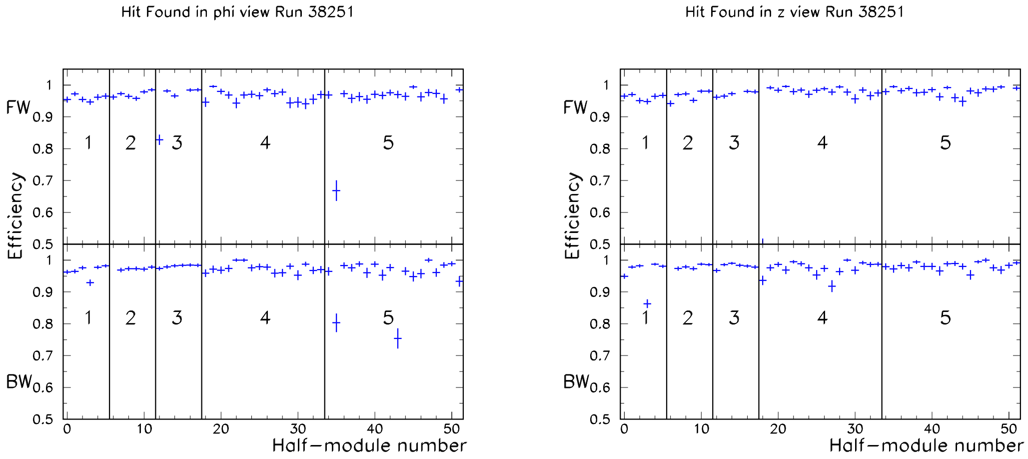

Figure 2.8: SVT reconstruction efficiency as measured in $\mu\mu$ events, the reconstruction efficiency is more than 97% per module.

when the magnet quenches, or during a detector access. The alignment is performed by fitting tracks from $e^+e^- \to \mu^+\mu^-$ events and cosmic rays.

SVT performance

The *BABAR* SVT has been performing extremely well during the life of operation. Figure 2.8 shows SVT hit reconstruction efficiency as measured on $\mu\mu$ events. The average efficiency reaches above 97%. Table 2.2 shows hit resolution in the z and ϕ directions.

2.5 Drift Chamber(DCH)

The DCH is the second part of the *BABAR* tracking system. The main function of DCH is to efficiently detect charged particles and measure their momentum. This detector is particularly important to the Dalitz plot analysis since each point on the

Parameters	Design	Achieved (typical)
ϕ resolution in μm	80	40
z resolution in μm	80	50

Table 2.2: Comparison of the design and achieved performance for the *BABAR* SVT detector.

Dalitz plot represent the momentum of the resonances. It complements the SVT, as daughters of long-lived particles, like K_S^0, whose decay vertices fall outside the SVT volume can only be reconstructed by the DCH. The DCH was designed to meet the following physical requirements:

- It must provide maximal solid angle coverage and good measurement of the transverse momentum;
- Provide efficient track reconstruction over a wide range of momentum;
- Provide particle identification by measurement of ionization loss $\frac{dE}{dx}$.

DCH design

In order to meet the physical requirements, the DCH has cylindrical structure. It is 2.8m long cylinder placed asymmetrically about the IP in order to increase coverage in the forward direction. The DCH is mostly constructed from aluminum, where the outer wall is made of 9mm-thick carbon-fiber-composite and the inner wall is made of 1mm-thick beryllium. These materials are light in weight and have small radiation length. Figure 2.9 shows the longitudinal section of the DCH.

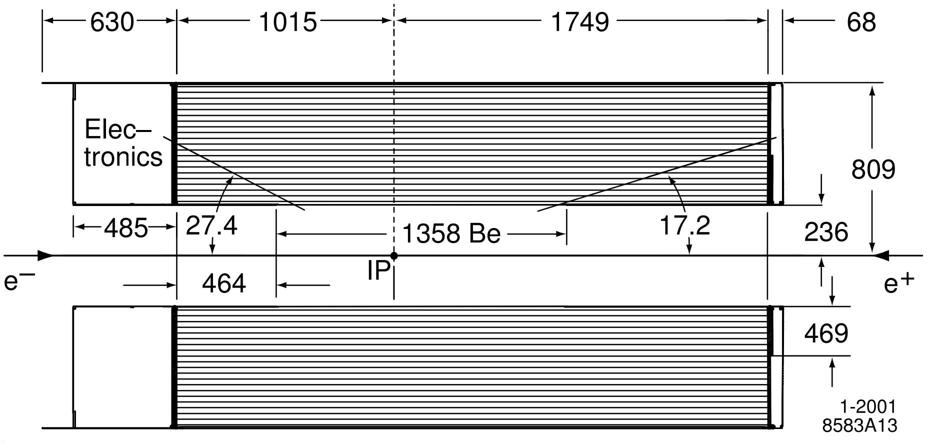

Figure 2.9: Longitudinal section of the DCH.

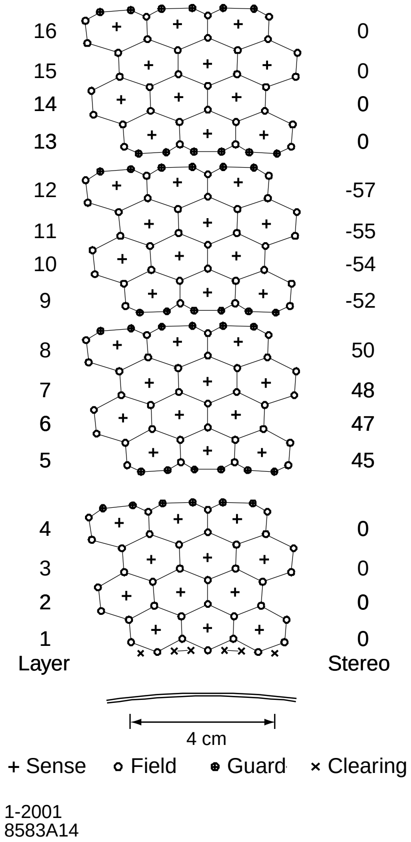

Figure 2.10: Layout of all superlayers in DCH.

DCH drift cells

The DCH is a wire chamber consisting of 7104 hexagonal cells each 11.9mm to 19.0mm-wide. Each of these cells is made of six gold-plated aluminum field wires with a gold-plated tungsten-rhenium sense wire at the center. The field wires are grounded, while the sense wires are operated at 1960V. In total, there are 40 layers of wires filling the DCH volume and organized into 10 superlayers. Each layer in a superlayer has the same wire orientation and an equal number of cells. The stereo angles of the superlayers are alternated between axial(A) and stereo pairs(U,V) in the order of AUVAUVAUVA to obtain longitudinal position information. Figure 2.10 shows the layout of all superlayers of the DCH.

DCH gas mixture

Gas mixture is critical to the operation of the DCH. The chamber is filled with a 80:20 mixture of helium:isobutane at a constant pressure of 4mbar. The choice of the gas mixture keeps multiple scattering inside the DCH at a minimum. During normal operation, one full volume of fresh gas is added every 36 hours, and the water concentration is kept at 3500 ppm in order to prevent electrical discharges. [3]

DCH performance

The DCH has been performing extremely well over the entire period of *BABAR* experiment. The DCH track reconstruction efficiency in the acceptance region is around

---

[3] This effect is known as the Malter effect.

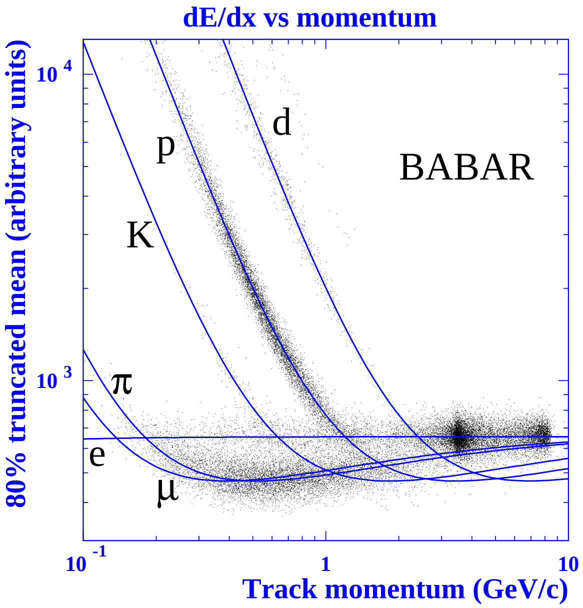

Figure 2.11: dE/dx in the DCH as a function of track momenta for different charged particles types.

93-94%. Figure 2.11 shows the dE/dx in the DCH as a function of track momenta for different charged particles.

2.6 Detector of Internally Reflected Cherenkov Light(DIRC)

The DIRC is a new kind of ring-imaging Cherenkov detector, designed to provide at least 3σ separation between high-momentum pions and kaons. Almost every analysis involving momentum above 500 MeV/c kaons will require DIRC information. The DIRC was designed to meet the following physical requirements,

- thin and uniform to minimize degradation of the calorimeter energy resolution;

- small in radial dimension to reduce the volume of the calorimeter;[4]
- fast signal response and able to tolerate high background.

The DIRC concept

The basic principle of the DIRC is quite simple: when a particle passes though the fused silica bar, it radiates Cherenkov light, and the Cherenkov angle θ_C relates to the particle velocity as:

$$\cos\theta_C = \frac{1}{n\beta} = \frac{c}{nv}, \tag{2.1}$$

where n is the index of refraction of the fused silica $n = 1.473$. Therefore, different particles will have different θ_C value and this information can be used for particle identification.

Fused silica is used because it not only serves as Cherenkov radiator, but also as a wave guide. Silica is chosen because of its high index of refraction, long attenuation length and low chromatic dispersion. Figure 2.12 shows a diagram of the DIRC radiation bar and the imaging region.

The DIRC design

The DIRC consists of 144 silica bars, which are 17mm thick, 35mm wide and 4.9m long. When a charged particle traverses the bar, the Cherenkov light propagates via total internal reflection to the standoff box, where the light is detected by an array

---

[4] The calorimeter is the most expensive component in *BABAR*.

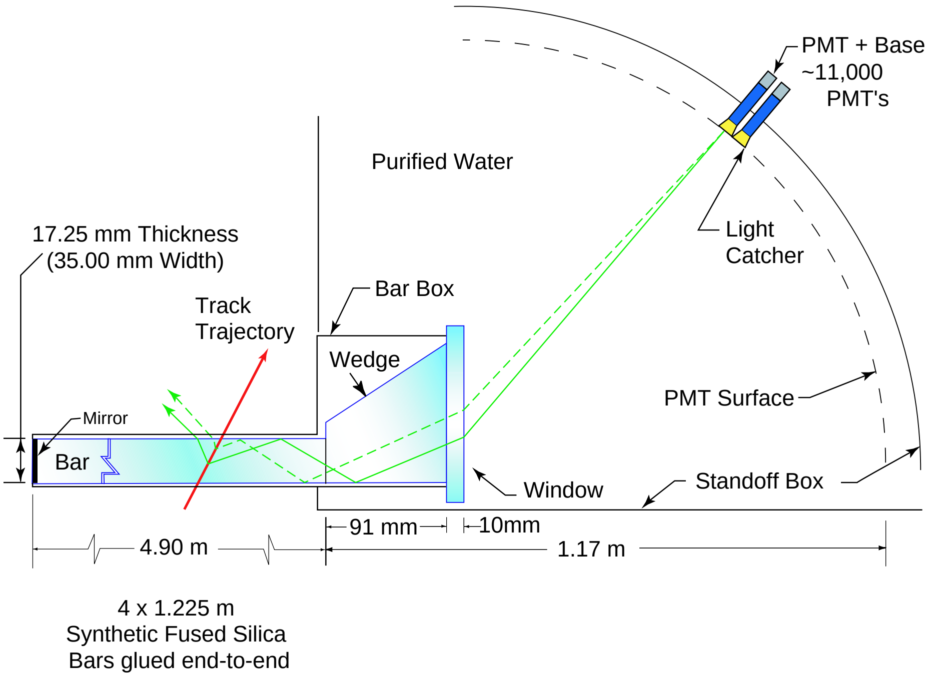

Figure 2.12: The DIRC layout.

of photomultiplier tubes(PMT). In order to reduce the number of PMTs, one end of the bar has a mirror that reflects the light toward the other end, which has a window to the standoff box.

The standoff box, which is instrumented by 12 sectors of 896 PMTs each, is located outside the flux return of the magnetic system. The magnetic field in the standoff box is typically about 1 Gauss, which is achieved by means of bucking coil that conteracts the solenoidal field. The two opposing coils are always ramped together to keep the field low in the region of the phototubes. As the nominal field inside the detector is about 15000 Gauss, the low magnetic field in standoff box allows to use conventional PMTs to collect the Cherenkov light. Also, because those particles are produced mainly forward in the detector due to the boost, the standoff box is placed at the backward end.

Water is used to fill the standoff box and as an inexpensive medium to transport the Cherenkov photons. Water is chosen because the refractive index ($n = 1.346$) matches reasonably well with fused silica to minimize refraction at the bar-water interface. The water is purified with filters and a reverse osmosis unit, de-gassed, de-ionized and exposed to UV radiation to prevent bacteria growth.

The DIRC performance

Due to good angular resolution of the DIRC it is possible to achieve $\sim 4\sigma$ or better π/K separation for most particles of momenta higher than the DIRC threshold. Figure 2.13 shows a typical performance of the DIRC. This good performance at high momentum plays a critical role in identification of two-body charmless decays such as $B \to \pi\pi$ and $B \to K\pi$.

2.7 Electromagnetic Calorimeter(EMC)

Located outside the DIRC, EMC is the component of the detector dedicated to the detection of photons and electrons. It also provides measurements of the energy deposition of both charged and neutral particles. Neutral particles are particularly important for the reconstruction of D^*, which primarily decays into $D^0\gamma$ and $D^0\pi^0$. Not only that, efficient detection of electrons is vital to determine the flavor of the B meson in all the semi-leptonic analysis(lepton tagging), and also important for

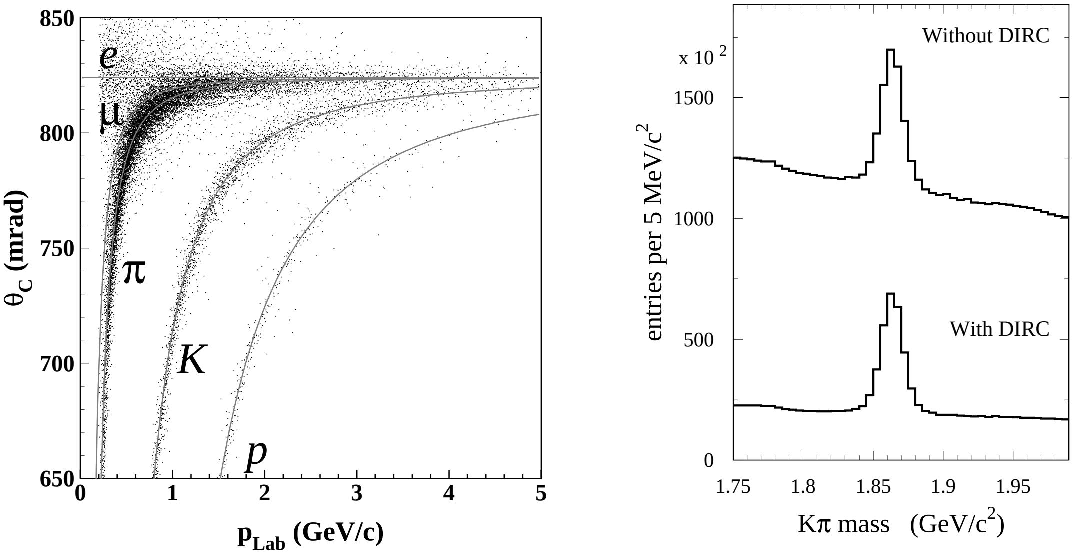

Figure 2.13: **Left.** The DIRC particle identification performance. The θ_C is the measured Cherenkov angle and p_{LAB} is the charged track momentum. **Right.** The $K\pi$ invariant mass distribution with and without DIRC information for the kaon ID. The mass peak corresponding to a D^0 particle.

the search the FCNC(Flavor Changing Neutral Current) analysis like $B \rightarrow Xe^+e^-$ analysis. The EMC was designed to satisfy the following physical requirements.

- excellent energy resolution over a wide energy range from 20 MeV to 9 GeV;
- capable to detect π^0, γ as well as electrons efficiently;
- compatible with 1.5T magnetic field and operate reliably over 10 years.

The EMC layout

The requirements stated above lead to the choice of a hermetic, total-absorption calorimeter, composed of finely-segmented array of 6580 thallium-doped cesium iodide CSI(Tl) crystals. It consists of two parts: the barrel detector made of 5760 crystals

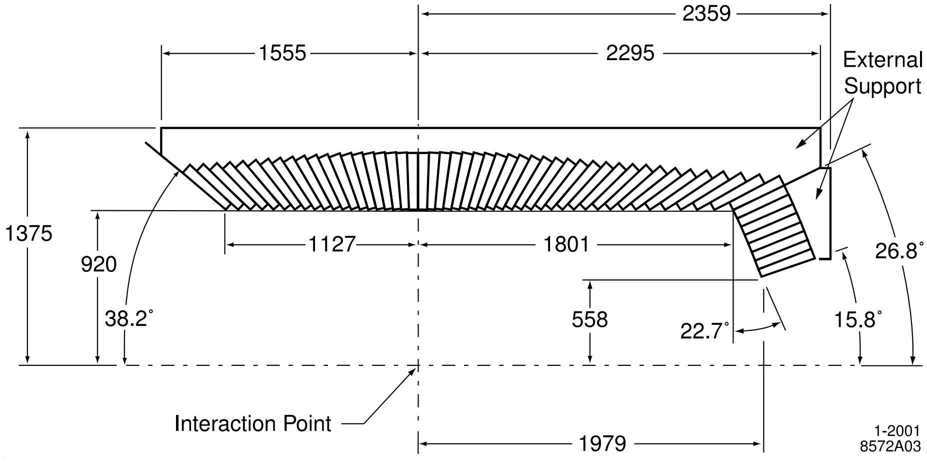

Figure 2.14: Longitudinal cross section of the EMC.

arranged in 48 distinct rings with 120 crystals each. The forward endcap consists of eight rings: three rings of 120, three rings of 100, and two rings of 80 crystals. This roughly covers 90% of the solid angle. Figure 2.14 shows the longitudinal cross section of the EMC layout.

The EMC crystal

The Thallium-doped CsI crystal meets the needs of the *BABAR* experiment. Based on the successful experience at CLEO, CsI was adopted due to high light yield and small Moliere radius, allowing for excellent energy and angular resolution. These crystals were grown from a melt of CsI salt doped with 0.1% thallium. The length of the crystals varies from 29.6 cm in the backward to 32.4 cm in the forward direction to minimize the effect of shower leakage for higher momentum particles. This length corresponds to 16-17 radiation lengths and allows for small shower leakage and good energy resolution.

The EMC performance

The *BABAR* EMC has good energy resolution and angular resolution. The energy resolution of the calorimeter is determined from various processes. Usually a radioactive source and Bhabha scattering are used. The single photon energy resolution was determined to be

$$\frac{\sigma_E}{E} = \frac{\sigma_1}{\sqrt[4]{E(\text{ GeV})}} \oplus \sigma_2 \tag{2.2}$$

where σ_1 is $2.32 \pm 0.30\%$ and σ_2 is $1.85 \pm 0.12\%$. The first term, which is energy dependent, corresponds to the fluctuations in photon statistics, electronics noise and low energy beam-generated backgrounds. The constant, second term arises from non-uniformity in the light collection, leakage or absorption in the material between and in front of the crystals.

Similarly, the angular resolution could be determined from the analysis of π^0 and η decays to two photons of approximately equal energy. The angular resolution was determined to be

$$\sigma_\theta = \sigma_\phi = \frac{\sigma_1}{\sqrt{E(\text{ GeV})}} \oplus \sigma_2 \tag{2.3}$$

where σ_1 is 3.87 ± 0.07 mrad and σ_2 is 0.00 ± 0.04 mrad. Figure 2.15 shows the angular resolution of the EMC for photons from π^0 decays. The agreement between data and Monte Carlo expectation is very good.

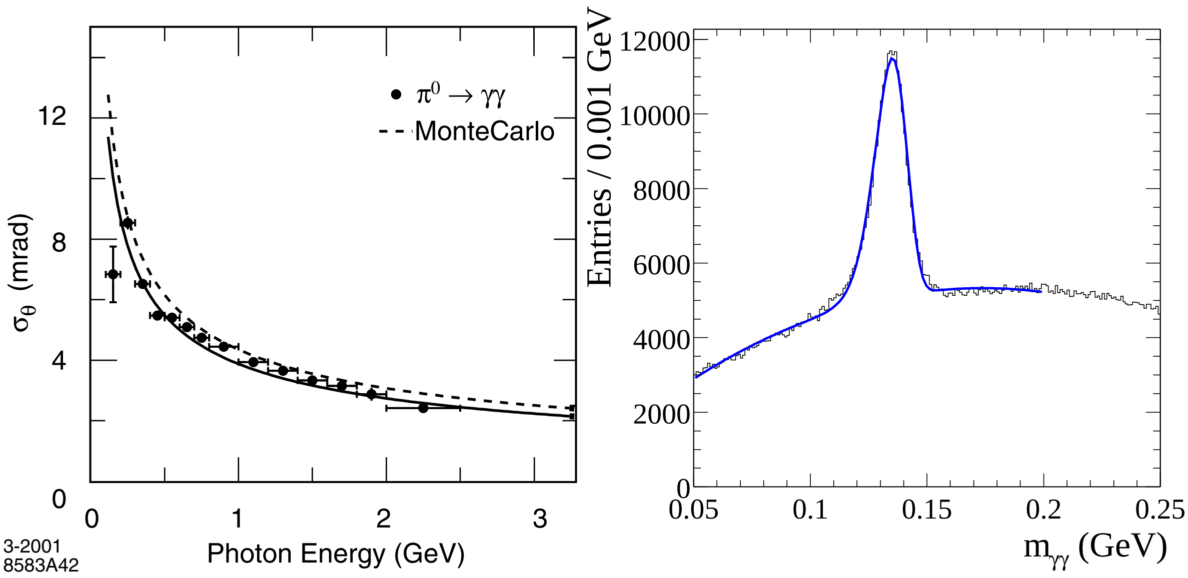

Figure 2.15: **Left.**The angular resolution of the EMC for photons from π^0 decay **Right.** Invariant mass of two photons in $B\bar{B}$ events. The solid line is a fit to the data.

2.8 Instrumented Flux Return(IFR)

The Instrumented Flux Return(IFR) largely serves as the muon and K_L identification system. Detection of muons is particularly important for analyses involving τ and FCNC $B \to Xl^+l^-$ decay, and in the reconstruction of $J/\psi \to \mu^+\mu^-$. The IFR was designed to satsify the following physical requirements:

- identify muons with high efficiency and good purity;
- detect neutral hadrons over a wide range of monenta and angles;
- large solid angle coverage, good efficiency and angular resolution;
- detector component must be relatively cheap, due to very large system.

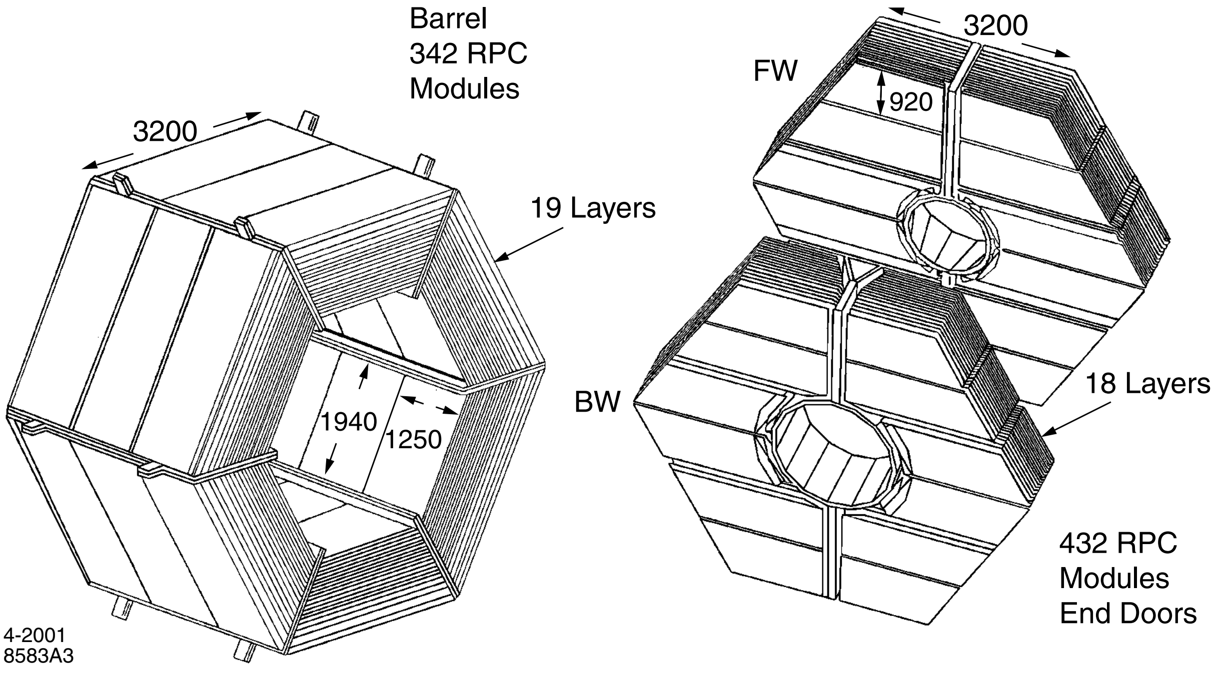

Figure 2.16: Overview of the IFR, barrel and endcap subsystems.

The IFR design

The following physical requirements lead to resistive plate chambers (RPCs) installed in the gaps between 18 plates of the steel flux return, which is used as a hadron absorber. The IFR detector covers a total active area of about $2000m^2$. Between the steel plates, RPCs are installed and used for muon identification. Figure 2.16 shows the barrel and endcap sections of the IFR.

The RPC system

As illustrated in Fig. 2.17, each RPC consists of two bakelite sheets kept 2mm apart by polycarbonate spacers (0.8cm^2) positioned about every 10 cm. High voltage (8000V) is applied to one of the surfaces of the bakelite sheets. Graphite is applied to the external surfaces of these sheets to make it slightly conducting, while the other side is grounded. The bakelite surfaces facing the gap are treated with lineseed oil. Next, 2-4cm read-out strips are placed outside the graphite coating to read out the streamer signals from ionizing particles. The orientation of the strips on the two sides of a chamber is orthogonal, which allows three-dimensional reconstruction in the IFR and the association of tracks reconstructed in the DCH or the neutral clusters from the EMC.

The RPC is a gaseous chamber. Due to safety reasons, a non-flammable gas mixture of 56.7% argon, 38.8% freon 134a, and 4.5% isobutane is chosen. The RPC is operated in streamer mode, which uses higher voltage than a typical proportional chamber, and leads to formation of a streamer with the collected charge no longer proportional to the original ionization.

The IFR performance

Figure 2.18 shows the IFR performance for muon/pion separation. The muon detection efficiency in the first year of running was close to 90% with the pion misidentification rate of about 5-6% for the momentum range of 2.0-4.0 GeV. Lower pion misidentification can be achieved for tighter criteria, but at the expense of detection efficiency.

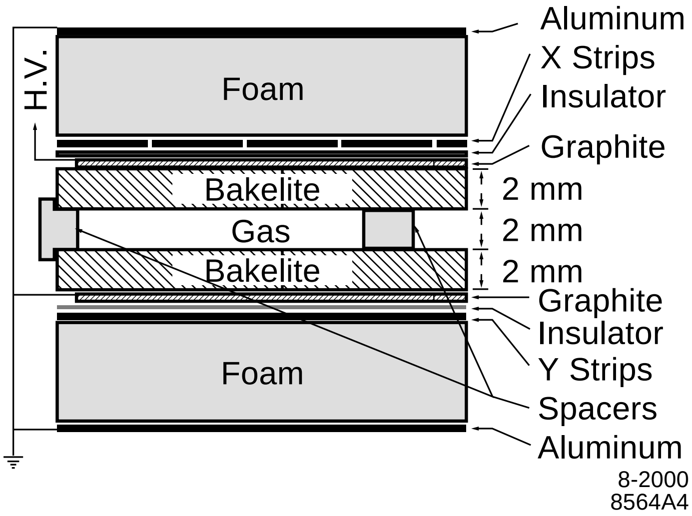

Figure 2.17: Cross section of a planar RPC with the schematics of the high voltage connection.

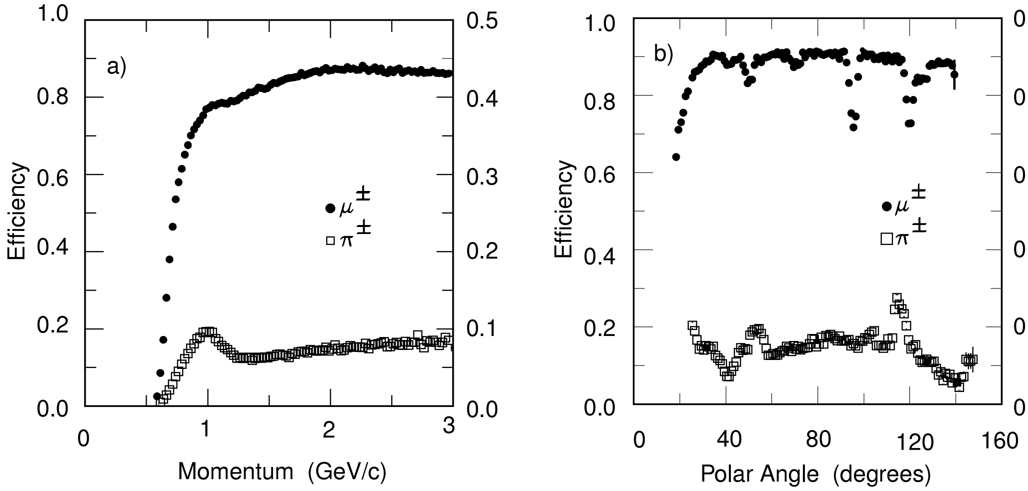

Figure 2.18: Muon efficiency (left scale) and pion misidentification probability (right scale) as a function of a) the laboratory track momentum and b) the polar angle (for $1.5 < p < 3.0$ GeV momentum), obtained with loose selection criteria.

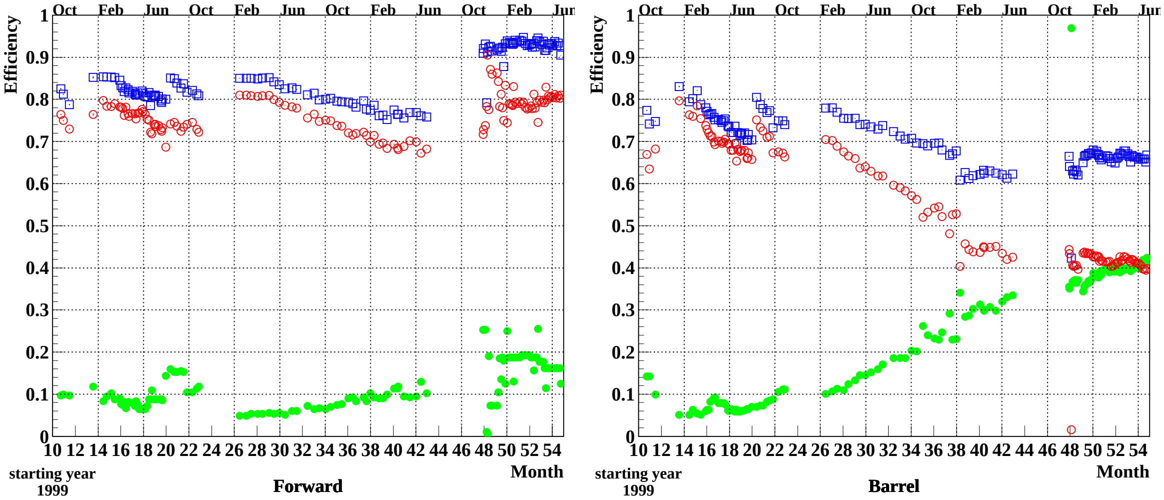

Figure 2.19: The RPC efficiency degradation with time for the forward endcap (left) and for the barrel (right) using $e^+e^- \rightarrow \mu^+\mu^-$ events. Red is the average efficiency over all modules in a group, blue is the average efficiency for modules that have efficiency greater than 10% and green is the fraction of modules with efficiency less than 10%.

Degraded RPC

At the early stage of the experiment it was found that a large number of RPCs were degraded in the their response and continued to degrade with time, which caused significant reduction of the IFR performance. Figure 2.19 shows the time evolution of the RPC efficiency, showing a significant drop in performance. Extensive research on the bad RPC led by Princeton physicist Changguo Lu[5] revealed that in many cases uncured linseed oil droplets had formed on the inner surface of the bakelike plates, leading to current paths from oil stalagmites bridging the 2mm gap. Several remedies were tried, including flowing $N_2/O_2(40/60)$ and allowing oxygen to polymerize the uncured linseed oil. However, none of these efforts proved successful.

---

[5] The author was also involved in the study the degraded RPC.

Figure 2.20: Surface image of a bad RPC

Upgraded RPC for the endcap

The forward end-cap RPCs were replaced with an upgraded version in summer 2002. The newer RPC has better quality control, and the thickness of the linseed oil is greatly reduced to prevent the formation of oil stalagmites.

The new LST for barrel upgrade

Due to the bad experience with the linseed-oil-based RPC, the *BABAR* barrel IFR is in the process of being upgraded with Limited Streamer Tubes(LST). The LST consists of a silver-plated wire $100\mu m$ in diameter, located at the center of a cell of $9 \times 9mm^2$ section. A plastic (PVC) extruded structure, contains 8 such cells, open on one side. The profile is coated with a resistive layer of graphite, having a typical surface resistivity between 0.2 and $1M\Omega/\mathrm{cm}^2$. High voltage (4.7 kV) is applied to the tube typically and the gas mixture is based on a non-flammable combination of CO_2, Argon, and isobutine. The collaboration is in the process of upgrading the


07 10 2002

Figure 2.21: Photo of a standard LST.

barrel IFR, by replacing bad RPCs with LSTs. Two out of six sextants was replaced in 2004 are operating with high efficiency. The remaining four sextants were recently installed in the fall of 2006. Figure. 2.21 shows the layout of the standard LST.

Chapter 3

Hadron Spectroscopy

3.1 Outline

This chapter is devoted to the physics of the Dalitz plot and hadron spectroscopy. In the first part of this chapter the basic features of the Dalitz plot is described, and the following topics will be covered to describe the dynamical properties of resonances:

- Dynamical function (Breit Wigner form factor)
- Spin dynamics (angular distributions)
- Finite-size effect of hadrons (Blatt-Weisskopf form factor)

The second part of this chapter is devoted to hadron spectroscopy. Although hadron spectroscopy is a broad subject and involves rich structure of QCD physics, this topic is not usually included in modern particle physics textbooks, thus it is worth to summarize the details here. The K-matrix theory, based on unitarity of the S-matrix, is introduced and various dynamical functions are derived. The complex S-matrix pole position of the hadron and the relationships to the usual Breit Wigner parameters are also discussed. [1]

3.2 Introduction to Dalitz plot

A Dalitz plot is a representation of a three-body decay, $D \rightarrow abc$, in a two-dimensional plane. The two axes of the plot are the squared invariant masses of two of the three possible particle pairs. For example.

$$\begin{aligned} s_{12} &\equiv (p_1 + p_2)^2, \\ s_{23} &\equiv (p_2 + p_3)^2. \end{aligned} \tag{3.1}$$

where $p^2 \equiv E^2 - \vec{p}^2$ and we denoted 1,2,3 as a,b,c respectively. Dalitz plots owe their name to Richard Dalitz, who developed this technique in order to analyze the decay $K^+ \rightarrow \pi^+\pi^+\pi^-$ [19]. [2] A Dalitz plot is an extremely powerful tool to explore the dynamics of the resonances. For three-body final states when the parent particle is a scalar, the decay rate is

$$\Gamma = \frac{1}{(2\pi)^3 32\sqrt{s^3}} \left|\mathcal{M}\right|^2 dm_{12}^2 dm_{23}^2, \tag{3.2}$$

---

[1] I thank Prof. A. Weinstein and Prof. M.R. Pennington who taught me about S-matrix theory.

[2] At that time, the kaon was “τ-meson”

where m_{12}^2 and m_{23}^2 are the squared invariant masses of respective particle pairs. If $|\mathcal{M}|^2$ is constant, the allowed region of the plot will be uniformly distributed with events. Any variation in $|\mathcal{M}|^2$ over the Dalitz plot is due to dynamical effect rather than the kinematics. Figure 3.1 shows the kinematically-allowed region of a typical Dalitz plot.

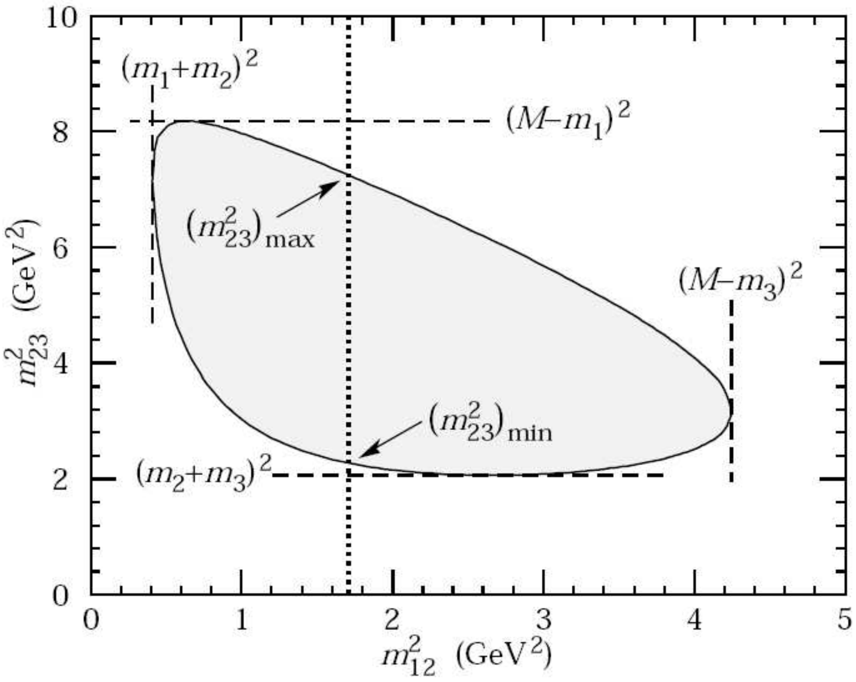

Figure 3.1: Dalitz plot for a three-body final state. Four-momentum conservation restricts events to the shaded region, whose area is determined by the masses of the decaying particle and parent particle. [20]

The matrix element $|\mathcal{M}|$

We need to specify the matrix element $|\mathcal{M}|$ in order to calculate the decay rate in Eq. 3.2. Typically, the matrix element is written as a sum of the resonances parameterized by the Breit Wigner (BW) resonance formula and a non-resonant term, [3]

$$\mathcal{M} = a_0 e^{i\phi_0} + \Sigma a_r e^{i\phi_r} \mathcal{A}_{\text{spin}}(ABC/r). \tag{3.3}$$

The form factor $\mathcal{A}_{\text{spin}}(ABC/r)$ is computed as the product of the BW, describing the underlying QCD dynamics, and an angular function describing the spin dynamics of the decay. The first term $a_0 e^{i\phi_0}$ is the non-resonant term, which has unit matrix element (i.e.,with no dynamical origin). In the following section we derive the BW lineshape and the spin dynamics using the spin sum rule.

3.3 BW lineshape

The BW lineshape is an approximate model for a resonance propagator in quantum field theory. It is only exact and well-defined for fundamental particles such as Z^0 and $W^{\pm}$. Hadronic resonances, which interact strongly with all other hadrons, are very complex. Anyhow, the derivation of the BW formula is outlined below.

---

[3] It is often named as Isobar model.

3.3.1 Non-relativistic BW – time dependence

The BW form factor arises in non-relativistic quantum mechanics. The time-dependent wave function $\Phi(t)$ for an unstable particle with mean lifetime $\Gamma = 1/\tau$ is

$$\Phi(t) = \Phi(0)e^{iw_R t - \frac{\Gamma t}{2}} \tag{3.4}$$

The energy dependence of the state is given by the Fourier transform of $\Phi(t)$

$$\begin{aligned} \Phi(w) &= \frac{1}{\sqrt{2\pi}}\int \Phi(t)e^{-iwt}dt && (3.5)\\ &= \frac{\Phi(0)}{\sqrt{2\pi}}\int e^{i(-w+w_R-\frac{\Gamma}{2})t}dt && (3.6)\\ &\propto \frac{1}{E_R - E - i\frac{\Gamma}{2}}, && (3.7) \end{aligned}$$

This is the non-relativistic version of the BW formula.[4] Note that some author define the BW form factor as $\frac{1}{E-E_R+i\Gamma/2}$ [21], with an overall minus sign. In the Dalitz plot context, this means the phase acquires an extra 180 degree shift. Therefore, care must be taken when comparing the phase for different Dalitz plot results due to the different sign conventions.

---

[4] The BW formula can be derived using partial wave expansion. The details are shown in appendix A.1.

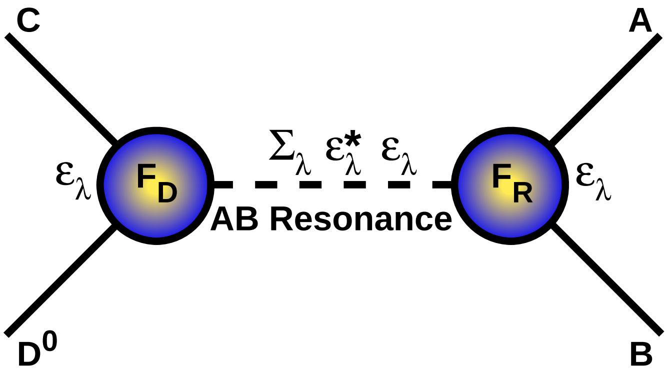

Figure 3.2: A representation of the three body decay of $D^0 \to ABC$ through an AB resonance [22]. The spin sum is performed to obtain the angular dependence of the decay.

3.3.2 Matrix element $|\mathcal{M}|$ from field theory approach

The BW formula derived above only valid in the non-relativistic regime. A more formal treatment is needed from the quantum field theory approach. For example, consider $D \to (AB)C$ where AB is a resonance as shown in the Feynman diagram in Fig. 3.2. The matrix element $\mathcal{M}$ is [22],

$$\mathcal{M} = F_D(P_{D^0} + P_C)_\mu \frac{\sum_\lambda \varepsilon^{\mu *}_\lambda \varepsilon^\nu_\lambda}{s - m^2(s) - i\sqrt{s}\Gamma(s)} (P_A - P_B)_\nu F_r \tag{3.8}$$

if it proceeds via vector (spin-1) particle. If instead the AB system is a tensor (spin-2) particle the amplitude is

$$\mathcal{M} = F_D(P_D + P_C)_\mu (P_D + P_C)_\nu \frac{\sum_\lambda \varepsilon^{\mu\nu *}_\lambda \varepsilon^{\alpha\beta}_\lambda}{s - m^2(s) - i\sqrt{s}\Gamma(s)} (P_A - P_B)_\alpha (P_A - P_B)_\beta F_r. \tag{3.9}$$

The relativistic BW form factor is the propagator

$$\frac{1}{s - m^2(s) - i\sqrt{s}\Gamma(s)}, \tag{3.10}$$

while the numerator contains a spin factor ε_λ which depends on the type of the decay: scalar, vector, tensor, etc and F_D and F_R are the correction to the vertex factor.

The relativistic BW propagators are described in Sec. 3.4, the spin factor is described in Sec. 3.5 and the correction of the vertex factor is described in Sec. 3.6.

3.4 Relativistic BW propagators

In relativistic quantum field theory, the relativistic BW form factor is the two-point function propagator, or self-energy of an unstable particle.

The Feynman rules specify the propagator for an intermediate massive, unstable, resonance:

$$\mathrm{BW} = \frac{1}{s - m^2(s) - i\sqrt{s}\Gamma(s)}, \tag{3.11}$$

where s is the squared four-momentum of the resonance. The denominator describes the energy dependence of the propagator. Since a resonance is related to the pole of the S-matrix, it should read $\frac{1}{s-\prod(s)}$ where $\prod(s)$ is the self-energy of the resonance:

$$\prod(s) = m^2(s) + i\sqrt{s}\Gamma(s). \tag{3.12}$$

In general, the function $\prod(s)$ is very complicated (for hadronic resonances, it is not possible to calculate in any fundamental way). For narrow resonances, (for example $\phi(1020)$) $\prod(s)$ can be approximated by constants: $\prod(s) = m_R^2 + im_R\Gamma_R$ where $m_R^2 \equiv m^2(m_R^2)$ is the pole mass and the propagator has a simple pole in the complex energy plane. In this context, if the resonance is narrow, the standard BW form $\frac{1}{s-m_R^2-im_R\Gamma_R}$ is obtained. However, if the resonance is broad (for example $\rho(770)$), it will not be described exactly by BW shape. A rigorous form can only be obtained if the total width is completely understood. However, most of the hadronic resonances do not satsify this requirement!

Gounaris-Sakurai(GS) parameterization

The real part of the self-energy function is $\mathrm{Re}\prod(s) = m^2(s)$, and is in general not constant. One can define the pole mass $m_R^2 \equiv m^2(m_R^2)$, and separate the constant and running-mass parts:

$$\mathrm{BW} = \frac{1}{s - \prod(s)} = \frac{1}{s - m_R^2 - \delta m^2(s) + im_R\Gamma_R(s)}, \tag{3.13}$$

where $\delta m^2(s)$ is the running pole mass as a function of s. The running mass can be related to the decay width $\prod(s)$ via the Kramers-Kronig dispersion relation

$$m^2(s) = m_R^2 + \frac{1}{\pi}\int_{s_0}^{\infty} \frac{m_R\Gamma_{tot}(s')}{(s-s')} ds'. \tag{3.14}$$

In practice, the total decay width is rarely understood well enough to calculate meaningful values for the running mass, and the mass is usually taken to be constant.

For some specific cases, effort has gone into understanding $\prod(s)$ in some detail. For example, in $\rho(770) \to \pi\pi$, G.J. Gounaris and J.J. Sakurai derived [23] $\prod(s)$ from an effective-range formula for the P-wave $\pi\pi$ scattering phase shift. This yields a modified propagator

$$\frac{1 + d \cdot \Gamma_R / m_R}{s - m_R^2 - \delta m^2(s) + i\, m_R \Gamma_R(s)}, \tag{3.15}$$

where $\delta m^2(s)$ is the correction to the propagator. Interested reader should refer to appendix A.2 for details. Eq. 3.15 becomes the standard parameterization for $\rho(770)$ resonances.

3.5 Spin Formalism

When a resonance has a non-zero spin, a proper description of the angular distribution on the Dalitz plot is required. To derive the expression, we start from the spin-sum rule:

$$\text{Spin Sum} = \sum_\lambda \varepsilon_\lambda^{\mu *} \varepsilon_\lambda^{\nu}. \tag{3.16}$$

For a scalar, there is no polarization vector associated with the decay vertex and the decay has uniform angular distribution. If we denote the spin function to be Z, then

$$Z = 1. \tag{3.17}$$

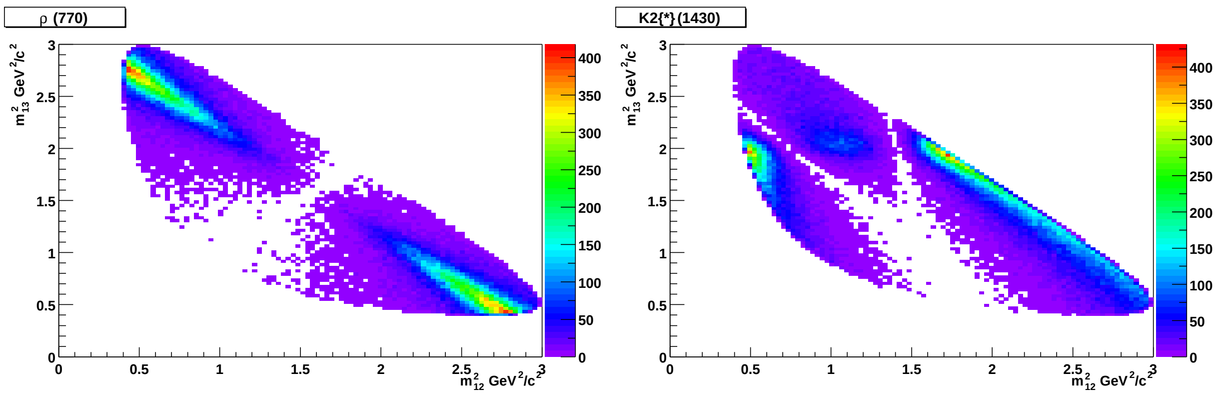

Figure 3.3: Simulated events in $D^0 \rightarrow K_S^0\pi^+\pi^-$ dalitz plot. **Left:**Spin one $\rho(770)$ resonance. **Right:** Spin two $K_2^*(1430)$ resonance, the angular distributions are very different.

For a vector (spin-1) resonance, the spin-sum in the numerator of Eq. 3.16 is evaluated to give

$$\sum_{\lambda} \varepsilon_{\lambda}^{\mu *} \varepsilon_{\lambda}^{\nu} = -g^{\mu\nu} + \frac{P_{AB}^{\mu} P_{AB}^{\nu}}{M_{AB}^2}, \tag{3.18}$$

where λ specifies the helicity state. Note that the second term in Eq. 3.18 ensures that the polarization vectors ϵ_μ are transverse: $p^\mu \epsilon_\mu = 0$. (See Sec. 3.5.1 later about this point.)

The procedure for higher-spin resonances involves a bit more algebra. For example, in the spin-2 case, the spin sum has been previously calculated [22] to be

$$\sum_{\lambda} \varepsilon_{\lambda}^{*\mu\nu} \varepsilon_{\lambda}^{\alpha\beta} = \frac{1}{2}\left(T^{\mu\alpha}T^{\nu\beta} + T^{\mu\beta}T^{\nu\alpha}\right) - \frac{1}{3}T^{\mu\nu}T^{\alpha\beta}, \tag{3.19}$$

where

$$T^{\mu\nu} = -g^{\mu\nu} + \frac{P^\mu P^\nu}{M^2}. \tag{3.20}$$

Once the spin-sum is calculated, we can insert the expression into Eq. 3.8 for a vector particle, or Eq. 3.9 for a tensor particle, and sum over the repeated indices to give the Lorentz invariant expression for the matrix element as a function of position in the Dalitz plot:[5]

$$\begin{aligned}
Z_0 &= 1 \qquad (3.21)\\
Z_1 &= M_{BC}^2 - M_{AC}^2 + \frac{(M_D^2 - M_C^2)(M_A^2 - M_B^2)}{M_{AB}^2}\\
Z_2 &= \Bigg[\left(M_{BC}^2 - M_{AC}^2 + \frac{(M_D^2 - M_C^2)(M_A^2 - M_B^2)}{M_{AB}^2}\right)^2 - \\
&\quad \frac{1}{3}\left(M_{AB}^2 - 2M_D^2 - 2M_C^2 + \frac{(M_D^2 - M_C^2)^2}{M_{AB}^2}\right)\\
&\quad \left(M_{AB}^2 - 2M_A^2 - 2M_B^2 + \frac{(M_A^2 - M_B^2)^2}{M_{AB}^2}\right)\Bigg].
\end{aligned}$$

where Z_0, Z_1, Z_2 are the spin functions for scalar,vector and tensor respectively.

3.5.1 Zemach Tensor vs Helicity model

In the previous section, the angular dependence is derived using the spin sum rule. Here we come to a subtle but important issue. In the spin-sum formula of Eq. 3.18:

$$\sum_{\lambda} \varepsilon_{\lambda}^{\mu\nu *} \varepsilon_{\lambda}^{\alpha\beta} = -g^{\mu\nu} + \frac{P^{\mu} P^{\nu}}{M^2} \qquad (3.22)$$

---

[5] Note in the ref. [22] there is a typo in the spin-1 formula. The labels A and B are swapped, introducing an overall extra minus sign.

what do we take for the M^2 in the denominator of the second term: m_{AB}^2 or m_R^2? If the former, this enforces transversality, $\varepsilon_\lambda^\mu (P_{ab})_\mu = 0$, and enforces a spin-1 current. This is the assumption built into the Zemach tensor formalism. However, if one uses Zemach tensors, for the W boson propagator, for example, the amplitude of $\pi^- \to W^- \to \mu\nu$ would be zero, and the pion would not decay! In the standard model, m_{W}^2 is used rather than m_{AB}^2 in the denominator of the second term, which is referred to as the "helicity model". When the W is far off-shell, it has an effective spin-zero component to its current[6], therefore it can couple to the spin-zero pion. Some physicists argue that the same argument should apply for the unstable resonances like ρ and $K^*(892)$. However, the choice of the Zemach tensor vs. helicity model is an unsettled question in the context of Dalitz plot analysis. To illustrate the difference, Fig. 3.4 shows a Monte Carlo simulation of $D_s \to f_2(1270)\pi^+$, where $f_2(1270) \to \pi\pi$ using Zemach Tensor vs. Helicity model. Clear differences in the interference pattern are visible.

Some effort has been expended on the $D_s \to \pi^-\pi^+\pi^+$ channel to answer this question experimentally. In this channel only the $\pi\pi$ system is involved and there is no evidence of a low mass scalar such as the $\sigma(500)$. It also has a large contribution from $f_2(1270)$ (roughly 15%). Figure 3.5 shows the actual data distribution of $D_s \to \pi^-\pi^+\pi^+$. It shows that if the helicity model is used then a large non-resonant term ($\sim$ 25%) is observed. If the Zemach tensor is used then the non-resonant term is reduced to $\sim$ 5%. There is evidence that the Zemach tensor model fits the Dalitz

---

[6] Note W is spin one and π is spin zero.

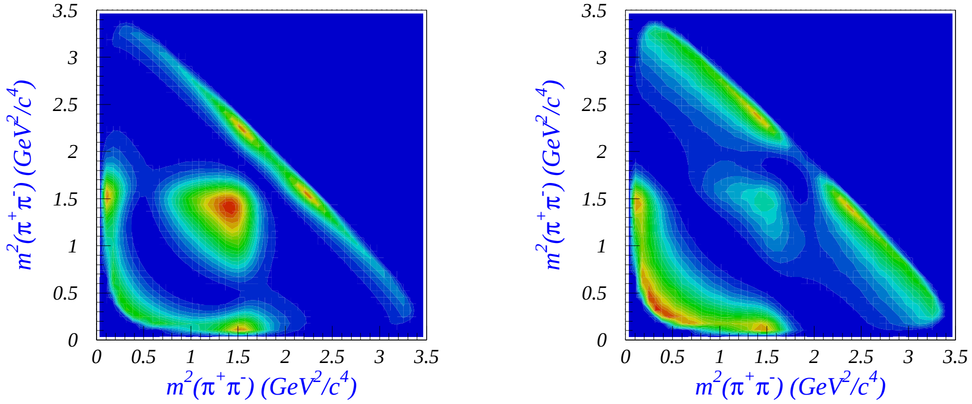

Figure 3.4: Monte Carlo simulation on $f_2(1270) \to \pi\pi$. Left: Zemach Tensor. Right: Helicity model. The difference between two is clearly visible.

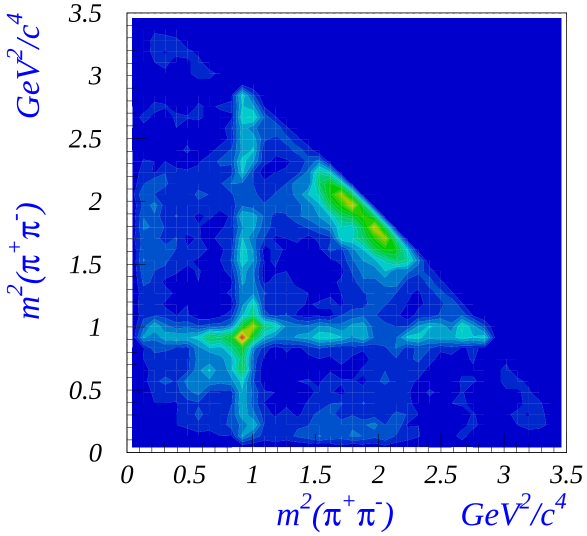

Figure 3.5: The actual $D_s \to \pi^-\pi^+\pi^+$ dalitz distribution of *BABAR* data.

plot better. If the helicity model does not fit the spin-2 component well, this requires increasing the non-resonant term to absorb the remaining events. However, there is no definite agreement in the HEP community yet.

3.6 Blatt-Weisskopf penetration factors

Next we return to the form factors F_D and F_r in Eq. 3.8. Quantum field theory assumes that all particles are point-like. However, in nuclear physics, the nucleus has finite extent. To account for this finite-size effect, form factors are placed on the vertex of the Feynman diagram to give the coupling constants a mass dependence. The classical treatment is done by Blatt and Weisskopf [24] and the vertex factors are referred to as Blatt-Weisskopf penetration factors. The interested readers should consult this classic text on nuclear physics for further details. The idea is briefly described here for complete reference.

The finite size of the decaying particle can be described crudely as a three-dimensioned gaussian distribution with a parameter R,

$$\Psi(r) = \frac{1}{(\pi R^2)^{\frac{3}{4}}} e^{-r^2/2R^2}. \tag{3.23}$$

The form factor $F(p)$ is given by its Fourier transform

$$F(p) = e^{-(Rp)^2/2} \approx 1 - \frac{(Rp)^2}{2} + O(Rp)^4. \tag{3.24}$$

Table 3.1: Blatt-Weisskopf penetration form factors, where p_r is the momentum of either daughter in the meson rest frame and p_{AB} is the momentum of either daughter in the candidate rest frame (same as p_r except the parent mass used is the two-track invariant mass of the candidate rather than the mass of the meson). R is the meson radial parameter.

Spin	Form Factor F_r
0	1
1	$\frac{\sqrt{1+R^2p_r^2}}{\sqrt{1+R^2p_{AB}^2}}$
2	$\frac{\sqrt{9+3R^2p_r^2+R^4p_r^4}}{\sqrt{9+3R^2p_{AB}^2+R^4p_{AB}^4}}$

Blatt and Weisskopf used this picture to calculate the barrier penetration factor. They assumed the potential for the finite size nucleus is given by the spherical-well potential. Recall in quantum mechanics that the solution of the three-dimensional spherical-well potential are the spherical Hankel functions. Blatt-Weisskopf barrier penetration factor is given by the logarithmic derivative of the Hankel wave functions evaluated at $r = R$. It amounts to a measure of the suppression of the process at non-zero angular momentum due to the centifugal barrier. The Blatt-Weisskopf formula is shown in Table 3.1.

3.7 Hadron Spectroscopy and K-matrix Theory

Hadron spectroscopy is a broad topic, and there are still many controversial issues left to resolve. In particular, the understanding of isoscalar scalars, with quantum numbers

$$J^{PC} = 0^{++},$$

is still very poor. Moreover, the existence of very broad isoscalar states, $\sigma(500)$ and $\kappa(800)$, commonly reported in various charm Dalitz plot analysis [25][26] is still controversial. It is also well known that the BW approximation is only valid if the resonance is narrow and does not overlap with other resonances. However, in the $J^{PC} = 0^{++}$ isoscalar sector, the resonances are broad and heavily overlapping, which violates the BW approximation. Figure 3.7 shows the $I = 0$ isoscalar $\pi\pi$ S-wave intensity plot taken from Ref. [27]. The various resonances are highly overlapping, and no simple BW peak is observed.

K-matrix theory is introduced because it can handle wide, overlapping resonances. K-matrix analysis is commonly used in scattering experiment where the model independent pole position can be determined. However, it is not a common practice to adopt K-matrix theory in the production environment. The theory is introduced here, and the production formalism is presented in the Dalitz plot context. The properties of the hadron and its BW parameters are discussed in the final section.

3.7.1 K-matrix theory

The K-matrix formalism provides an elegant way of expressing the unitarity of the S-matrix for processes of the type $ab \to cd$. It has been originally introduced by Wigner [28], and Wigner and Eisenbud [29], to study resonances in nuclear reactions.

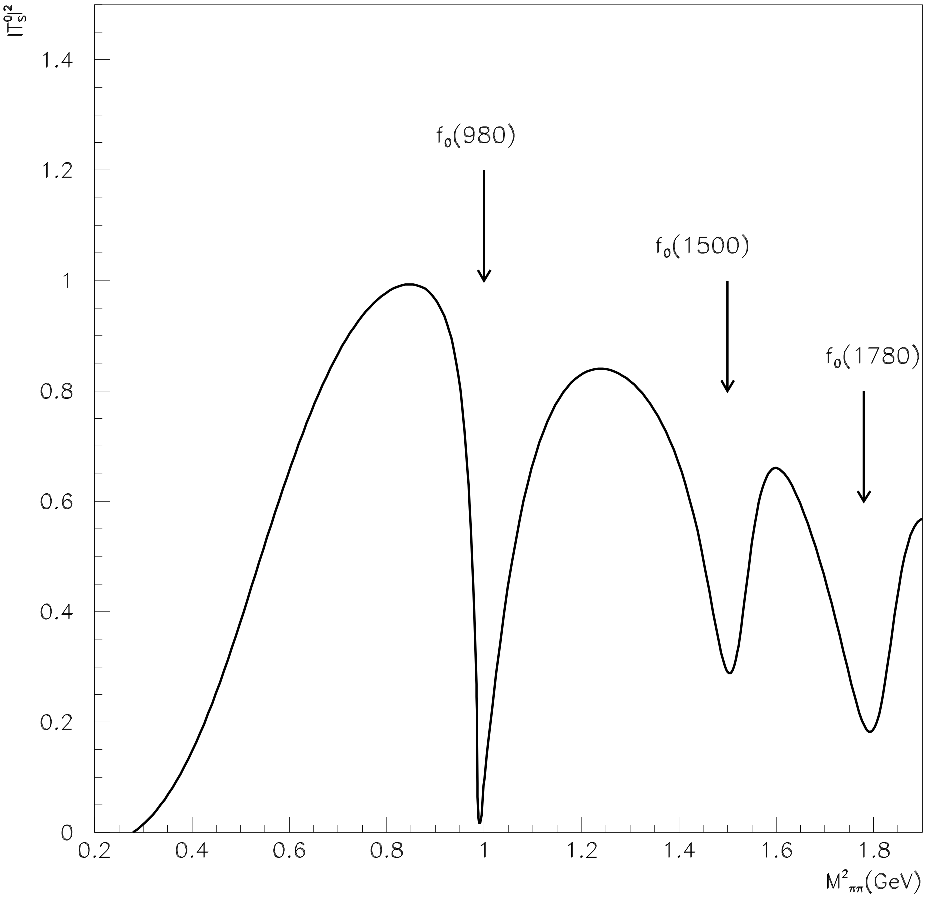

Figure 3.6: $I = 0$ Isoscalar $\pi\pi$ S-wave intensity. No simple Breit-Wigner peak structure is observed.

The first use in particle physics goes back to an analysis of resonance production in Kp scattering by Dalitz and Tuan [30].

S-matrix and T-matrix

S-matrix formalism was first developed by Heisenberg in 1942. In general, the amplitude for a transition from initial state $|i\rangle$ to the final state $|f\rangle$ is written as

$$S_{fi} = \langle f|S|i\rangle, \tag{3.25}$$

where S_{fi} is the scattering matrix. In practice, we define the transition operator T via

$$S = I + 2iT, \tag{3.26}$$

as we are not interested in the processes that are non-interacting.

Derivation of K-matrix based on unitarity

From the conservation of the probability, the scattering matrix S is unitary:

$$SS^{\dagger} = S^{\dagger}S = I, \tag{3.27}$$

and from the unitarity of the S matrix one obtains

$$T - T^{\dagger} = 2iT^{\dagger}T = 2iTT^{\dagger}, \tag{3.28}$$

In terms of the inverse operators, Eq. 3.28 can be rewritten

$$(T^{\dagger})^{-1} - T^{-1} = 2iI, \tag{3.29}$$

which may further be transformed into

$$(T^{-1} + iI)^{\dagger} = T^{-1} + iI. \tag{3.30}$$

One is now ready to introduce the K operator via

$$K^{-1} = T^{-1} + iI. \tag{3.31}$$

From Eq. 3.30 one finds that the K operator is Hermitian, $K = K^{\dagger}$.

From time-reversal invariance of S and T, it follows that the K operator must be symmetric, i.e. the K-matrix may be chosen to be real and symmetric. One can eliminate the inverse operators in Eq. 3.31 by multiplying by K and T from left and right, and vice versa, to obtain

$$T = K + iTK = K + iKT, \tag{3.32}$$

which shows that K and T operators commute, i.e. $[K, T] = 0$.

Solving for T, one obtains

$$T = K \cdot (I - iK)^{-1} = (I - iK) \cdot^{-1} K. \tag{3.33}$$

and

$$S = (I + iK) \cdot (I - iK)^{-1} = (I - iK) \cdot^{-1} (I + iK). \tag{3.34}$$

Note that T is complex only through the i that appears in this Eq. 3.33. In other words, T^{-1} has been explicitly broken up into its real and imaginary parts.(Eq. 3.31)

Combining Eq. 3.33 with Eq. 3.28, one finds that the unitarity condition takes on the simple form $ImT = |T|^2$, which is essentially the optical theorem. Finally, from Eq. 3.31, one obtains

$$ImT^{-1} = -I. \tag{3.35}$$

The Lorentz Invariant form

The transition amplitude T and the K-matrix defined in Eq. 3.31 are not Lorentz invariant. The invariant amplitude is defined through two-body wave functions for the initial and final states, and the process of the derivation involves proper normalization for two-particle state. The resulting invariant amplitude contains the inverse square root of the two-body phase-space element. The Lorentz-invariant amplitude, denoted $\hat{T}$, is given by:

$$T = \sqrt{\rho}\hat{T}\sqrt{\rho} \tag{3.36}$$

and

$$S = I + 2i\sqrt{\rho}\hat{T}\sqrt{\rho}, \tag{3.37}$$

where the phase-space matrix ρ is diagonal by definition

$$\rho_{ij} = \begin{pmatrix} \rho_i & & \\ & \ddots & \\ & & \rho_j . \end{pmatrix} \tag{3.38}$$

Here, $\rho_i = \frac{2q_i}{m}$, and q_i are the breakup momenta in the channel i. Following the same exercise, the lorentz-invariant form of K-matrix can be written as (after a few lines of algebra)

$$\hat{K}^{-1} = \hat{T}^{-1} + i\rho, \tag{3.39}$$

and the Lorentz form of T can be written as:

$$\hat{T} = (I - i\hat{K}\rho)^{-1} \cdot \hat{K} = \hat{K} \cdot (I - i\rho\hat{K})^{-1}. \tag{3.40}$$

3.7.2 P-vector formalism

In the previous section the K-matrix theory has been developed in the two-body scattering process $ab \to cd$. However, the K-matrix formalism can be generalized to describe the case of “production” of resonances in the decays of unstable particles. The key assumption is that the two-body system in the final state does not interact simultaneously with the rest of the final state. Here the so-called "P-vector formalism" is described which can be adopted in Dalitz plot analysis.

The P-vector formalism was proposed by I.J.R. Aitchison[31]. In the case of scattering, the Lorentz invariant T matrix is written as:

$$\hat{T} = (I - i\hat{K}\rho)^{-1} \cdot \hat{K}. \tag{3.41}$$

In the production environment, the production amplitude F can be written as

$$\hat{F} = \underbrace{(I - i\hat{K}\rho)^{-1}}_{\text{propagator}} \cdot \hat{P}, \tag{3.42}$$

where the term P is the initial production vector, and the term $(I - i\hat{K}\rho)^{-1}$ is the scattering propagator. In the production environment, the system is produced initially in the state $\hat{P}$, and propagates into the final state via the $(I - i\hat{K}\rho)^{-1}$ operator. Notice that the introduction of the term $(I - i\hat{K}\rho)^{-1}$ guarantees consistency between scattering and production as they contains same set of K-matrix propagator $(I - i\hat{K}\rho)^{-1}$. Figure 3.7 shows the pictorial representation of the P-vector process.

3.8 K-matrix examples

Several examples are given here where a large class of form factor can be derived from K-matrix theory, which demostrates the validity of the K-matrix model.

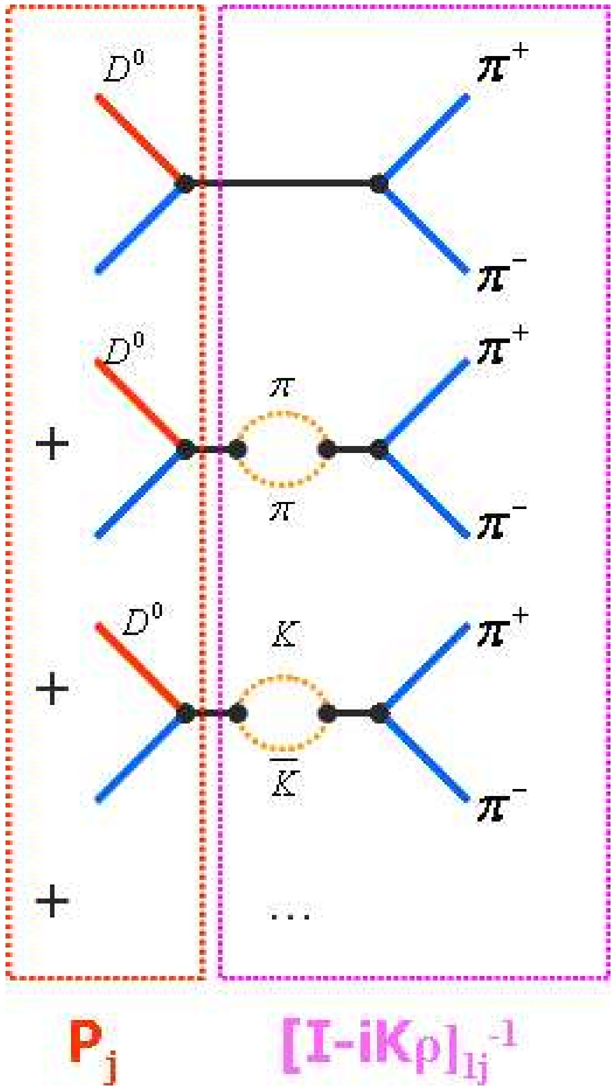

Figure 3.7: The P-vector formalism. The vector P is responsible for the production process, while the term $(I - i\hat{K}\rho)^{-1}$ is the scattering propagator.

Simple Breit-Wigner Formula

Consider now an isoscalar $\pi\pi$ scattering in S-wave below $\sqrt{s} = 1\,\text{GeV}$. This is a single-channel problem and unitarity is rigorously maintained. Let the K-matrix be

$$K = \tan\delta = \frac{m_0\Gamma(s)}{m_0^2 - s}. \tag{3.43}$$

From Eq. 3.33, we obtain

$$\begin{aligned}
T &= K\cdot(1-iK)^{-1} && (3.44)\\
&= \frac{m_0\Gamma(s)}{m_0^2 - s}\cdot\frac{m_0^2 - s}{m_0^2 - s - im_0\Gamma(s)} && (3.45)\\
&= \frac{m_0\Gamma(s)}{m_0^2 - s - im_0\Gamma(s)} && (3.46)
\end{aligned}$$

which is the well-known BW formula. Notice in the Eq. 3.43 the K-matrix pole position occurs when $s = m_0^2$, which is when the phase shift δ passes 90 degrees. As an illustrative example, the BW lineshape and the phase shift for $\rho(770)$ are shown in Fig. 3.8.

Coupled-channel Breit-Wigner (Flatté Formula)

Consider next a two-channel problem (eg. $f_0(980) \to \pi\pi, K\bar{K}$) in which the S-matrix may be expressed as 2×2 matrices. In the K-matrix representation, illustrated in

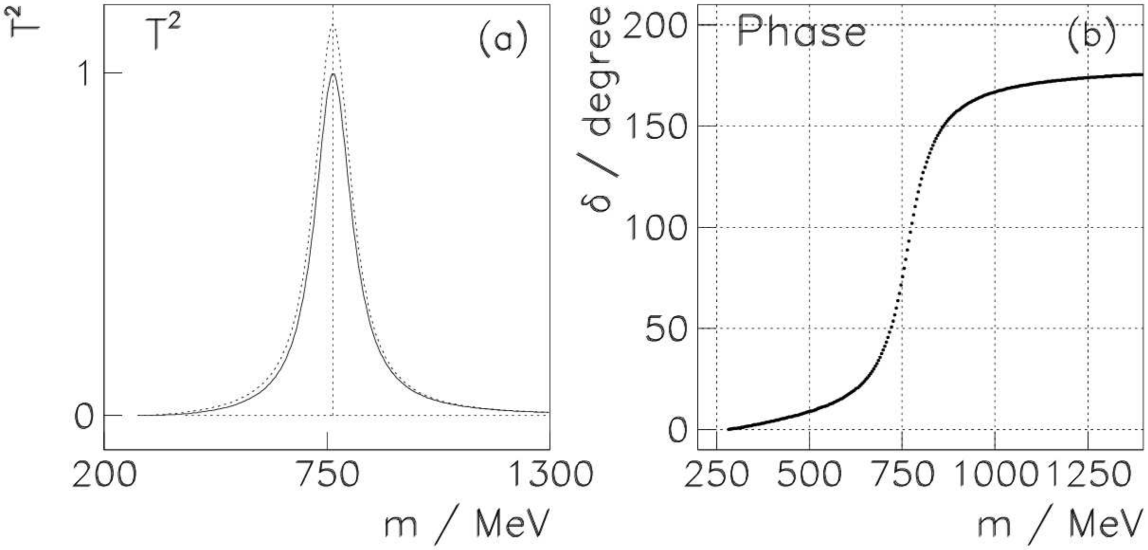

Figure 3.8: **(a)**Breit-Wigner amplitude squared $|\rho T|^2$ as a function of invariant $\pi\pi$ mass. The amplitude $|T|^2$ is superimposed as dotted line. **(b)** $\pi\pi$ phase shift δ, which reaches 90° at resonance mass.

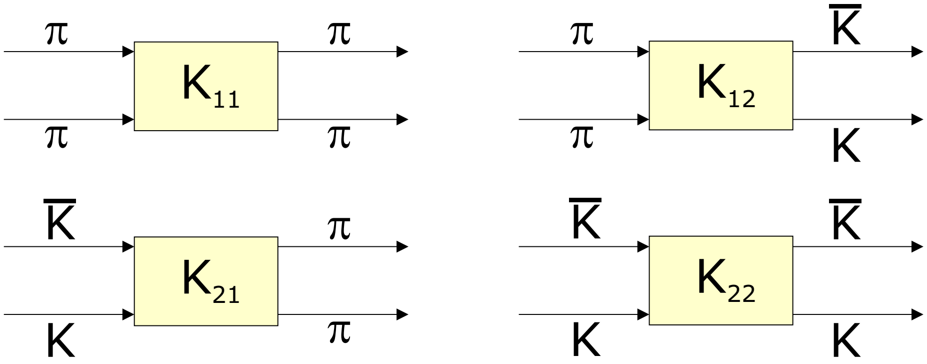

Figure 3.9: Scattering process using a K-matrix propagator. The boxes hide the actual process.

Fig. 3.9, let

$$K = \begin{pmatrix} K_{11} & K_{12} \\ K_{21} & K_{22} \end{pmatrix} = \begin{pmatrix} K_{\pi\pi\to\pi\pi} & K_{\pi\pi\to K\bar{K}} \\ K_{K\bar{K}\to\pi\pi} & K_{K\bar{K}\to K\bar{K}}, \end{pmatrix} \tag{3.47}$$

where $K_{12} = K_{21}$ and the K_{ij} are real, as K-matrix is real and symmetric. We could parameterize the elements of the K-matrix as

$$\begin{aligned} K_{11} &= g_\pi^2 \frac{m_0\Gamma}{(m_0^2 - s)}, \\ K_{22} &= g_K^2 \frac{m_0\Gamma}{(m_0^2 - s)}, \\ K_{12} = K_{21} &= g_\pi g_K \frac{m_0\Gamma}{(m_0^2 - s)}. \end{aligned} \tag{3.48}$$

Then, from Eq. 3.40, one finds

$$T = \frac{m_0\Gamma}{m_0^2 - s - im_0\Gamma(\rho_1 g_\pi^2 + \rho_2 g_K^2)} \begin{pmatrix} g_\pi^2 & g_\pi g_K \\ g_\pi g_K & g_K^2 \end{pmatrix}, \tag{3.49}$$

where ρ_1 and ρ_2 are the phase-space factors,

$$\rho_i(s) = \sqrt{1 - \frac{(m_{i1} + m_{i2})^2}{s}}.$$

This is the Flatté formula [32]. Note that both T and S must satisfy analyticity, which implies that $\rho(s)$ requires analytic continuation when the energy is below threshold.

From the K-matrix point of view, the coupling constants g_π and g_K are process-dependent. Therefore, different processes will have different values of g_π and g_K,

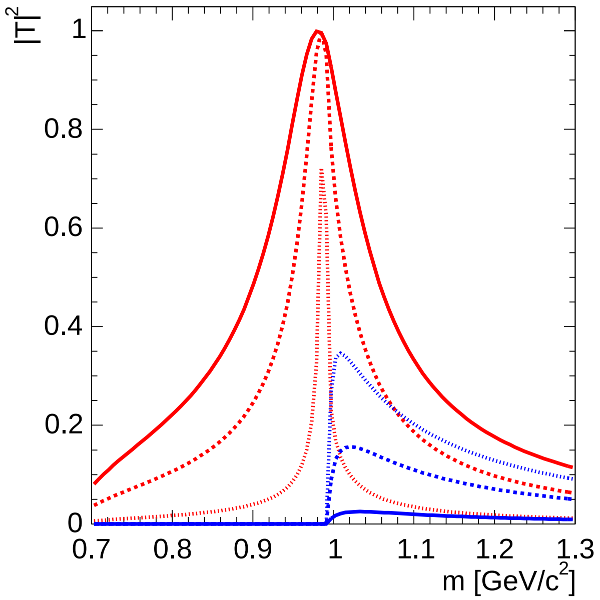

Figure 3.10: Effect of coupling variations in the Flatté formula. The stronger the coupling on the second channel, the more dramatic are the effects on the lineshape. The solid, dashed and dotted curves represent the coupling function $g_1^2/g_2^2 = 10$ to 1 and 0.1 respectively for the two channels.

which parameterizes the coupling to $\pi\pi$ and $K\bar{K}$ channels. Figure 3.10 shows the effect of coupling variations in the Flatté formula. The red curve (with nice BW structure) shows the coupling to $\pi\pi$ and the blue curve (shows up only above 1 GeV) shows the coupling to $K\bar{K}$.

This effect is clearly seen in charm meson decay. In $D_s^+ \to \pi^-\pi^+\pi^+$, the $f_0(980)$ is strongly coupling to $\pi\pi$ and therefore shows a clear Breit-Wigner peak, while in $D^0 \to K_S^0\pi^+\pi^-$ it is strongly coupled to $K\bar{K}$ and shows an abrupt cusp around 1 GeV. Figure 3.11 shows the different lineshape for $f_0(980)$ in the $D_s^+ \to \pi^-\pi^+\pi^+$ and $D^0 \to K_S^0\pi^+\pi^-$ channels around 1 GeV.

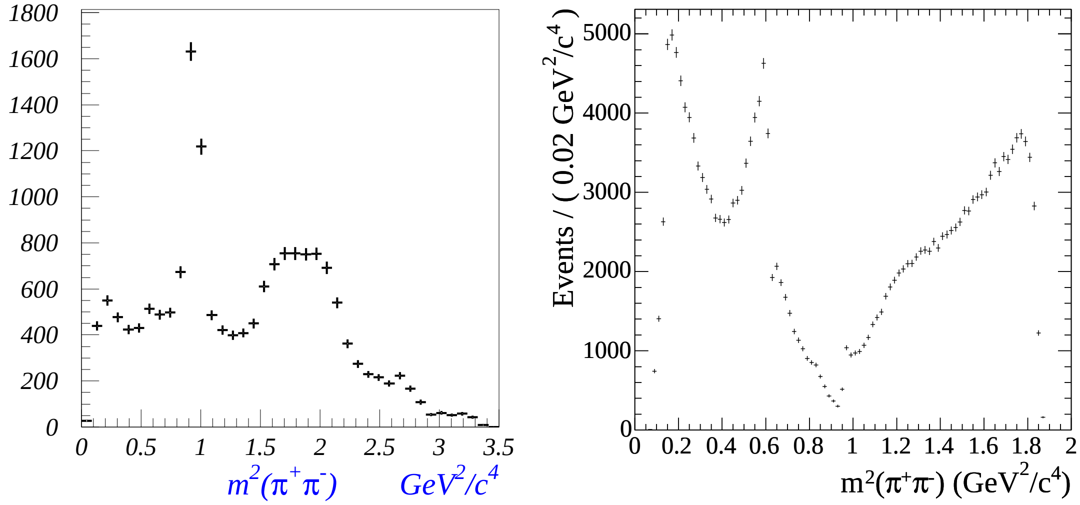

Figure 3.11: **Left:** Dalitz plot projection on $D_s^+ \rightarrow \pi^-\pi^+\pi^+$, where the BW is observed near 1 GeV^2/c^4. **Right**: Dalitz plot projection on $D^0 \rightarrow K_S^0\pi^+\pi^-$, notice a sharp abrupt cusp around 1 GeV^2/c^4, indicating the opening up of $K\bar{K}$ channel.

Overlapping Resonances

Consider again in $\pi\pi$ scattering. Suppose two resonances exist with the pole masses m_a and m_b. The prescription for the K-matrix in this case is that

$$K = \frac{m_a\Gamma_a(m)}{m_a^2 - s} + \frac{m_b\Gamma_b(m)}{m_b^2 - s}. \tag{3.50}$$

If m_a and m_b are far apart relative to the widths, the K-matrix is dominated either by the first or second term, depending on whether m is near m_a or m_b. The corresponding T-matrix is then given merely by the sum

$$T \sim \frac{m_a\Gamma_a(m)}{m_a^2 - s - im_a\Gamma_a(m)} + \frac{m_b\Gamma_b(m)}{m_b^2 - s - im_b\Gamma_b(m)}. \tag{3.51}$$

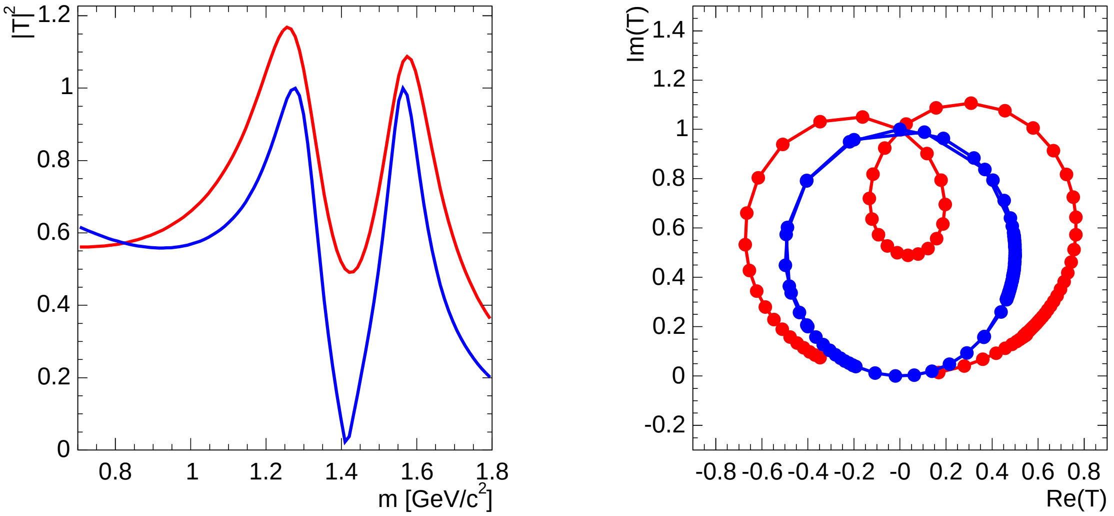

Figure 3.12: Two overlapping resonances with the parameters: $m_A = 1275\,\mathrm{MeV}/c^2, \Gamma_A = 185\,\mathrm{MeV}/c^2, m_B = 1565\,\mathrm{MeV}/c^2, \Gamma_B = 150\,\mathrm{MeV}/c^2$. **Left:** shows the result of adding the resonance poles in the K-matrix(blue line). The red line corresponds to the sum of the two BW amplitude ($|T_A + T_B|^2$), which violates unitary where $|T|^2 > 1$. Note that the intensity does not drop to zero between the resonance peaks. **Right:** shows the corresponding argand diagrams for the isobar model(in red) and the K-matrix(in blue). Note that the amplitude in the K-matrix model always remains on the unitary circle.

Therefore, simply adding two BW shapes is only valid when two resonances are far apart.($|m_a - m_b| \gg \Gamma_a, \Gamma_b$) See Fig. 3.12 for the details.

In the limit when $m_a = m_b$, then the transition amplitude becomes

$$T = \frac{m_a(\Gamma_a(m) + \Gamma_b(m))}{m_a^2 - m^2 - im_a(\Gamma_a(m) + \Gamma_b(m))}. \tag{3.52}$$

This shows that the result is a single BW form but its total width is now the sum of two individual widths.

LASS formula as K-matrix

In the early 1990's LASS [33] at SLAC performed a scattering experiment $K^- p \to K^- \pi^+ n$ at 11 GeV to study the $K\pi$ system. A scalar resonance $K^*(1430)$ was found near 1.4 GeV with a broad width (300 MeV) that did not exhibit the usual BW lineshape. LASS adopted effective-range parameterization to model the lineshape of the $K^*(1430)$ resonance

$$T = \sin\delta_b e^{i\delta_b} + e^{2i\delta_b} \sin\delta_r e^{i\delta_r}, \tag{3.53}$$

where

$$\begin{aligned} \cot\delta_r &= \frac{m_0^2 - s}{m_0 \Gamma(s)} \qquad (3.54) \\ \cot\delta_b &= \frac{1}{aq} + \frac{rq}{2}. \qquad (3.55) \end{aligned}$$

Here, a is the scattering length and r is the effective range while q is the four-momentum of the spectator particle in the resonance frame,

$$q = \frac{\sqrt{(s - (m_K + m_\pi)^2)(s - (m_K - m_\pi)^2)}}{4s}. \tag{3.56}$$

Equation 3.53 is not easy to interpret at first glance. However, the physics is transparent in the K-matrix framework. Consider the following K-matrix:

$$K = \tan(\delta_r + \delta_b), \tag{3.57}$$

which from Eq. 3.33 leads to the following T-matrix

$$\begin{aligned} T &= K \cdot (1 - iK)^{-1} & (3.58) \\ &= \sin\delta_b e^{i\delta_b} + e^{2i\delta_b} \sin\delta_r e^{i\delta_r}. & (3.59) \end{aligned}$$

This formula is exactly the LASS parameterization. The physics in K-matrix framework is now apparent: the rapid (resonance) phase shift is coming from the term δ_r (note that the δ_r is same as K-matrix in Eq. 3.43 and the δ_b corresponding to non-resonant slow rising phase shift in Eq. 3.55.)

3.9 Model dependence of BW parameters

In this section the BW mass and width parameters and the relationship to the properties of hadrons are discussed. This subject can be confusing and it is therefore worth to explore in more detail.

A resonance gives rise to a peak in a cross-section in the scattering experiment. Typically, a BW amplitude is adopted to describe the lineshape and its mass and width are extracted. As described in Sec. 3.3, for narrow resonances, the self energy of the propagator $\prod(s)$ is approximated by a constant: $\prod(s) = m_R^2 + im_R\Gamma_R$. In fact, from the S-matrix point of view, the pole of the S-matrix is the most fundamental definition of a hadron, regardless of how the state appears in the experiment. In the case of the narrow, isolated resonance, there is a close connection between the position of the pole in the complex energy plane and the peak we observe in experiments necessarily measured on the real axis. However, when a resonance is overlapping with other resonances, this close connection is lost. Here three examples are given to demonstrate this problem.

Δ(1236) resonances

By 1971, the $\Delta(1236)$ resonance had been observed in several different channels. Different experiments under a variety of experimental conditions reported varying estimates for the BW mass and width. At the time, the PDF had difficulty combining the various results, and concluded that [34] "the mass and width of $\Delta(1236)$ are in a state of flux; therefore we do not quote any errors in the table."

> "A year later, it was recognized that this problem can be solved if we take the mass and width to be given by the actual pole position of $\Delta(1236)$ in the complex energy plane. [35]"

In summary, PDG found that different parameterizations of the lineshape,

- $\tan\delta = \frac{m_0\Gamma(s)}{m_0^2 - s}$ Breit-Wigner

- $\tan\delta = \frac{\gamma(s)}{2(m_0-\sqrt{s})}$ Layson
- $\tan\delta = \frac{m_0\Gamma(s)}{2s(m_0^2-s)}$ Chew-Low
- $q^3\cot\delta = \sum_{n=1}^{N} a_n q^{2q-2}$ Polynomial

can all fit the data well. However, the resonance parameters, (mass and width) are highly model-dependent, ie. these values are not unique. This discrepancy is removed if we take the mass and width to be given by the actual pole position of the $\Delta(1236)$ in the complex energy plane. The complex pole position of $\Delta(1236)$, which is determined to be $M_{\text{pole}} = 1211.11 \pm 0.24\,\text{MeV}$, $\Gamma_{\text{pole}} = 100.01 \pm 0.56\,\text{MeV}$ is essentially process- and parameterization-independent.

$\rho(770)$ **resonance**

As a second example we consider the $\rho(770)$ in greater detail. The Breit-Wigner parameters are measured with different processes, for example in $e^+e^- \to \pi^+\pi^-$, τ decays, $p\bar{p}$ annihilation, hadroproduction, photoproduction process etc. It is found that the mass and width of the $\rho(770)$ meson measured in these processes are not consistent. Again PDG had difficulty averaging the values. Benayoun, O'Connell and Williams *et al* [36] searched the pole of $\rho(770)$ in the complex energy plane and found the complex pole position lies in the range

$$M_{\text{pole}} = 756 - 759\,\text{MeV} \tag{3.60}$$

$$\Gamma_{\text{pole}} = 140 - 145\,\text{MeV} \tag{3.61}$$

(The spread is less than 5 MeV), no matter which parameterization is used or which production environment. However, the specific measured BW mass and width quoted by the experiments has a large spread:

$$M_{\mathrm{BW}} = 763 - 780\,\mathrm{MeV} \tag{3.62}$$

$$\Gamma_{\mathrm{BW}} = 141 - 157\,\mathrm{MeV} \tag{3.63}$$

(The spread is more than 15 MeV with error typically ± 1 MeV). This is further evidence that the BW parameters are model and process dependent. Figure 3.13 shows the 2006 PDG average of the BW mass and width of $\rho(770)$. Despite the high statistics from CMD2 and KLOE, the difference is still clearly visible. Figure 3.14 shows the results from Benayoun *et al* [36] for the complex pole position of $\rho(770)$. The BW parameters (cross) are scattered around but the complex pole position(denoted by $\otimes$) are essentially same.

The $K_0^*(1430)$ resonances

In the third example we point out that the mass and width parameters are also dependent on the parameterization on the non-resonant term[7]. As was shown in the Sec. 3.8, the lineshape of the $K\pi$ S-wave obtained from LASS experiment is parameterized as

$$T = \sin\delta_b e^{i\delta_b} + e^{2i\delta_b}\sin\delta_r e^{i\delta_r} \tag{3.64}$$

---

[7] This has a great effect on the $\pi\pi$ phase measurement in $D^0 \to K_S^0\pi^+\pi^-$ dalitz plot analysis

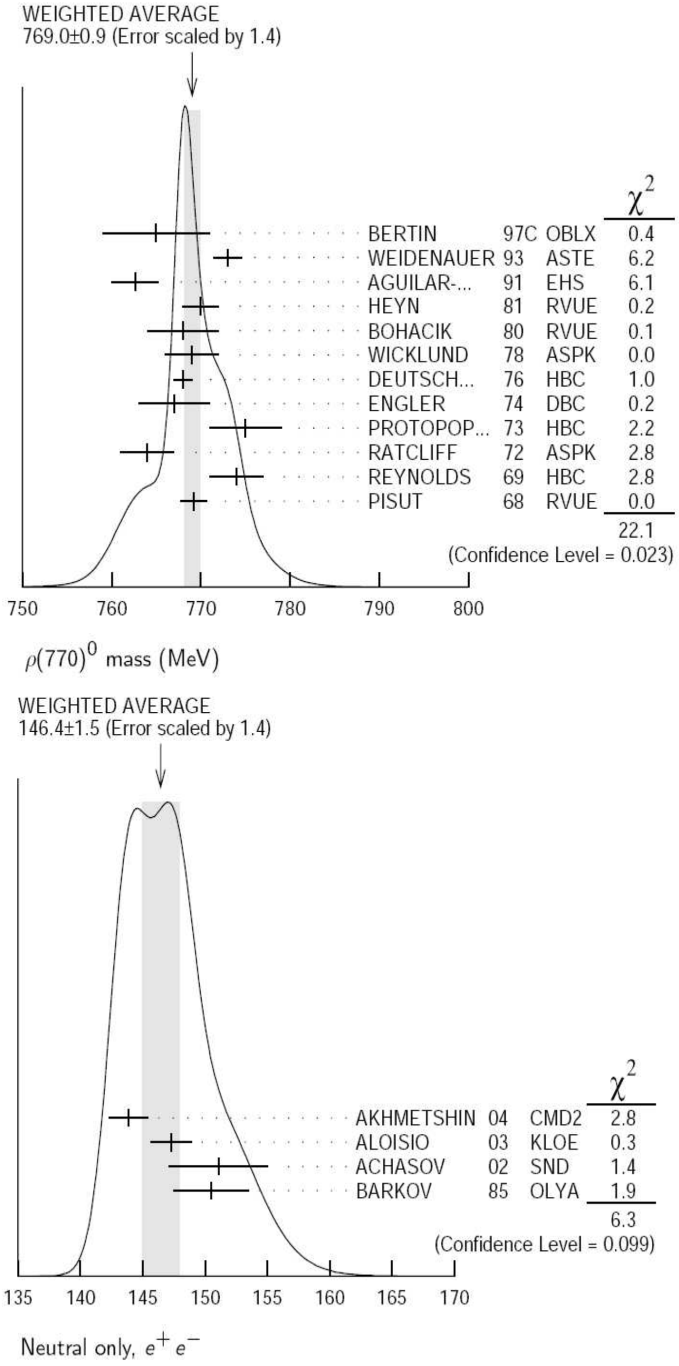

Figure 3.13: Weighted average of $\rho(770)$ BW parameters. (Top) Different measurements report different BW mass parameters. (Bottom) With more than one million events collected in the $e^+e^- \to \pi^+\pi^-$ process, the $\rho(770)$ width is still inconsistent. [20]

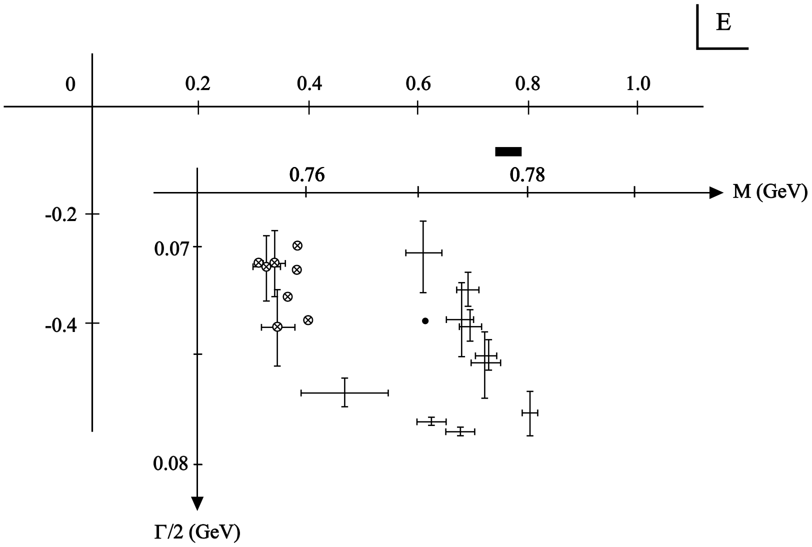

Figure 3.14: The complex energy plane of $\rho(770)$. Both BW mass and width parameters (cross) and their corresponding pole mass and width parameters (denoted by $\otimes$) are plotted. The complex pole position is clearly process and parameterization independent. The reference can be found in the paper by Benayoun *et al. [36].*

where

$$\cot \delta_b = \frac{1}{aq} + \frac{rq}{2}. \tag{3.65}$$

Note that $\cot \delta_b$ models the slow rising non-resonant contribution. To demonstrate that the BW mass and width are parameterization dependent, Monte Carlo simulation study was performed. We generated 30K events according to the measurement reported by LASS. An alternative model parameterization of δ_b was used to study the effect of mass and width of the resonances parameters. As an illustrative purpose, an alternative non-resonant parameterization(3rd order polynomial) is used: [8]

$$\cot \delta_b = aq + rq^2 + bq^3 \tag{3.66}$$

---

[8] Any background model will work as long as they fit the data well.

BW mass(generated)	1430(fixed) MeV
BW width (generated)	279(fixed) MeV
BW mass(LASS)	1431± 4 MeV
BW width(LASS)	271± 6 MeV
BW mass(alternative)	1453± 5 MeV
BW width(alternative)	241± 7 MeV

Table 3.2: Measured $K_0^*(1430)$ BW parameters using simulated events generated by the LASS model.

The measured mass and the width are shown in the Table 3.2. The variation with the parameterization of the non-resonant component is clear. In fact, in the original LASS paper, it mentioned the same problem [33]:

> “These resonance parameters are correlated with the background parameters, and can change significantly when different background forms are used.”

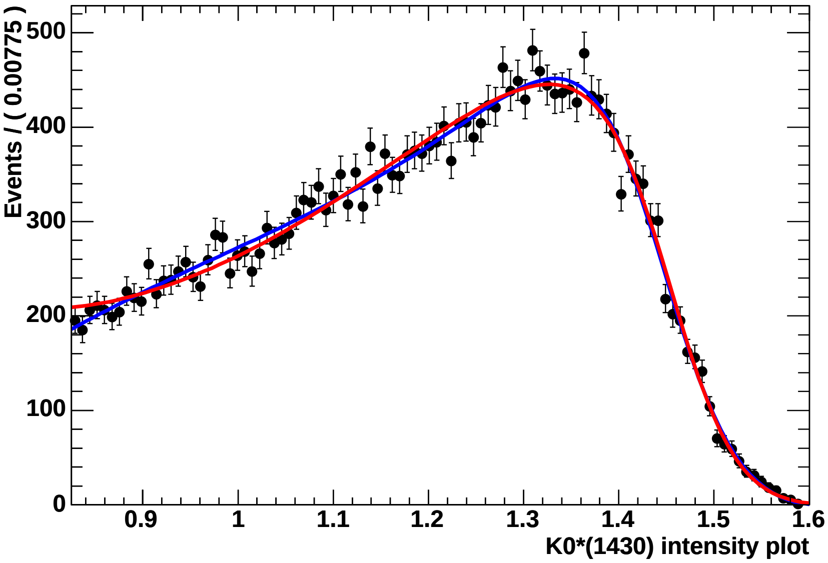

Figure 3.15: Simulated $K_0^*(1430)$ intensity plot with parameters taken from the LASS parameterization. Blue line: The fit using standard LASS parameterization. Red line: The fit using alternative parameterization. Note that both background parameterization describe the data well, although the resulting mass and width parameters are very different.

Chapter 4

$D^0 \rightarrow K^0_S\pi^+\pi^-$ Dalitz plot analysis

4.1 Introduction

The dynamics of charmed-meson decays have been studied extensively during the past decade. Dalitz-plot analysis of three-body D decays has proved to be a powerful tool to investigate the effect of the resonance structure, interference pattern, and final-state interaction. Moreover, the Dalitz-amplitude parameterization of the $D^0 \rightarrow K^0_S\pi^+\pi^-$decay is essential for the measurement of the γ of the Unitarity Triangle [17]. In this context, a Dalitz plot analysis of the $D^0 \rightarrow K^0_S\pi^+\pi^-$decay was performed as part of the first *BABAR* measurement of γ using this technique [37][38]. The Dalitz amplitude was parameterized as a sum of relativistic BW resonances, including form factors and a term describing the angular distribution of the two-body decay of each intermediate state.

However, this parametrization works well only in the case of narrow, isolated resonances. In fact, resonances are associated generally with the poles of the S matrix in the complex energy plane, and the Breit Wigner amplitude corresponds to only the most elementary type of the possible extrapolations from the physical region to the pole position in the complex energy plane. In the case of broad resonances that overlap significantly, a more complex formalism is required. This is particularly true for the S-wave component of the $D^0 \to K^0_S\pi^+\pi^-$decay.

The K-matrix formalism is an approach ideally suited to the study of overlapping resonances in multichannel decays. Although this approach was developed in the context of two-body scattering, it can be generalized to the case of resonance production in multi-body decays when the two-body system in the final state is isolated, and the two particles do not interact simultaneously with the rest of the final state in the production process (isobar model). In addition, the K-matrix formalism provides a direct way of imposing the two-body unitarity constraint that is not guaranteed in the case of the BW model.

4.2 $D^0 \to K_S^0\pi^+\pi^-$ selection

The D^0 and D^* reconstruction

The $D^0 \to K_S^0\pi^+\pi^-$data sample is reconstructed from continuum $e^+e^- \to c\bar{c}$ events through the following decay chain:

$$\begin{aligned} D^{*+} &\to D^0\pi^+ \\ D^0 &\to K_s\pi^+\pi^-, \end{aligned} \tag{4.1}$$

Selecting D^0 from the D^* decay has a superior advantage that the flavor of the D^0 can be tagged via the slow pion from the D^*, and the purity can be significantly improved via the mass difference between $\Delta m = m_{D^*} - m_{D^0}$.

The neutral kaon is constructed from pairs of oppositely-charged tracks assumed to be pions. The di-pion mass is required to be in the region $[0.488 - 0.508]\,\mathrm{GeV}/c^2$, corresponding to 3σ standard deviations around the nominal K_S^0 mass. The probability of the vertex-fit χ^2 must be greater than 0.001.

In order to remove fake K_S^0 candidates, the K_S^0 decay distance from the D^0 vertex is required to be greater than 0.4 cm. The angle $\alpha_{K_S^0}$ between the reconstructed K_S^0 momentum and its flight length (vector from the the D^0 vertex to the K_S^0 vertex) is required to satisfy $\cos\alpha_{K_S^0} > 0.99$. These cuts are aimed at rejecting fake K_S^0, and in particular they remove the possible contamination from decays of D^0 into four pions. In order to improve the momentum resolution, mass constraint is applied to K_S^0 and

D^0 while constructing the candidates. The center-of-mass (CM) momentum of the D^0 candidate is required to be greater than $2.2\,\mathrm{GeV}/c$ to remove D^0 coming from B decays. The D^0 candidate is reconstructed with the K_S^0 candidate and with two opposite-charged pions, while the D^* candidate is reconstructed combining the D^0 candidate with a pion satisfying $p < 0.6\,\mathrm{GeV}/c$. The probability of the resulting D^* vertex-fit χ^2 must be greater than 0.001.

Final $D^0 \to K_S^0\pi^+\pi^-$ selection

The final selection is based on two highly discriminating variables: D^0 mass M_D, and the mass difference $\Delta m = M_{D^*} - M_{D^0}$, where M_{D^*} is the reconstructed mass of the $D\pi$ combination. The Δm distribution (Fig. 4.1) has been fitted with a sum of two Gaussian distributions for signal, and a threshold function,

$$\Delta m_{\mathrm{bkg}} = \left(1 - e^{\frac{-(\Delta m - \Delta m_0)}{c}}\right)\left(\frac{\Delta m}{\Delta m_0}\right)^a + b\left(\frac{\Delta m}{\Delta m_0} - 1\right), \tag{4.2}$$

for background. Signal candidates are selected in the range $\pm 1.4\,\mathrm{MeV}/c^2$ ($\sim 2\sigma$) around the mean of the Δm distribution.

The M_{D^0} distribution has been fitted with a sum of two Gaussian distributions for signal, and a first-order polynomial for the background. Figure 4.1 shows the D^0 mass spectrum and the result of the fit. We require a reconstructed D^0 mass within $11\,\mathrm{MeV}(\sim 2\sigma)$ of the nominal D^0 mass.

After all the requirements, a sample of 215449 events with a purity of $S/(S+B) =$

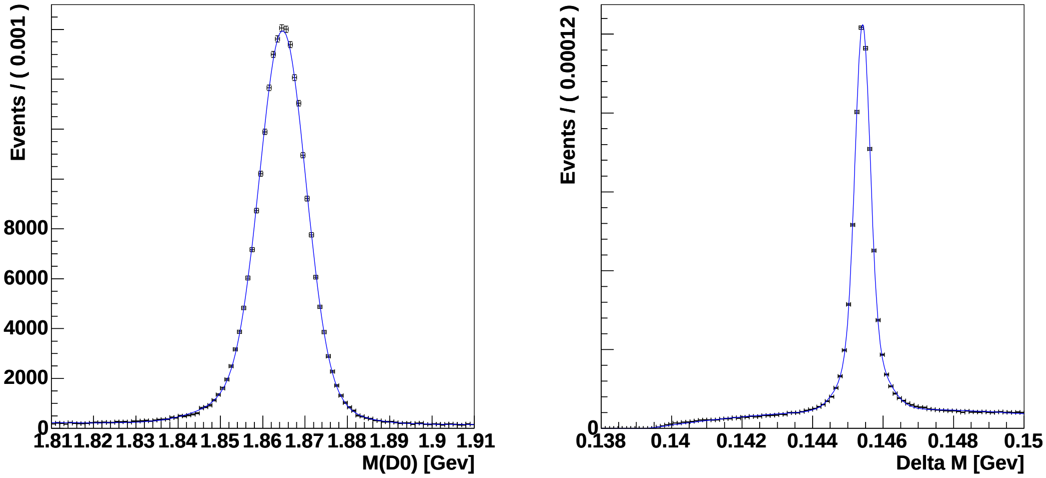

(a) $M(K_s\pi^+\pi^-)_{D^0}$

(b) $M_{D^*} - M_{D^0}$

Figure 4.1: Distributions of M_{D^0} and Δm and the fit results.

98.1% is obtained. Figure 4.2 shows the Dalitz plot distribution and Fig. 4.3 shows the corresponding projections.

4.3 Background composition

In order to estimate the background composition, the same selection criteria is applied to the continuum background (uds, $c\bar{c}$), and $B\bar{B}$ generic Monte Carlo samples. The M_{D^0} distributions of the different Monte Carlo components and the Data-MC comparison are shown in Fig. 4.4. The fraction of the wrong-flavor D^0 is less than 0.1% and is neglected.

A Monte Carlo study gives a purity of 98.9%, which is consistent with the one

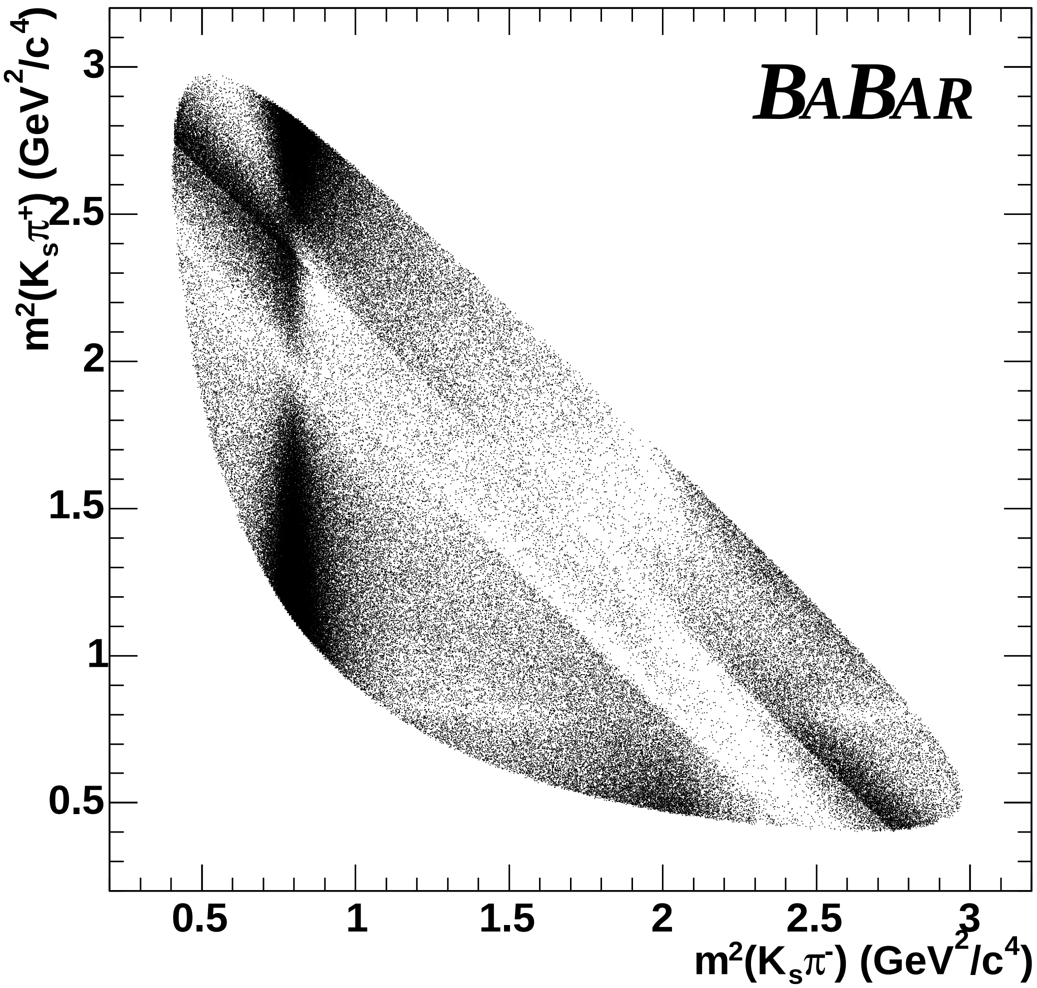

Figure 4.2: Dalitz plot projection in $m^2(K_s\pi^+)$ vs. $m^2(K_s\pi^-)$ for the decay $D^0 \rightarrow K_S^0\pi^+\pi^-$.

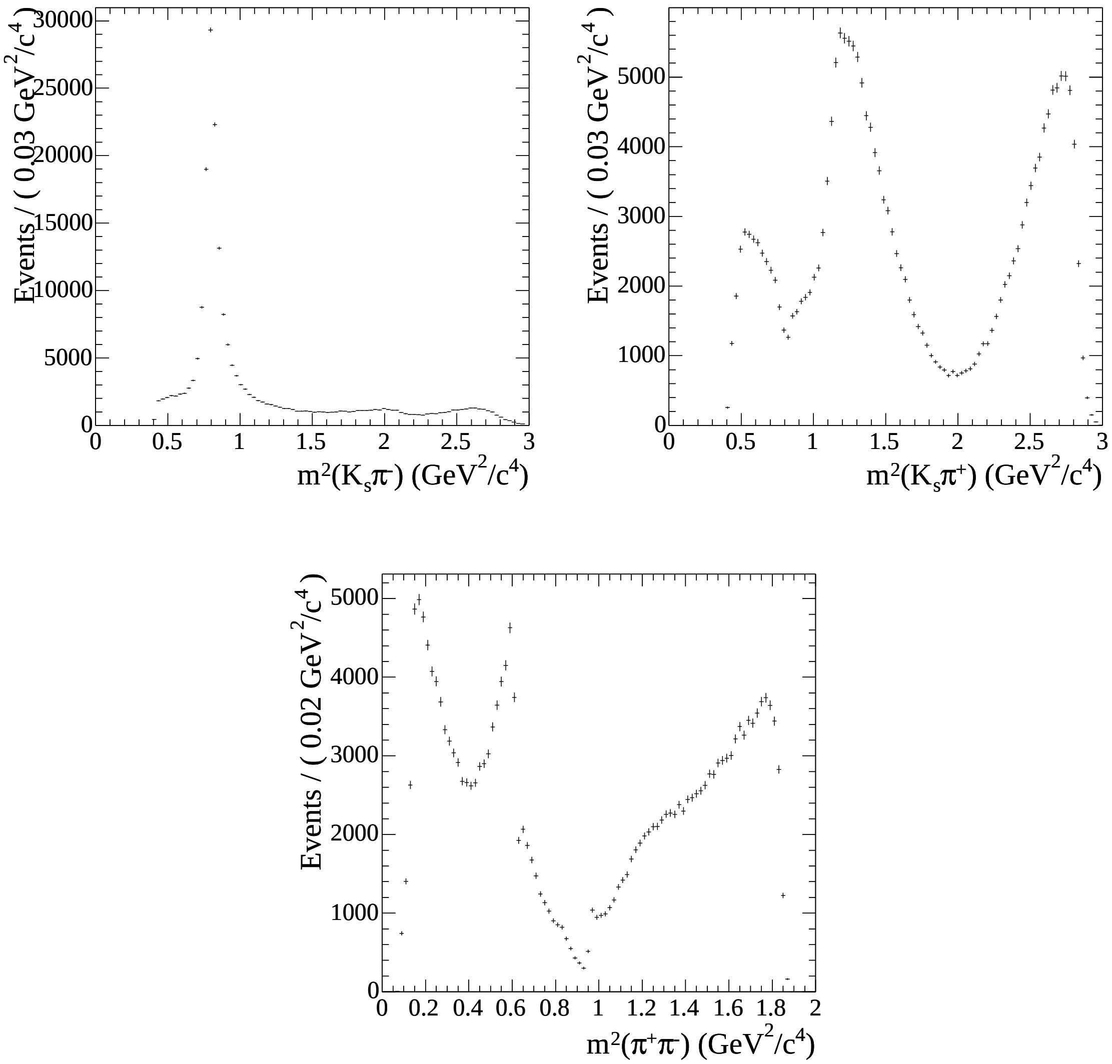

Figure 4.3: $D^0 \rightarrow K_S^0\pi^+\pi^-$Dalitz plot projections. **Top Left:** Dalitz projection in $m^2(K_s\pi^+)$ channel, a strong $K^*(892)$ is clearly seen. **Top Right:** Dalitz projection in $m^2(K_s\pi^-)$ channel. **Bottom:** Dalitz projection in $\pi\pi$ channel. A clear $\rho - \omega$ mixing is seen around 0.6 GeV^2/c^4, and the cusp rise around 1 GeV^2/c^4, which corrsponding to $f_0(980)$(see sec. 3.8).

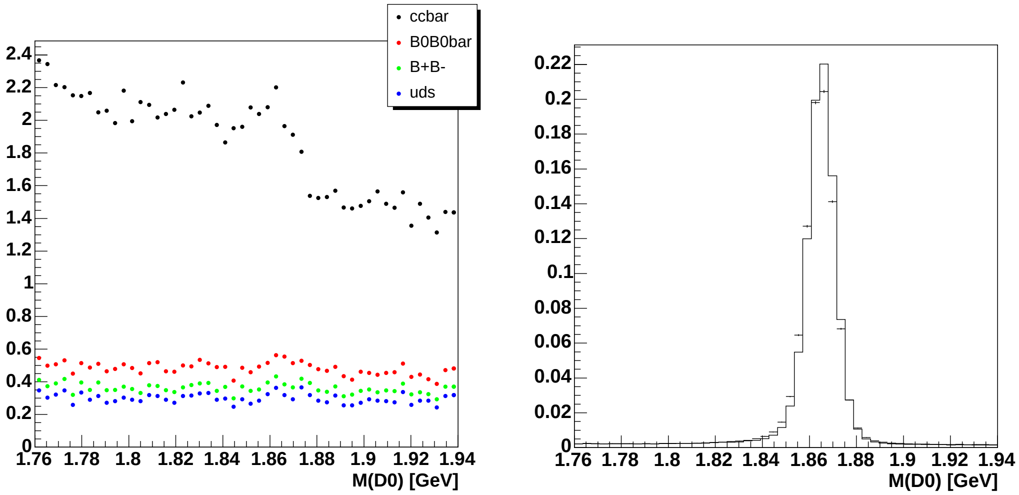

Figure 4.4: **Left:** M_{D^0} distributions of the different Monte Carlo components. The background component is small and there is no sign of any peaking background. **Right:** Comparison of data and MC, where good agreement is observed.

obtained with the M_{D^0} fit to the data sample. Moreover the M_{D^0} distributions of the background components do not present a peak in the selected region, so we parameterize the background distribution with a linear function.

4.3.1 Dalitz background parameterization

Since there is no indication of any peaking background in the M_{D^0} distribution, the M_{D^0} sidebands can be used to parameterize the background Dalitz distribution. Two sidebands are chosen: the "left" sideband centered at $M_{D^0} = 1.8\,\mathrm{GeV}/c^2$ and the "right" sideband centered at $M_{D^0} = 1.92\,\mathrm{GeV}/c^2$. The width of both of these regions is chosen to be $30\,\mathrm{MeV}/c^2$, the background component is parameterized with sum of two terms described below. The first is a resonant component parameterized as an incoherent sum of BW resonances, which is justified because the background is a sum of many different components that do not interfere and there is no dominant component. The resonances include: $K^{*-}(892)$, $K^{*+}(892)$, $\rho^0(770)$, and a spin-zero $K_S\pi^+$ component not corresponding to any real resonance, but introduced to improve the goodness of fit. The second term is a non-resonant component parameterized by a third-order polynomial in two dimensions. The relative fraction of the two background components is evaluated from the data.

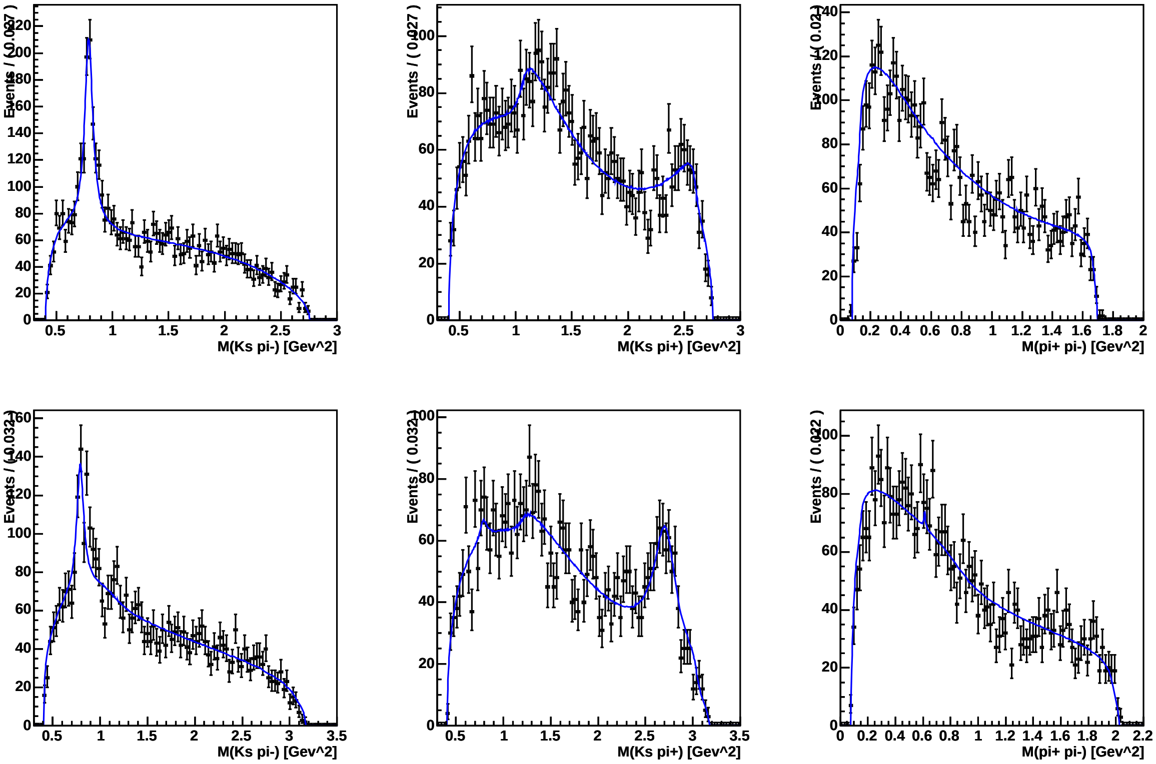

Figure 4.5: Dalitz background distribution extracted from left sideband (top) and right sideband (right). The blue line corrsponds to the fit result

Figure 4.5 shows the left and right sideband data samples and the fit results. The mass and the width of the $K^*(892)$ and $\rho^0(770)$ are taken from the PDG [20], while the mass and the width of the BW are extracted from the fit of the right sideband.

4.4 Efficiency and momentum resolution

4.4.1 Efficiency

The efficiency as a function of position in the Dalitz plot is evaluated using a signal Monte Carlo sample of 2.82M events where the D^0 is allowed to decay isotropically. The 334853 events remaining after all selection criteria are fit to a third-order polynomial in two dimensions:

$$\begin{aligned}\epsilon(x,y) = |1 + a_1 \cdot x + a_2 \cdot y + a_3 \cdot x^2 + a_4 \cdot x^2 + a_5 \cdot x \cdot y + \\ a_6 \cdot x^3 + a_7 \cdot y^3 + a_8 \cdot x \cdot y^2 + a_9 \cdot y \cdot x^2|,\end{aligned} \tag{4.3}$$

where $x = m_{12}^2$ and $y = m_{13}^2$. Figure 4.6 shows the Dalitz distribution of the MC sample. The efficiency over the Dalitz plot is basically uniform.

4.4.2 Mass resolution

The imperfect reconstruction of tracks from the D^0 leads to a modification of the Dalitz structure. The momentum smearing worsens the agreement between the $D^0 \to K_S^0\pi^+\pi^-$Dalitz plot distribution and the Dalitz model used to fit it, and causes about 2-3% of the reconstructed D^0 decays to lie outside the kinematically-allowed region. In

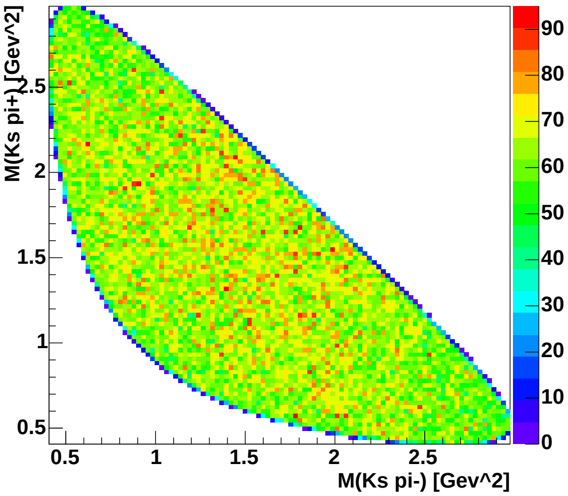

Figure 4.6: Efficiency distribution obtained from Monte Carlo distributions.

order to improve the momentum resolution of the D^0 daughters, a D^0 mass constraint fit is applied during the reconstruction. There are two advantages: 1) the uncertainty of the four-momentum of the particles is reduced, giving a more precise measurement of the mass squared variables used to define an event position in the Dalitz plot, and 2) the decay position in these variables is guaranteed to respect the kinematic boundaries of the Dalitz plot.

Resolution function

To evaluate the effect of the of the mass resolution on the shape of the Dalitz amplitude we calculate the event-by-event difference in the generated and reconstructed (m_{12}^2, m_{13}^2) distributions. The resolution as a function of the Dalitz variables has been obtained in bins of $(0.1\,\mathrm{GeV}/c^2 \times 0.1\,\mathrm{GeV}/c^2)$ by fitting the resolution function for

parameter	generated	smeared
$K^*(892)$ mass	8.9222e-01 ± 8.00e-05	8.9348e-01 ± 8.02e-05
$K^*(892)$ width	5.1208e-02 ± 1.86e-04	5.1232e-02 ± 1.86e-04
$\omega(782)$ mass	7.8246e-01 ± 1.48e-05	7.8053e-01 ± 1.36e-05
$\omega(782)$ width	8.8380e-03 ± 2.67e-05	8.8995e-03 ± 2.93e-05

Table 4.1: Fit results of the mass and the width of the generated and smeared $K^*(892)$ and $\omega(782)$ samples.

(m_{12}^2, m_{13}^2) with a sum of three Gaussian distributions.

In order to demostrate the effect of the resolution function on the $K^*(892)$ shape, a sample of 200000 events is generated and smeared according to resolution determined in MC. We then fitted both the generated and the smeared samples. The results of the fits are given in Table 4.1 and displayed in Fig. 4.7. A small effect on the mass and the width of the $K^*(892)$ is seen. We performed the same test with the $\omega(782)$ in order to test the effect of the resolution function on a narrow resonance (Fig. 4.7 right) The overall conclusion is that the finite mass resolution has a negligible effect on the analysis and will treat the momentum resolution as systematics.

4.5 Decay Amplitude

4.5.1 The Isobar model

The Dalitz plot distribution (m_{12}^2, m_{13}^2) is fitted using the Isobar model described in detail in Ref. [22]. In this formalism, the decay amplitude f can be written as a sum

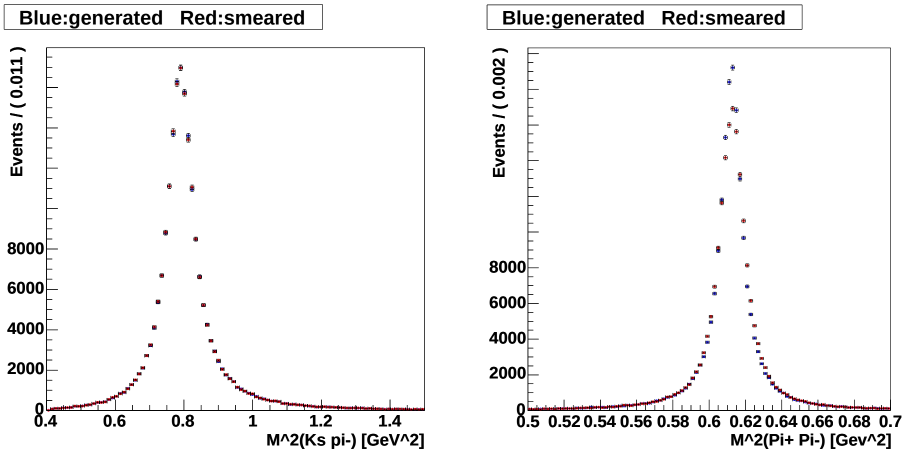

Figure 4.7: **Left:** BW distribution of the $K^*(892)$ sample, **Right:** BW distribution of the $\omega(782)$ sample. the smearing effect is not significant in both cases.

of two-body matrix elements and a non-resonant term according to

$$f = a_0 e^{i\phi_0} + \Sigma a_r e^{i\phi_r} \mathcal{A}_{\text{spin}}(ABC/r). \tag{4.4}$$

The first term is the three-body non-resonant term and the sum is over the contributions from the intermediate two-body resonances. The form factors $\mathcal{A}_{\text{spin}}(ABC/r)$ are described in detail in Sec. 3.5, which we do not repeat here. The Γ_{AB} is a function of the mass M_{AB}, the momentum p_{AB} of either daughter in the AB rest frame, the momentum p_r of either daughter in the resonance rest frame, the spin J of the resonance, and the width Γ_r of the resonance. The explicit expression for Γ_{AB} is [22]

$$\Gamma_{AB} = \Gamma_r \left(\frac{p_{AB}}{p_r}\right)^{2J+1} \left(\frac{M_r}{M_{AB}}\right) F_r^2. \tag{4.5}$$

For $\pi\pi$ vector resonances ($\rho(770)$ and $\rho(1450)$) we use the Gounaris-Sakurai (GS) parametrization [23] introduced in Sec. 3.4.

The form factors F_D and F_r attempt to model the underlying quark structure of the D^0 meson and the intermediate resonances. We use the Blatt-Weisskopf penetration factors shown in Table 3.1. The one free parameter R represents the "radius" of the meson and depends on the momentum p_r of the decay particles in the parent rest frame. We assume $F_D = 1$ for the D^0 and $R = 1.5\ \mathrm{GeV}^{-1}$ for the intermediate resonances.

4.5.2 The K-matrix Model

It is well-known that the isobar model is only suitable for relatively narrow and isolated resonances. The treatment of S-wave states in $D^0 \to K^0_S\pi^+\pi^-$requires a more general formalism to account for non-trivial dynamics due to the presence of broad, overlapping resonances. We therefore use the K-matrix approach to parameterize the S-wave component of the $\pi^+\pi^-$ system in $D^0 \to K^0_S\pi^+\pi^-$. The amplitude is given by

$$f = F_1 + \sum_{spin \neq 0} a_r e^{i\phi_r} \mathcal{A}_{spin}(ABC/r), \tag{4.6}$$

where F_1 is the contribution of the S-wave states (parameterized in the K-matrix formalism) and the sum is over the contributions from the intermediate non-scalar resonances. The factor F_1 is

$$F_l = \sum_j (I - iK\rho)^{-1}_{lj} P_j, \tag{4.7}$$

where I is the identity matrix, K is the matrix describing the S-wave scattering process, ρ is the phase-space matrix and P is the initial production vector [31]. The index l is the pion channel index where $1 = \pi\pi$, $2 = K\overline{K}$, $3 = 4\pi$, $4 = \eta\eta$, and $5 = \eta\eta'$. In this picture, the production process can be viewed as consisting of an initial preparation of several states, which are then propagated by the $(I - iK\rho)^{-1}_{lj}$ term into the final state (Fig. 3.7). Since we are describing the $\pi\pi$ channel, only the F_1 amplitude is present.

The masses and widths of the BW components are taken from the PDG [20]. The K-matrix parameters are obtained from the study of Anisovich and Sarantsev (AS) [39], who performed a global fit of the available $\pi\pi$ scattering data from threshold up to 1900 MeV/c^2. The AS K-matrix parameterization is

$$K_{ij}(s) = \left\{ \sum_\alpha \underbrace{\frac{g_i^{(\alpha)} g_j^{(\alpha)}}{m_\alpha^2 - s}}_{\text{pole}} + f_{ij}^{\text{scatt}} \underbrace{\frac{1.0 - s_0^{\text{scatt}}}{s - s_0^{\text{scatt}}}}_{\text{SVP}} \right\} \underbrace{\frac{(1 - s_{A0})}{(s - s_{A0})}(s - s_A m_\pi^2/2)}_{\text{Adler zero}}, \tag{4.8}$$

where the pole term $\frac{g_i^{(\alpha)} g_j^{(\alpha)}}{m_\alpha^2 - s}$ is responsible for the resonant contribution. The non-resonant term is described by a slowly-varying function of s, $\frac{1.0 - s_0^{\text{scatt}}}{s - s_0^{\text{scatt}}}$. The term

Table 4.2: K-matrix parameters. Masses and coupling constants are in GeV/c^2.

m_α	$g_{\pi\pi}$	$g_{K\overline{K}}$	$g_{4\pi}$	$g_{\eta\eta}$	$g_{\eta\eta'}$
0.65100	0.22889	-0.55377	0.00000	-0.39899	-0.34639
1.20360	0.94128	0.55095	0.00000	0.39065	0.31503
1.55817	0.36856	0.23888	0.55639	0.18340	0.18681
1.21000	0.33650	0.40907	0.85679	0.19906	-0.00984
1.82206	0.18171	-0.17558	-0.79658	-0.00355	0.22358
s_0^{scatt}	f_{11}^{scatt}	f_{12}^{scatt}	f_{13}^{scatt}	f_{14}^{scatt}	f_{15}^{scatt}
-3.92637	0.23399	0.15044	-0.20545	0.32825	0.35412
$s_{A0} = -0.15$	$s_A = 1$				

$\frac{(1-s_{A0})}{(s-s_{A0})}(s - s_A m_\pi^2/2)$, is the "Adler zero" term[1], to suppress the amplitude at $\pi\pi$ threshold in accordance with the Adler-Weinberg theorem [41]. The $g_i^{(\alpha)}$ is the coupling constant of the K-matrix pole m_α to the i^{th} channel. The parameter values used in this analysis are listed in Table 4.2 (obtained through private communication with Anisovich and Sarantsev).

By definition, K is real and symmetric. However, the K-matrix couplings and poles may not have a physical meaning. The K-matrix is related to the physical (and therefore, observable) T-matrix by the following expression:

$$T = (I - iK\rho)^{-1} \cdot K. \tag{4.9}$$

A one-to-one correspondence between K and T exists only in the simplest case of a single pole and a single channel. (Sec. 3.8). The phase space matrix is diagonal,

---

[1] Note that there is a typo in Ref. [40].

$\rho_{ab} = \delta_{ab}\rho_a$, and

$$\rho_i(s) = \sqrt{1 - \frac{(m_{1i} + m_{2i})^2}{s}}. \tag{4.10}$$

The normalization is such that $\rho_i \to 1$ as $s \to \infty$. Since the S-matrix has to respect analyticity, we used an analytic continuation for ρ_a below threshold. The expression for the multi-meson-state phase space is written as [39]

$$\rho_5(s) \quad = \left\{ \begin{array}{ll} \rho_{51} & s < 1\,\mathrm{GeV}/c^2 \\ \\ \rho_{52} & s > 1\,\mathrm{GeV}/c^2 \end{array} \right\}, \tag{4.11}$$

where

$$\rho_{51}(s) = \rho_0 \int\int \frac{ds_1}{\pi}\frac{ds_2}{\pi} \frac{M_\rho^2 \Gamma(s_1)\Gamma(s_2)\sqrt{(s + s_1 - s_2)^2 - 4ss_1}}{s[(M^2 - s1)^2 + M^2\Gamma^2(s_1)][(M^2 - s_2)^2 + M^2\Gamma^2(s_2)]} \tag{4.12}$$

and

$$\rho_{52}(s) = \left(\frac{s - 16m_\pi^2}{s}\right). \tag{4.13}$$

Here, s_1 and s_2 are the squared energies of the two pions, M is the ρ-meson mass and $\Gamma(s)$ is the energy-dependent width. The factor ρ_0 provides the continuity of $\rho_5(s)$ at $s = 1\,\mathrm{GeV}^2$. Energy conservation in the di-pion system must be satisfied when calculating the integral. This complicated expression reveals the fact that the ρ meson has an intrinsic width. If one sets $\Gamma(s) = \delta(s)$, where δ is the Dirac δ function,

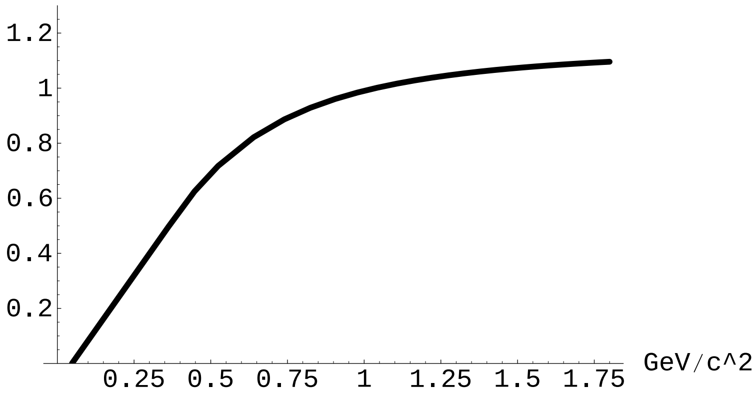

Figure 4.8: The $\pi\pi$ phase-space factor as shown in Eq. 4.10, Note that $\rho(s) \to 1$ as $s \to \infty$.

the usual two-body phase-space factor is obtained.

Figure 4.8 shows the real part of the $\pi\pi$ phase-space factor and Fig. 4.9 shows the 4π phase-space factor. Figure 4.10 shows the $\pi\pi$ S-wave intensity, where the absence of a simple Breit-Wigner-like structure is apparent. Figure 4.11 shows the Argand plot diagram for the $\pi\pi$ S-wave. One can see that K-matrix satisfies unitarity, which is a fundamental requirement of the S-matrix. In contrast, it is well known that unitarity is not respected generally in the BW model. Figure 4.12 shows the $\pi\pi$ scattering phase shift. There is a strong phase variation around $\sqrt{s} = 1\,\text{GeV}$ and $1.5\,\text{GeV}$, which corresponds to the narrow $f_0(980)$ and $f_0(1500)$ scalar resonances. Fig. 4.13 shows the elasticity plot for $\pi\pi$ scattering. The process is purely elastic up to $1\,\text{GeV}$, while new channels (*e.g.* $K\bar{K}$) open up at higher energies and the scattering process becomes inelastic.

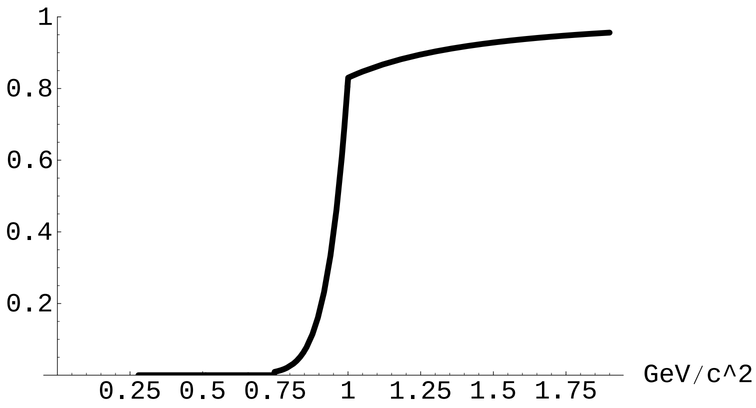

Figure 4.9: The 4π phase-space factor as shown in Eq. 4.11.

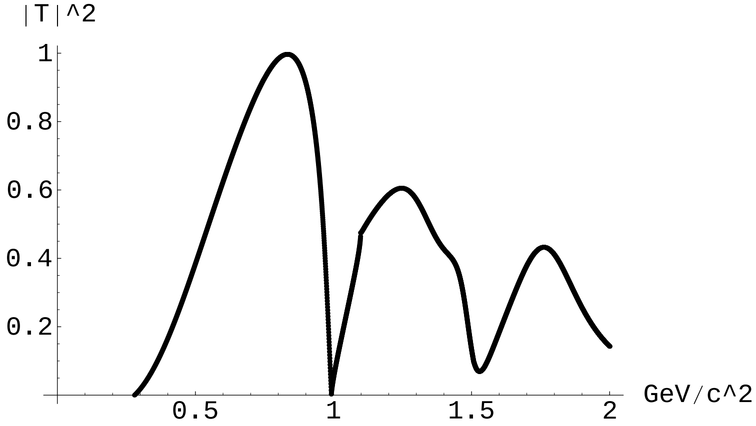

Figure 4.10: The $\pi\pi$ S-wave intensity, showing the lack of a simple Breit-Wigner resonance structure.

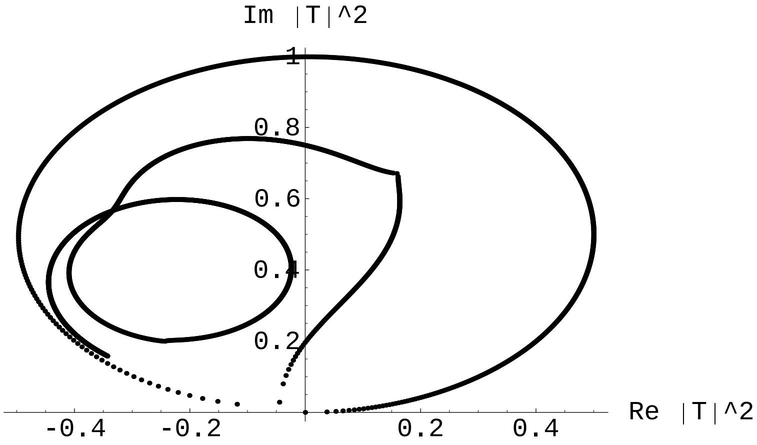

Figure 4.11: The Argand Plot Diagram for the $\pi\pi$ S-wave component, showing the unitarity of the K-matrix parameterization.

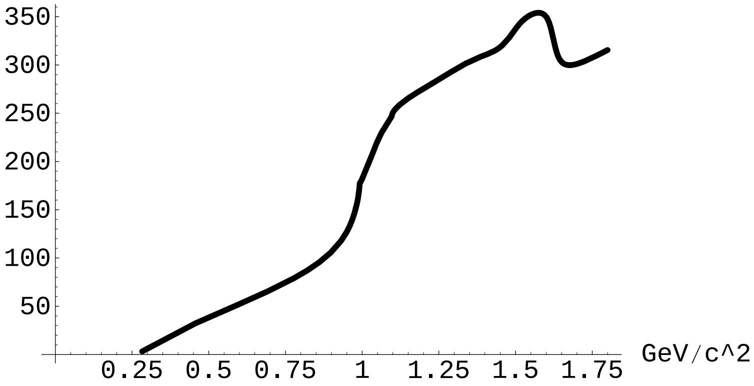

Figure 4.12: The $\pi\pi$ S-wave phase shift.

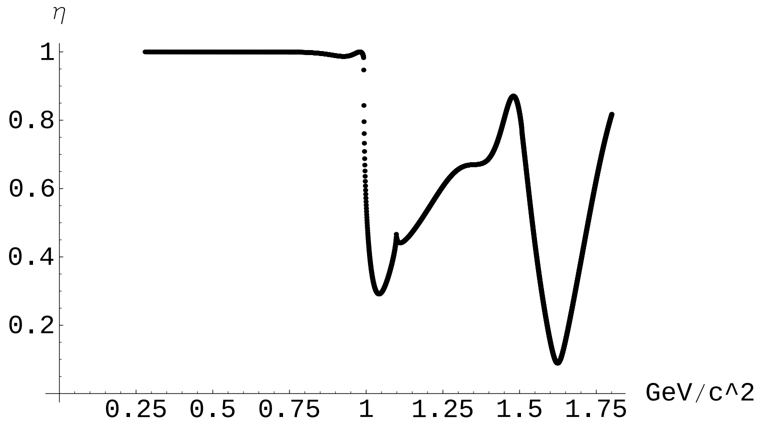

Figure 4.13: The elasticity plot, indicating the purely-elastic nature of the scattering process below 1 GeV.

4.6 Likelihood function and fit procedure

An unbinned maximum-likelihood technique is used to fit the population on the Dalitz plot and to extract the amplitudes (a_{nr}, a_j) and phases (ϕ_{nr}, ϕ_j). The likelihood function is

$$L = x\ P_{\rm sig} + (1-x)\ P_{\rm bkg},$$

where

$$P_{\rm sig}(m_{12}^2, m_{13}^2) = \frac{\epsilon(m_{12}^2, m_{13}^2)\,|f(m_{12}^2, m_{13}^2)|^2}{\int \epsilon(m_{12}^2, m_{13}^2)\,|f(m_{12}^2, m_{13}^2)|^2\,d\mathcal{DP}}.$$

Here x is the fraction of the signal events and $1-x$ is the fraction of background events. $f(m_{12}^2, m_{13}^2)$ is the signal Dalitz Probability Density Function (PDF) which is described in Sec. 4.5. The background dalitz distribution $P_{\rm bkg}(m_{12}^2, m_{13}^2)$ is described in Sec. 4.3, while the efficiency $\epsilon(m_{12}^2, m_{13}^2)$ is described in Sec. 4.4.1.

4.7 Results

4.7.1 Isobar Model

For fitting the Dalitz plot we have considered a model with twelve resonances described by the masses and widths listed in the PDG [20] (see Table 4.3). This leads to 18 two-body decay amplitudes and phases, eight of which are $\pi\pi = \sigma_1$, $\rho^0(770)$, $\omega(782)$, $f_0(980)$, σ_2, $f_2(1270)$, $f_0(1370)$, and $\rho(1450)$; five are $K^0_S\pi^- = K^*(892)$, $K^*_0(1430)$, $K^*_2(1430)$, $K^*(1410)$, and $K^*(1680)$); and three are $K^0_S\pi^+ = K^*(892)$, $K^*_0(1430)$, and $K^*_2(1430)$. All the considered resonances are well established except the two $\pi\pi$ scalar resonances σ_1 and σ_2, which were used in the first measurement of γ in this mode by the Belle experiment. [42]. The masses and widths of these two scalars were obtained from an initial binned likelihood fit[2] with all phases and amplitudes varied together with the masses and widths of the two resonances. The binning we use in this case consists of a uniform grid of 200 × 200 bins, which corresponds to about 3 MeV precision on the $\pi^+\pi^-$ invariant mass, well below the expected width of the two scalars. The values obtained in this way are later fixed to obtain all the phases and amplitudes using the full unbinned maximum likelihood fit. Since there is an arbitrary overall normalization factor and phase, we choose the $K^0_S\rho$ mode as our reference and set its amplitude and phase to unity and zero, respectively. Figure 4.14 show the projections of the fit results (corrected by efficiency) on top of the data

---

[2] We used binned likelihood technique since the standard fit with the additional parameters takes a prohibitive amount of time to converge.

Resonance	Mass (MeV/c^2)	Width (MeV/c^2)	Spin
$K^*(892)$	891.66	50.8	1
$K_0^*(1430)$	1412	294	0
$K_2^*(1430)$	1425.6	98.5	2
$K^*(1410)$	1414	232	1
$K^*(1680)$	1717	322	1
σ_1	484 ± 9 (from fit)	383 ± 14 (from fit)	0
$\rho^0(770)$	775.8	146.4	1
$\omega(782)$	782.6	8.5	1
$f_0(980)$	975	44	0
σ_2	1014 ± 7 (from fit)	88 ± 13 (from fit)	0
$f_2(1270)$	1275.4	185.1	2
$f_0(1370)$	1434	173	0
$\rho(1450)$	1406	455	1

Table 4.3: Values for the masses and widths of the resonances used in the $D^0 \to K_s\pi^-\pi^+$ Dalitz plot fit. The values and the width for the two scalars σ_1 and σ_2 have been obtained floating them in the fit, while the other have been fixed according to the PDG [20] values.

distributions.

4.7.2 The K-matrix Model

From Sec. 4.7.1 we see that in the BW model two ad-hoc σ scalars were needed to obtain a reasonable fit. This was one of the primary reasons for pursuing a K-matrix approach. Another difference is that the mass and the width of $K^*(1680)$, which is incorrectly averaged by the PDG as the LASS experiment observed $K^*(1680)$ in the $K^-p \to K^-\pi^+n$ and $K^-p \to \overline{K}^0\pi^+\pi^-n$ channels, but with quite different masses and widths. Since we are considering only the $K^*(1680) \to K\pi$ channel, the mass and width from $K^-p \to K^-\pi^+n$ measurement rather than PDG average value should be

Resonance	Amplitude	phase (degrees)	fit fraction (%)
$K^*(892)$	1.777 ± 0.018	131.0 ± 0.81	58.51
$\rho^0(770)$	1 (fixed)	0(fixed)	22.33
$K^*(892)$ DCS	0.1789 ± 0.0080	-44.0 ± 2.4	0.59
$\omega(782)$	0.0391 ± 0.0016	114.8 ± 2.5	0.56
$f_0(980)$	0.469 ± 0.011	213.4 ± 2.2	5.81
$f_0(1370)$	2.32 ± 0.31	114.1 ± 4.4	3.39
$f_2(1270)$	0.915 ± 0.041	-22.0 ± 2.9	2.95
$K_0^*(1430)$	2.454 ± 0.074	-7.9 ± 2.0	8.37
$K_0^*(1430)$ DCS	0.350 ± 0.069	$-344. \pm 10.$	0.60
$K_2^*(1430)$	1.045 ± 0.045	-53.1 ± 2.6	2.70
$K_2^*(1430)$ DCS	0.074 ± 0.038	-98 ± 30	0.01
$K^*(1410)$	0.524 ± 0.073	-157 ± 10	0.39
$K^*(1680)$	0.99 ± 0.31	-144 ± 18	0.35
$\rho(1450)$	0.554 ± 0.097	$35 \pm 12.$	0.28
σ_1	1.346 ± 0.044	-177.5 ± 2.5	9.11
σ_2	0.292 ± 0.025	-206.8 ± 4.3	0.98
Non resonant	3.41 ± 0.48	-233.9 ± 5.0	6.82

Table 4.4: Amplitudes, phases and fit fraction of the different components obtained from the likelihood fit of the $D^0 \to K_S^0\pi^+\pi^-$Dalitz plot. The total fit fraction is 1.24.

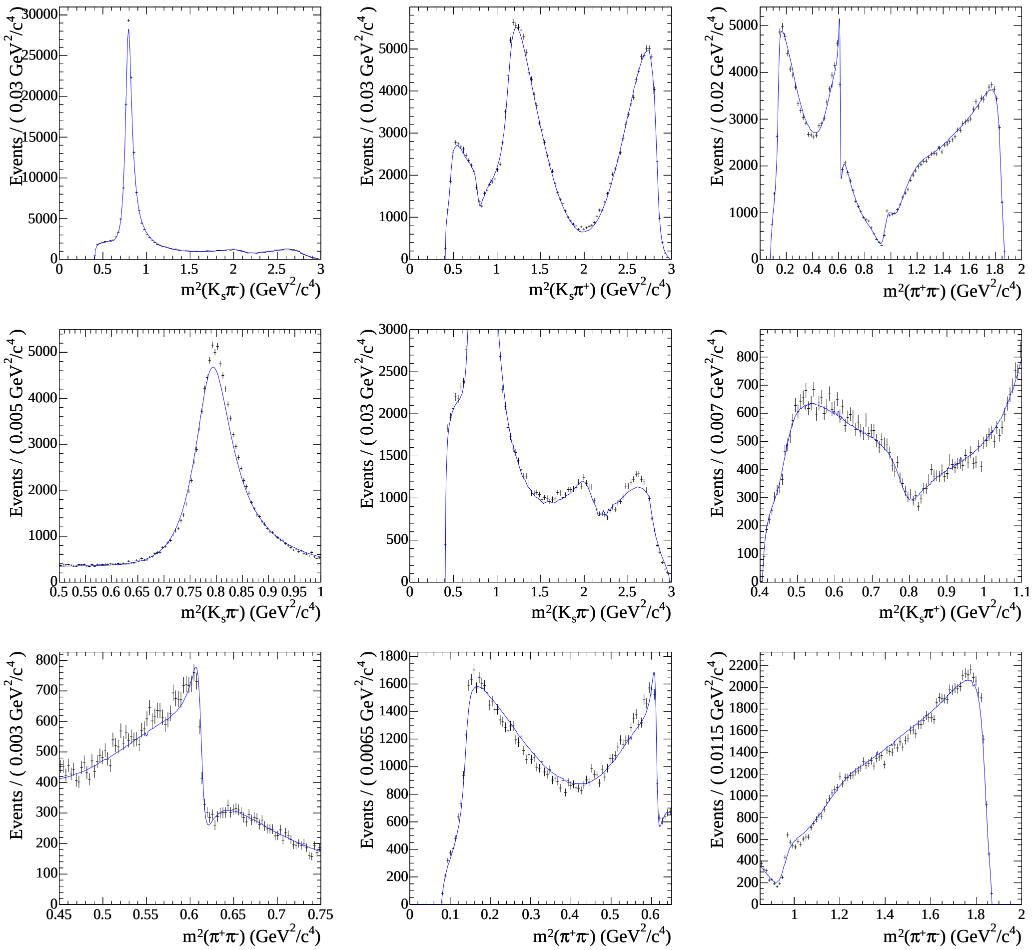

Figure 4.14: Result of the unbinned likelihood fit to the $D^0 \rightarrow K_S^0\pi^+\pi^-$Dalitz plot. On the first row the three projections are displayed : Cabibbo allowed (CA) ($K_s\pi^-$), the ($K_s\pi^+$) and the ($\pi^+\pi^-$) (from left to right respectively). On the second row we show the zoom of K*(892) mass peak region (on the left) and of the K*(1430) and K*(1680) (on the middle) on the Cabibbo allowed ($K_s\pi^-$) projection . On the right of the middle row we show the region of interference between the CA-DCS decays involving K*(892) mesons. On the bottom row we show, in the ($\pi^+\pi^-$) projection, the $\rho - \omega$ mixing interference region (left plot) and the ρ region (left plot), the low mass ($\pi^+\pi^-$) (middle plot) and the higher mass ($\pi^+\pi^-$) projection with $f_0(980)$.(right)

Resonance	Mass (MeV/c^2)	Width (MeV/c^2)	Spin
$K^*(892)$	891.66	50.8	1
$K_0^*(1430)$	1412	294	0
$K_2^*(1430)$	1425.6	98.5	2
$K^*(1680)$	1677	205	1
$\rho^0(770)$	775.8	146.4	1
$\omega(782)$	782.6	8.5	1
$f_2(1270)$	1275.4	185.1	2
$\rho(1450)$	1406	455	1

Table 4.5: Values for the masses and widths of the resonances used for the fit in the K-matrix model. Except $K^*(1680)$, all values are obtained from the PDG. [20]

used. Table 4.5 lists the masses and widths of the resonances used by the K-matrix fit.

In the K-matrix formalism the Dalitz amplitude f is written as a sum of a two-body-decay matrix elements for the spin-1 and spin-2 resonances (isobar model), and the spin-zero piece is written in terms of the K-matrix, which we denote as F_1. Therefore,

$$f = F_1 + \sum_{spin \neq 0} a_r e^{i\phi_r} \mathcal{A}_{spin}(ABC/r), \tag{4.14}$$

where F_1 is the contribution of $\pi\pi$ S-wave states,

$$F_1 = \sum_j (I - iK\rho)^{-1}_{1j} P_j, \tag{4.15}$$

Resonance	Amplitude	phase (degrees)	fit fraction (%)
$K^*(892)$	1.7582 ± 0.0079	129.78 ± 0.38	59.01
$\rho^0(770)$	1 (fixed)	0(fixed)	22.30
$K^*(892)$ DCS	0.1708 ± 0.0042	-50.23 ± 1.3	0.58
$\omega(782)$	0.04238 ± 0.00089	837.5 ± 1.2	0.64
$K_0^*(1430)$	2.745 ± 0.036	-375.245 ± 0.71	9.82
$K_0^*(1430)$ DCS	0.380 ± 0.029	-26.73 ± 4.6	0.19
$K_2^*(1430)$	1.124 ± 0.020	-42.01 ± 1.3	3.00
$K_2^*(1430)$ DCS	0.200 ± 0.018	-64.25 ± 5.3	0.09
$K^*(1680)$	1.634 ± 0.089	159.0 ± 2.7	1.17
β_1	3.784 ± 0.067	-931.268 ± 0.81	N/A
β_2	9.830 ± 0.081	17.7 ± 1.1	N/A
β_4	13.45 ± 0.16	-6.77 ± 1.3	N/A
f_1^{prod}	10.93 ± 0.10	-153.379 ± 0.88	N/A
sum of S-wave			16.2

Table 4.6: Amplitudes, phases and the fit fraction of the different components obtained from the likelihood fit of the $D^0 \to K_S^0 \pi^+ \pi^-$Dalitz plot. The total fit fraction is 1.16.

and P_j is the production vector,

$$P_j(s) = \left\{ \sum_\alpha \frac{\beta_\alpha g_j^{(\alpha)}}{m_\alpha^2 - s} + f_{1j}^{\text{proj}} \frac{1.0 - s_0^{\text{scatt}}}{s - s_0^{\text{scatt}}} \right\}. \tag{4.16}$$

The free parameters for the P-vector are β_α and f_{1j}^{proj}. Figure 4.15 shows projections of the fit results (corrected by efficiency) and the data distributions.

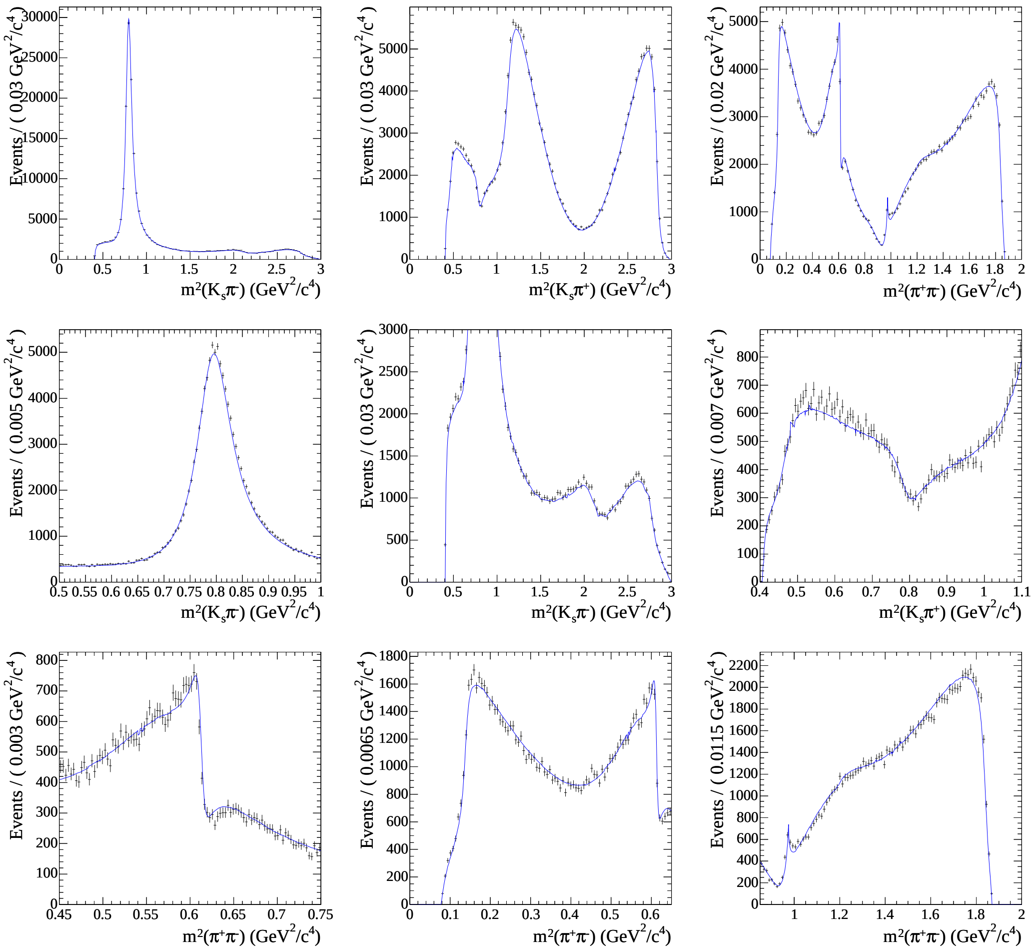

Figure 4.15: Result of the K-matrix fit to the $D^0 \rightarrow K_S^0\pi^+\pi^-$Dalitz plot. On the first row the three projections are displayed : Cabibbo allowed (CA) ($K_s\pi^-$), the ($K_s\pi^+$) and the ($\pi^+\pi^-$) (from left to right respectively). On the second row we show the zoom of K*(892) mass peak region (on the left) and of the K*(1430) and K*(1680) (on the middle) on the Cabibbo allowed ($K_s\pi^-$) projection . On the right of the middle row we show the region of interference between the CA-DCS decays involving K*(892) mesons. On the bottom row we show, in the ($\pi^+\pi^-$) projection, the $\rho - \omega$ mixing interference region (left plot) and the ρ region (left plot), the low mass ($\pi^+\pi^-$) (middle plot) and the higher mass ($\pi^+\pi^-$) projection with $f_0(980)$.(right)

Chapter 5

Analysis of $B^- \to D^{(*)}K^-$ decays

5.1 Introduction

In this chapter the detailed analysis of $B^- \to D^{(*)}K^-$ is presented. A charged B^- can decay into a $D^0(\overline{D}^0)K^-$ final state via a $V_{cb}(V_{ub})$ mediated process. *CP* violation can occur if the $D^0(\overline{D}^0)$ decay to the same final state. The measurement of *CP* violation in this mode is sensitive to the phase difference between $|V_{ub}|e^{-i\gamma}$ and $|V_{cb}|$, and thus to the angle γ of the Unitarity Triangle. In order to increase the statistics, the B mesons are reconstructed in two decay modes: $B^- \to D^0K^-$ and $B^- \to D^{*0}K^-$. The event selection, background suppression and background composition are presented in this chapter; Dalitz plot efficiency and background parameterization are evaluated; and the signal and background yields are extracted.

5.2 $B^- \to D^{(*)0}K^-$ Selection

The $D^{(*)0}$ and K^- reconstruction

We used the same D^0 selection as in the Dalitz analysis in Chapter 4.2. The D^* is reconstructed in the $D^0\pi^0$ and $D^0\gamma$ modes. The photon candidates for $D^{*0} \to D^0\gamma$ are reconstructed from clusters in the electromagnetic calorimeter, and are required to have an energy greater than 30 MeV and to have a shower shape consistent with the expected distribution for photons. The π^0 candidates are reconstructed from pairs of photons with $115 < m(\gamma\gamma) < 150\,\mathrm{MeV}/c^2$ and total energy greater than 70 MeV. The photon momenta are refit to the invariant mass to the world average value for the π^0 mass [20]. To reduce the combinatorial background we require the mass difference Δm between the reconstructed D^{*0} and D^0 candidates to be within 2.5 MeV for the $D^{*0} \to D^0\pi^0(\gamma)$ and 10 MeV for the $D^{*0} \to D^0\pi^0(\gamma)$ respectively. The bachelor kaon is identified using standard *BABAR* particle identification(PID) algorithms that rely on energy-loss measurements in the SVT and DCH, and the Cherenkov measurement from the DIRC.

The B candidate selection

The charged B mesons are reconstructed from $D^{(*)0}$ and K^-. The candidate B^- decay point is obtained by vertexing the D^0 with the bachelor kaon. The probability of the vertex-fit $\chi 2$ must be greater than 0.001. The main variables used in the B meson selection are the beam energy-subsituted mass (m_{ES}) and the energy difference

(ΔE). The beam energy-subsituted mass is defined as:

$$\mathrm{m_{ES}} = \sqrt{(\sqrt{s}/2)^2 - p_B^{*2}}. \tag{5.1}$$

where p^* is the B candidate momentum in the $\Upsilon(4S)$ (CM) rest frame. Since $|p_B^*| \ll \sqrt{s}/2$, the experimental resolution on m_{ES} is dominated by beam energy fluctuations. Therefore, the shapes of the m_{ES} distribution for B meson is Gaussian, while the backgound is approximately flat with an endpoint near 5.29 GeV. The energy differnece is defined as:

$$\Delta E = E_B^* - \sqrt{s}/2 \tag{5.2}$$

where E_B^* is the energy of the B candidate in the $\Upsilon(4S)$ rest frame and $\sqrt{s}$ is the total energy of the $e^+ e^-$ system in the CM rest frame. Signal events are Gaussian distributed in ΔE around zero, while the background will have a downward sloping linear distribution in the region of interest. Table 5.1 summarizes the selection requirements and the number of selected events for signal and background in the range $m_{\mathrm{ES}} > 5.272$ is shown. The overall efficiency for signal events is ($18.0 \pm 0.1\%$).

5.2.1 Comparison of data and Monte Carlo

Figure 5.1 shows the m_{ES} distribution(left) and the ΔE distribution(right) after applying the final selection criteria. For all the cases the colored histograms display

selection cuts	signal	B_d^0	B^+	$D\pi$	$D^0 \to 4\pi$	D^{*0}	uds	charm
$\|cos\theta_{\rm thr.}\|$ <0.8 $\|M(D^0) - M(PDG)\|$ <20MeV $\|M(K_S) - M(PDG)\|$ <10MeV $\|\Delta E\| <$ 60 MeV $P(\chi^2, D^0)$ >0. $P(\chi^2, B)$ >0. tight K-id.	210.3	26.7	78.5	42.9	9.4	1.3	138.1	195.7
$\|M(D^0) - <M>\|$ <12MeV	193.2	13.9	49.9	40.5	9.0	1.3	83.2	131.7
$\|M(K_S) - <M>\|$ <9MeV	191.8	13.6	47.2	39.4	8.2	1.3	78.6	122.1
cos$\alpha_{\rm K_S} > 0.99$	184.8	6.0	18.6	39.6	0.8	1.3	42.0	83.1
$\|\Delta E\| <$ 30 MeV	175.1	3.4	9.0	6.3	0.8	0.3	23.6	44.1
range $m_{\rm ES}$ [5.20-5.29]	176.0	20.9	37.0	6.4	0.8	0.5	199.9	351.7
same cuts but loose K-id	200.3	6.5	12.9	35.0	0.8	1.1	34.3	56.6
range $m_{\rm ES}$ [5.20-5.29]	201.3	32.1	50.3	35.0	0.8	1.5	267.7	447.1
same cuts but very-tight K-id	160.3	2.3	6.7	3.5	0.6	0.0	20.6	41.9
range $m_{\rm ES}$ [5.20-5.29]	161.0	16.7	31.9	3.5	0.6	0.2	176.9	322.8

Table 5.1: Number of selected events for signal and backgrounds in the range $m_{\rm ES}$ >5.272 reported from Monte Carlo sample. The number of events is based on the estimation from 108 million $B\overline{B}$ events.

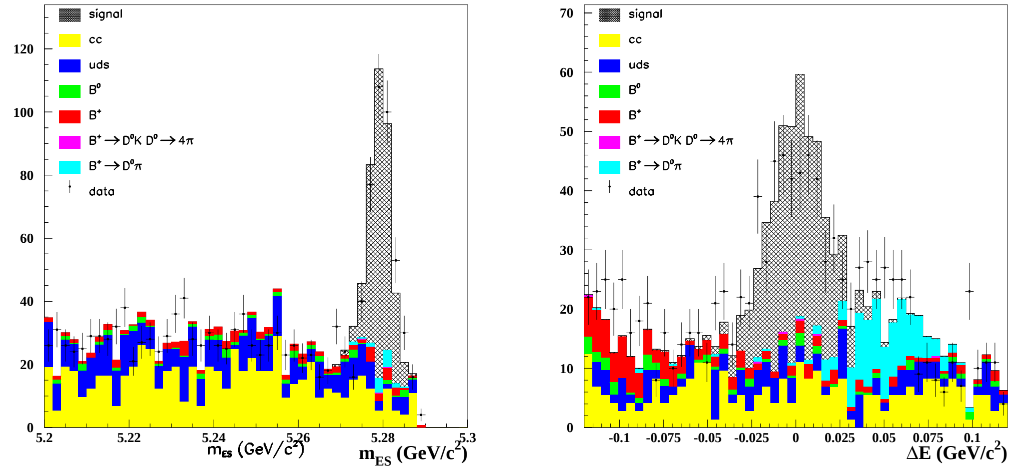

Figure 5.1: **Left:** The $m_{\rm ES}$ distribution for various components obtained after applying the final selection criteria. The Monte Carlo samples are all shown together with the data represented by points with error bars. **Right:** The Data/Monte Carlo comparison for the ΔE variable. The distributions are obtained after having applied all the cuts and for all the events entering in the Likelihood.

the various Monte Carlo components and the data are represented by crosses. The simulation sample reproduces expected yield and we find good agreement between the data and Monte Carlo.

5.3 Background composition

It is important to understand and suppress the background and extract the yield for all background components. In a brief summary, there are several backgrounds that require attention in this analysis:

- jet-like continuum $e^+e^- \to q\bar{q}$(q=u,d,s,c) background;

- background from $B \to D\pi$;
- $\Upsilon(4S) \to B^0\overline{B}^0, B^+B^-$ not containing a signal decay("general B-background");
- real and fake D^0 from $e^+e^- \to c\bar{c}$;
- wrongly-tagged D^0 and $\bar{D}^0$ in $e^+e^- \to c\bar{c}$.

In the following section the individual backgrounds are discussed in detail, including the background-suppression technique and the yield determination.

5.3.1 Background from $e^+e^- \to q\bar{q}$ continuum light-quark

The dominant background in this analysis is from light-quark production in e^+e^- annihilation. To suppress this background, the unique event topologies of $B\overline{B}$ vs. $q\bar{q}$ events is exploited.

- $\cos\theta^*_B$:the polar angle of B in the $\Upsilon(4S)$ center of mass system;
- the Legendre monomials (L_0 and L_2);
- $\cos\theta_{\mathrm{thrust}}$: the angle between the rest of event thrust axis and the B direction,

where the thrust axis of an event is defined as the direction which maximizes the sum of the longitudinal momenta of the particles. In a typical background event(jet-like event), the decay products of each B candidate lie in one of the two jets, and thus they are approximately back-to-back, while for a true signal event, the B decay axis is uncorrelated with the thrust axis of the rest of the events, which has event topology

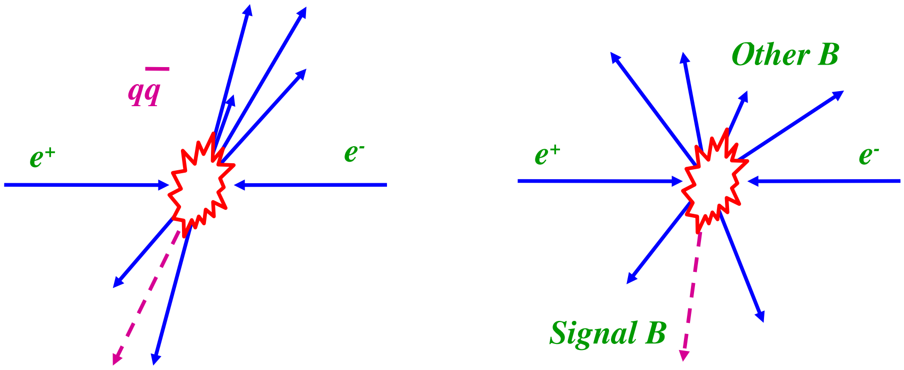

Figure 5.2: Pictorical representation of the jet-like topology of $q\bar{q}$ events (left), in comparison to the spherical shape of $B\overline{B}$ events (right).

of spherical shape. Therefore, the event shapes provides an excellent way to separate from signal to background. Figure 5.2 shows a pictorial representation of the event shape in $q\bar{q}$ and $B\overline{B}$ events.

Simulation studies indicate that a requirement of $|\cos\theta_{\text{thrust}}|$ <0.8 is sufficient to reduce this background without significantly affecting the signal efficiency.

udsc background yield extraction

The yields are determined from the m_{ES} distribution (Fig. 5.1), where the signal peaks at 5.28 GeV/c^2 and the background varies slowly with an endpoint given by the beam energy in the CM frame. (5.29 GeV) To extract the signal and background yields, the m_{ES} distribution is fitted with an empirical background function suggested by the ARGUS collaboration [43], and a Gaussian distribution for the signal component.

Mode	Data	MC
DK	67.2 ± 4.9%	64.3 ± 4.9 %
$D^*K(\pi^0)$	92.0 ± 4.0%	91.0 ± 5.0 %
$D^*K(\gamma)$	47.0 ± 10.0%	62.0 ± 8.0 %

Table 5.2: Fraction of signal events satsifying $m_{\text{ES}} > 5.272\,\text{MeV}/c^2$

The ARGUS function is defined as:

$$\frac{dN}{dm_{\text{ES}}} = N \cdot m_{\text{ES}} \cdot \sqrt{1 - x^2} \cdot e^{-\zeta(1-x^2)}, \tag{5.3}$$

where $x = m_{\text{ES}}/m_{\text{max}}$, m_{max} is the endpoint of the ARGUS distribution, and ζ is determined from the fit. Table 5.2 shows the fraction of signal events satisfying $m_{\text{ES}} > 5.272\,\text{GeV}/c^2$. It turns out that the $D^*K(\pi^0)$ has the highest purity due to the constraint from π^0 and the Δm cut.

5.3.2 Background from $B \to D\pi$ decays

The $B^- \to D\pi^-$ and $B^- \to DK^-$ are very similar kinematically, with several consequences. First, true $B^- \to D\pi^-$ events reconstructed as $B^- \to DK^-$ tend to peak at the same m_{ES} value as signal. Second, the D^0 is correctly reconstructed, so the Dalitz distribution for these events is identical to signal. Therefore, this background will dilute the accuracy of the γ measurement. Despite the excellent PID cabalility of the *BABAR* detector, the $B^- \to D\pi^-$ background is irreducible because the branching fraction $\mathcal{B}(B^- \to D\pi^-) = 5.3 \pm 0.5 \times 10^{-3}$ is an order of magnitude larger than the corresponding $\mathcal{B}(B^- \to DK^-) = 3.7 \pm 0.6 \times 10^{-4}$.

We estimate this fraction from data by fitting the ΔE distribution(Fig. 5.3), where the $B^- \to D\pi^-$ events are shifted by approximately $+50\,\mathrm{MeV}$ with respect to the $B^- \to DK^-$ events. [1]

For this fit, signal are parameterized by a Gaussian distribution centered at zero with a width $\sigma_{\mathrm{DK}} = (14.6 \pm 0.2)\,\mathrm{MeV}$. For the $D\pi$ events, the parametrization exploits the fact that the shift in ΔE between the kaon and pion hypothesis is known on a event by event basis,

$$\Delta E_{\mathrm{shift}} \;=\; \Delta E_K - \Delta E_\pi = \gamma\left[\sqrt{m_K^2 + p^2} - \sqrt{m_\pi^2 + p^2}\right], \tag{5.4}$$

where p is the momentum of the bachelor track in laboratory frame and γ is the PEP-II boost factor. The important adventage of this parameterization is that the mean of the $D\pi$ distribution is not an independent variable. The results of the fit are shown in Fig. 5.3, where we found

$$f(D\pi) = 0.059 \pm 0.012. \tag{5.5}$$

5.3.3 Background from $B \to 4\pi$

Another possible source of peaking background is $B \to 4\pi$, as the dominant particles produced in e^+e^- annihilations are pions that can be readily combined into fake B

---

[1] Only the region between [-0.100,0.120] GeV/c^2 has been considered in the fit to exclude the contribution from the D^*K events.

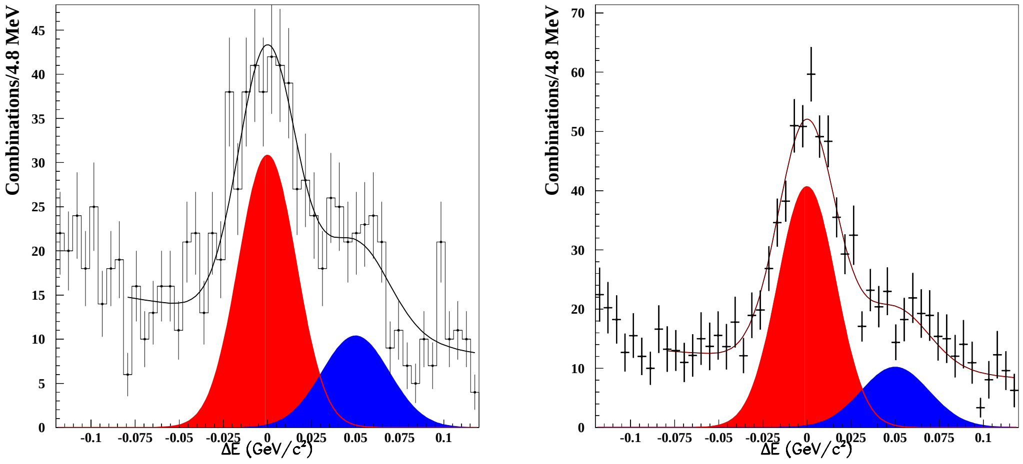

Figure 5.3: The plots on left (right) show the ΔE distribution as obtained on the data (Monte Carlo) with the fit superimposed. The two Gaussian distributions for the DK (in center) and the $D\pi$ events(on the right) are shown.

candidates. However, this background is easily suppressed by requiring $\cos(\alpha_{K_S}) > 0.99$, which the efficiency of this cut is 99%.

5.3.4 Real D^0 from $e^+e^- \to c\bar{c}$

There is an extra complication in the $c\bar{c}$ background. In uds background the fraction of real D^0 is vanishingly small, and the Dalitz distribution does not display the same structure as in a real D^0 decay. The situation is different in $c\bar{c}$ where there is a mix of real and fake D^0, where their Dalitz plot distribution is very different. For this reason the background from the $c\bar{c}$ and the background from the $b\bar{b}$ events must be considered separately, whether the D^0 is real or not. The total fraction of the real D^0 in the combinatorial background is obtained on the data by checking the fraction

Mode	MC-counting
DK	22.1 ± 4.2 %
$D^{*}K(\pi^0)$	36.0 ± 13.0%
$D^{*}K(\gamma)$	39.0 ± 6.0%

Table 5.3: Fraction of real D^0 candidate in $c\bar{c}$ background in the $m_{ES} > 5.272$ range.

of signal events in m_{D^0}, which results in

$$f_{\text{real}}^{D^0} = 0.221 \pm 0.042 \quad . \tag{5.6}$$

Table 5.3 summarize the fraction of real D^0 in other channels.

Charge correlation with kaons

Another delicate issue is the fraction of events with a real D^0 associated with a negative charged kaon in $e^+e^- \to c\bar{c}$ process: Due to the large mass of the D^0-K combination required to fake a $B^- \to D^0K^-$ decay, the D^0 and kaon are typically obtained from opposite jets in $e^+e^- \to c\bar{c}$ events. Since the quark in the jet opposite the D^0 is likely to be a $\bar{c}$, the resulting kaon is perferentially a K^+, which is the wrong sign combination with the D^0. The fraction of right-sign combinations is obtained from simulation and the results are shown in Table 5.4, where we find that approximately 20% of kaons are tagged correctly.

Mode	MC-counting
$DK(R_{cc})$	20.8 ± 3.3 %
$D^*K(\pi^0)$	23.0 ± 11.0%
$D^*K(\gamma)$	16.0 ± 6.0%

Table 5.4: Fraction of right sign D^0 candidate in udsc in the $m_{\rm ES}$ >5.272 range.

5.3.5 Random flavor-tagging kaon for signal events

Finally, another potential background arises when the correct D^0 candidate in a signal decay is incorrectly combined with a random kaon in the event. Half the time these kaons will have the wrong sign and be misinterpreted as a $\bar{D}^0$. However, detailed MC simulation indicates that this background is negligible.

5.4 $B^- \to D^0\pi^-$ as control sample

A very similar analysis can be performed to select on the data the $B \to D\pi$ channel. The kinematics of the decay is very similar to the $B^- \to D^0K^-$ and therefore it is possible to extract the relevant observables for the selection of the signal events and the *CP* fit.

All the selection criteria are identical to those applied for the DK analysis except that the events are selected in the ΔE region in the range [20 - 80] MeV (see Fig. 5.4). We also required the bachlor's tracks satsify the pion selection from *BABAR* PID requirements.

The $m_{\rm ES}$ distribution for the different components and for the data are shown in Fig. 5.4. The efficiency obtained on $D\pi$ signal Monte Carlo is estimated to be

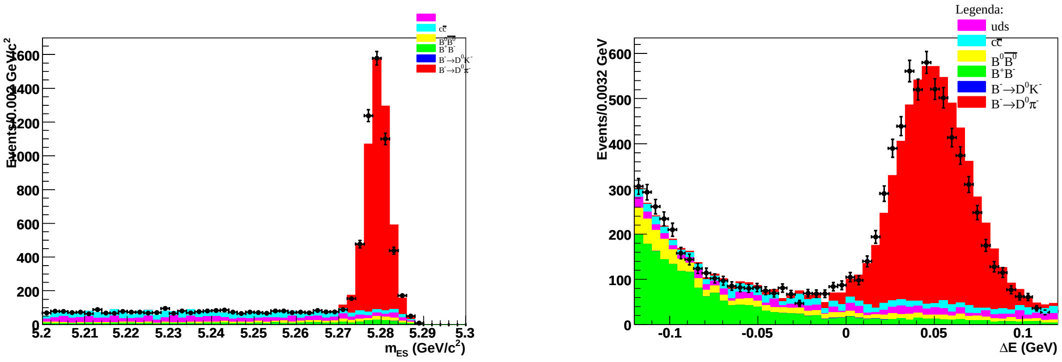

(a) (b)

Figure 5.4: (a) m_{ES} and (b) ΔE distributions for $B^- \to D^0\pi^-$, $D^0 \to K^0_S\pi^+\pi^-$. All the cuts are applied but the one on the plotted variable. The different background components are reported in colored filled histograms, the data are over-imposed with full dots. The number of events is normalized to 288.5 fb^{-1}.

$\epsilon = (13.8 \pm 0.1)\%$.

The overall background fraction is smaller than in the DK sample. Nevertheless the $B\overline{B}$ background shows more complicated peaking structure coming from many different components with respect to DK. Considering that r_B for this sample is expected to be 0.007, it will be difficult to use this sample to extract γ. [2] Therefore, this sample is used for the control samples.

5.5 Efficiency over the Dalitz plot

In Sec. 4.4.1 the efficiency as a function of position in the Dalitz plot was discussed. Similiarly, the efficiency of the signal events in $B^- \to D^0K^-$must be consider seper-

---

[2] the r_B in $B^- \to D^{(*)0}\pi^-$ can be roughly estimated as $\frac{1}{3}\frac{|V^*_{ub}V_{cd}|}{|V^*_{cb}V_{ud}|}\sim 0.007$, where the factor of $\frac{1}{3}$ accounts for color suppression.

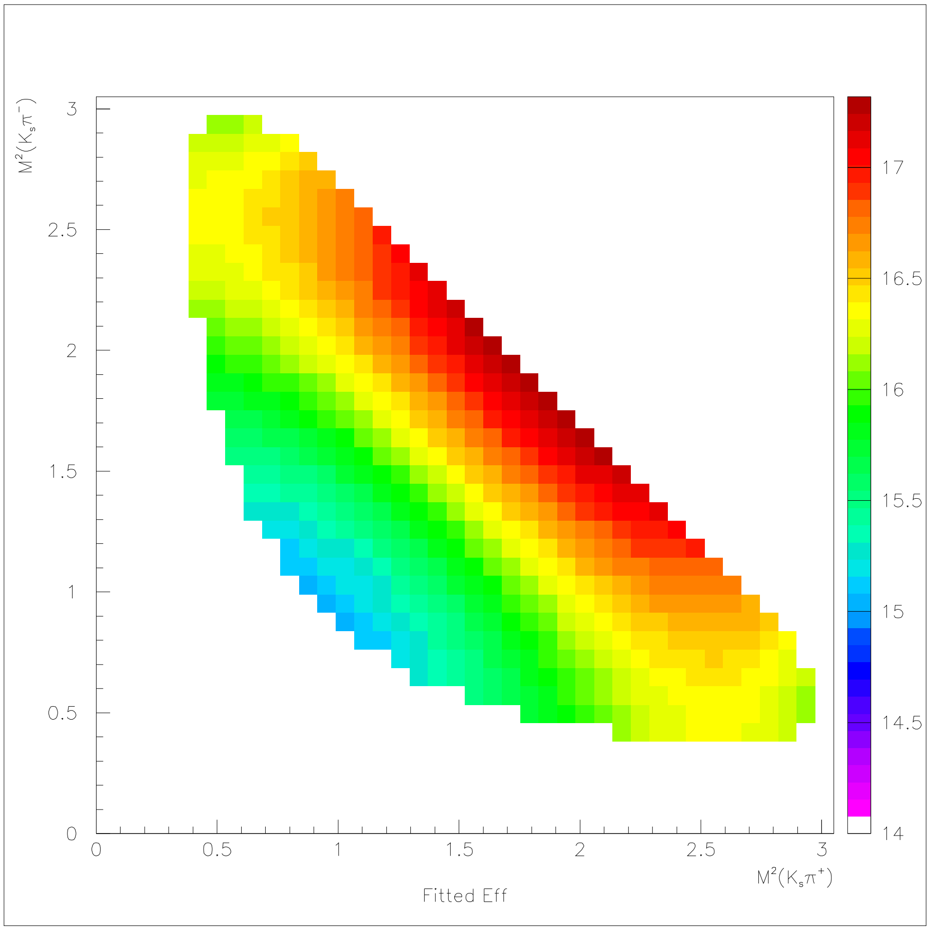

Figure 5.5: Fitted efficiency over the Dalitz plot $(K_s\pi^+)$ *vs* $(K_s\pi^-)$. The color code indicates the value (in percent) of the fitted efficiency. This is taken from high statistics $B^- \to D^0 K^-$ signal Monte Carlo.

Parameters	a_1	a_2	a_3
	1.093 ± 0.162	-0.217 ± 0.049	0.013 ± 0.007

Table 5.5: The values and the errors for the parameters of the third-order polynomial function as shown in Eq. 5.7.

ately. It was evaluated using a signal Monte Carlo sample distributed uniformly over the Dalitz plot. The efficiency is fitted with a third-order polynomial taking into account the symmetry of the Dalitz plot:

$$\epsilon(x, y) = 1 + a_1\ (x + y) + a_2\ (x^2 + y^2 + xy) + a_3\ (x^3 + y^3 + x^2y + xy^2). \tag{5.7}$$

Table 5.5 shows the corresponding fit result.

5.6 Background Dalitz shape

The Dalitz plot shape for continuum $q\bar{q}$ background is determined from off-resonance data using the D^0 mass sidebands in order to exclude the real D^0 (where $M_{D^0} < 1.85$ GeV or $M_{D^0} > 1.88\,\mathrm{GeV}$). For generic $B\bar{B}$ background events, the Dalitz plot shape is determined using Monte Carlo where real D^0 is excluded. The selection criteria are identical to those used for the D^0K analysis except the ΔE requirement, which is relaxed in order to increase the sample size. The distributions for $q\bar{q}$ and $B\overline{B}$ have been fitted to a third-order polynomial function, since studies have shown a clear asymmetry in the Dalitz shape for D^0 and $\overline{D}^0$,

$$\begin{aligned} \mathrm{bkg}(x,y) &= 1 + a_{10}\ x + a_{01}\ y + a_{20}\ x^2 + a_{11}\ xy + a_{02}\ y^2 + \\ & a_{30}\ x^3 + a_{21}\ x^2y + a_{12}\ xy^2 + a_{03}\ xy^3\ , \end{aligned} \tag{5.8}$$

where $x \equiv m^2(K_s\pi^+)$ and $y \equiv m^2(K_s\pi^-)$.

5.7 Likelihood fit procedure

In this section the likelihood definition and strategy used to extract the *CP* parameters is described. We first describe the generic (prototype) PDF for a given B and D decay mode. This PDF is then replicated for all the different B and D decay modes in order to make a combined fit.

Prototype likelihood definition

The likelihood function is built from the total probability density function(PDF), which is constructed to distinguish the following signal and background components.

- $B^- \to D^0K^-$signal (sig);
- $B \to D\pi$ background;
- $udsc$ background;
- $B\bar{B}$ background.

However, as explained Sec. 5.3, there are several components in the $c\bar{c}$ and $B\bar{B}$ background. They are subdivided into two categories:

- real D^0 ($\bar{D}$) combined with a flavor tagged kaons.
- combinatorics (fake D^0).

The total PDF $\mathcal{P}^\alpha$ is defined as:

$$\begin{aligned}
\mathcal{P}^\alpha &= f_{\rm sig}\mathcal{P}^\alpha_{\rm sig} + f_{D\pi}\mathcal{P}^\alpha_{D\pi} + f_{\rm sigWS}\mathcal{P}^{\overline{\alpha}}_{\rm sigWS} + \\
& f_{\rm cont}\left\{(1-R_{\rm cont})\mathcal{P}^{\rm comb}_{\rm cont} + R_{\rm cont}\left[R^{RS}_{\rm cont}\mathcal{P}^\alpha_{\rm cont} + (1-R^{RS}_{\rm cont})\mathcal{P}^{\overline{\alpha}}_{\rm cont}\right]\right\} + \\
& f_{\mathsf{B\overline{B}}}\left\{(1-R_{\mathsf{B\overline{B}}})\mathcal{P}^{\mathsf{comb}}_{\mathsf{B\overline{B}}} + R_{\mathsf{B\overline{B}}}\left[R^{RS}_{\mathsf{B\overline{B}}}\mathcal{P}^\alpha_{\mathsf{B\overline{B}}} + (1-R^{RS}_{\mathsf{B\overline{B}}})\mathcal{P}^{\overline{\alpha}}_{\mathsf{B\overline{B}}}\right]\right\}, \qquad (5.9)
\end{aligned}$$

where

- $\alpha = \mathsf{D^0}$, or $\mathsf{\overline{D}^0}$ and $\overline{\alpha}$ is the charge conjugate state of α;
- f_j is the fraction of component $j = \mathrm{sig}, \mathrm{cont}, \mathrm{D}\pi, \mathrm{sigWS}, \mathsf{B\overline{B}}$;
- $R_{\rm cont}$ ($R_{\mathsf{B\overline{B}}}$) is the fraction of real D^0 or $\overline{D}^0$ in the cont ($\mathsf{B\overline{B}}$) background component;
- $R^{\mathsf{RS}}_{\rm cont}$ ($R^{\mathsf{RS}}_{\mathsf{B\overline{B}}}$) is the fraction of right sign D^0 or $\overline{D}^0$ in the cont ($\mathsf{B\overline{B}}$) background component;
- $\mathcal{P}^\alpha_j$ is the PDF for component j for the real D^0;
- $\mathcal{P}^{\mathsf{comb}}_j$ is the PDF for component j for the fake D^0.

In the general PDF definition of Eq. 5.9 we intentionally omitted explicit dependencies on variables, which are discussed in the following sections.

5.7.1 Signal yield determination

Component yields and PDF shape parameters were first determined by performing a simultaneous fit using $m_{\rm ES}$, ΔE, $\mathcal{F}$ as the discriminating variables. The PDF is

$$\mathcal{P}_j^\alpha \equiv \mathcal{P}_j^\alpha(m_{\rm ES}, \Delta E, \mathcal{F}) = \mathcal{P}_j^\alpha(m_{\rm ES})\mathcal{P}_j^\alpha(\Delta E)\mathcal{P}_j^\alpha(\mathcal{F}) \tag{5.10}$$

and the variables are assumed to be independent. The statistical uncertainty of the yields is correctly determined by performing an unbinned extended likelihood fit

$$\mathcal{L}_{\rm ext} = \frac{e^{-\eta}\eta^N}{N!}\prod_\alpha\prod_{i=1}^{N}\mathcal{P}^\alpha(i), \tag{5.11}$$

where N is the total number of events in the sample, and η is the expected value according to Poisson statistics. The yields N_j can be calculated simply as $N_j = \eta f_j$, the fractions satsifying $\sum_j f_j = 1$. The fit is done in ΔE region $[-80, 120]$ MeV for kaon samples and $[20, 80]$ MeV for pion samples. The background parameter for the $B\overline{B}$ background component is fixed to Monte Carlo estimates obtained separately for kaon and pion samples in the ΔE regions $[-30, 30]$ and $[20, 80]$ MeV, respectively. Due to the small number of events, the estimates for $(D^0\pi^0)K$ and $(D^0\gamma)K$ are made combining both samples. The $m_{\rm ES}$ $B\overline{B}$ peaking background contribution is negligible for all DK samples but is significant for $D\pi$ (both $D^0\pi$ and $D^{*0}\pi$). This has been estimated to be about 30% relative to the $B\overline{B}$ combinatorial component. This value is fixed in the fit and the relative fraction of peaking with respect to combinatorial background was determined from data directly. The fit projections for kaon and pion data for $m_{\rm ES}$, ΔE and $\mathcal{F}$ are shown in Fig 5.6 and 5.7, respectively. The corresponding yields are given in Table 5.6.

Decay modes	Signal	$B\overline{B}$	Continuum	$D\pi$
$B^- \to D^0K^-$,$D^0 \to K^0_S\pi^+\pi^-$	393 ± 25	583 ± 121	4989 ± 139	138 ± 17
$B^- \to D^{*0}K^-$,$D^0\pi^0$,$D^0 \to K^0_S\pi^+\pi^-$	101 ± 13	125 ± 29	446 ± 32	33 ± 8
$B^- \to D^{*0}K^-$,$D^0\gamma$,$D^0 \to K^0_S\pi^+\pi^-$	87 ± 12	345 ± 49	1275 ± 57	19 ± 8

Table 5.6: $B^- \to D^{(*)0}K^-$ yields, corresponding to 316.3 fb^{-1}.

Decay modes	Signal	$B\overline{B}$	Continuum	DK
$B^- \to D^0\pi^-$,$D^0 \to K^0_S\pi^+\pi^-$	5549 ± 83	3469 ± 202	8089 ± 215	60 ± 31
$B^- \to D^{*0}\pi^-$,$D^0\pi^0$,$D^0 \to K^0_S\pi^+\pi^-$	1526 ± 44	978 ± 55	609 ± 45	32 ± 21
$B^- \to D^{*0}\pi^-$,$D^0\gamma$,$D^0 \to K^0_S\pi^+\pi^-$	991 ± 41	2608 ± 99	2247 ± 93	32 ± 23

Table 5.7: $B^- \to D^{(*)0}\pi^-$ yields, corresponding to 316.3 fb^{-1}.

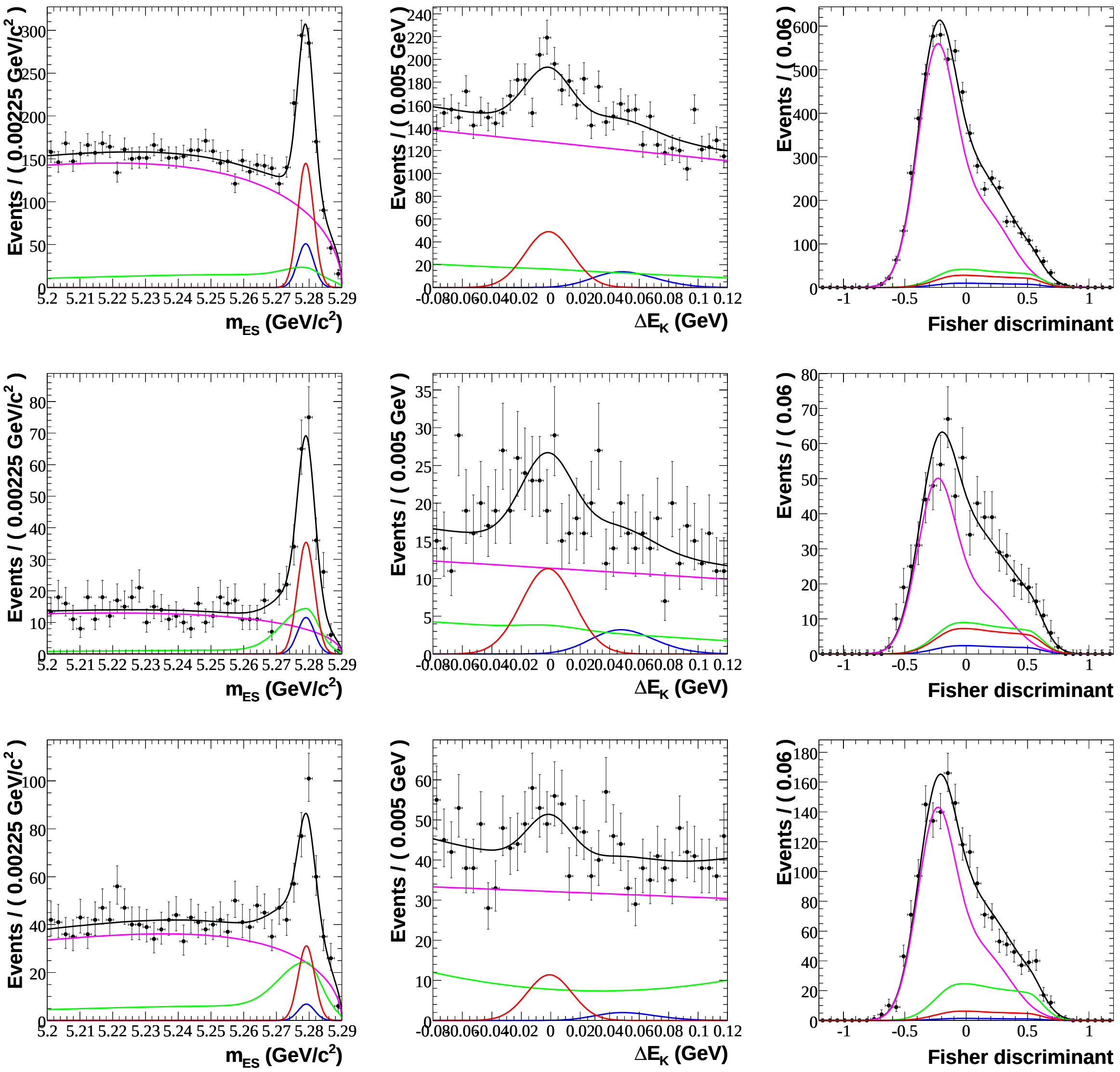

Figure 5.6: Distribution of $m_{\rm ES}$, ΔE and $\mathcal{F}$ for $B^- \to D^0 K^-$ (top), $B^- \to D^{*0} K^-$, $D^{*0} \to D^0 \pi^0$ (middle) and $B^- \to D^{*0} K^-$, $D^{*0} \to D^0 \gamma$ (bottom), for $D^0 \to K^0_S \pi^+ \pi^-$. The data are overlaid on the projection of the shapes fit described in the text. Also shown are the different components: signal (red), $D\pi$ (blue), $\mathsf{B}\overline{\mathsf{B}}$(green) and cont (magenta).

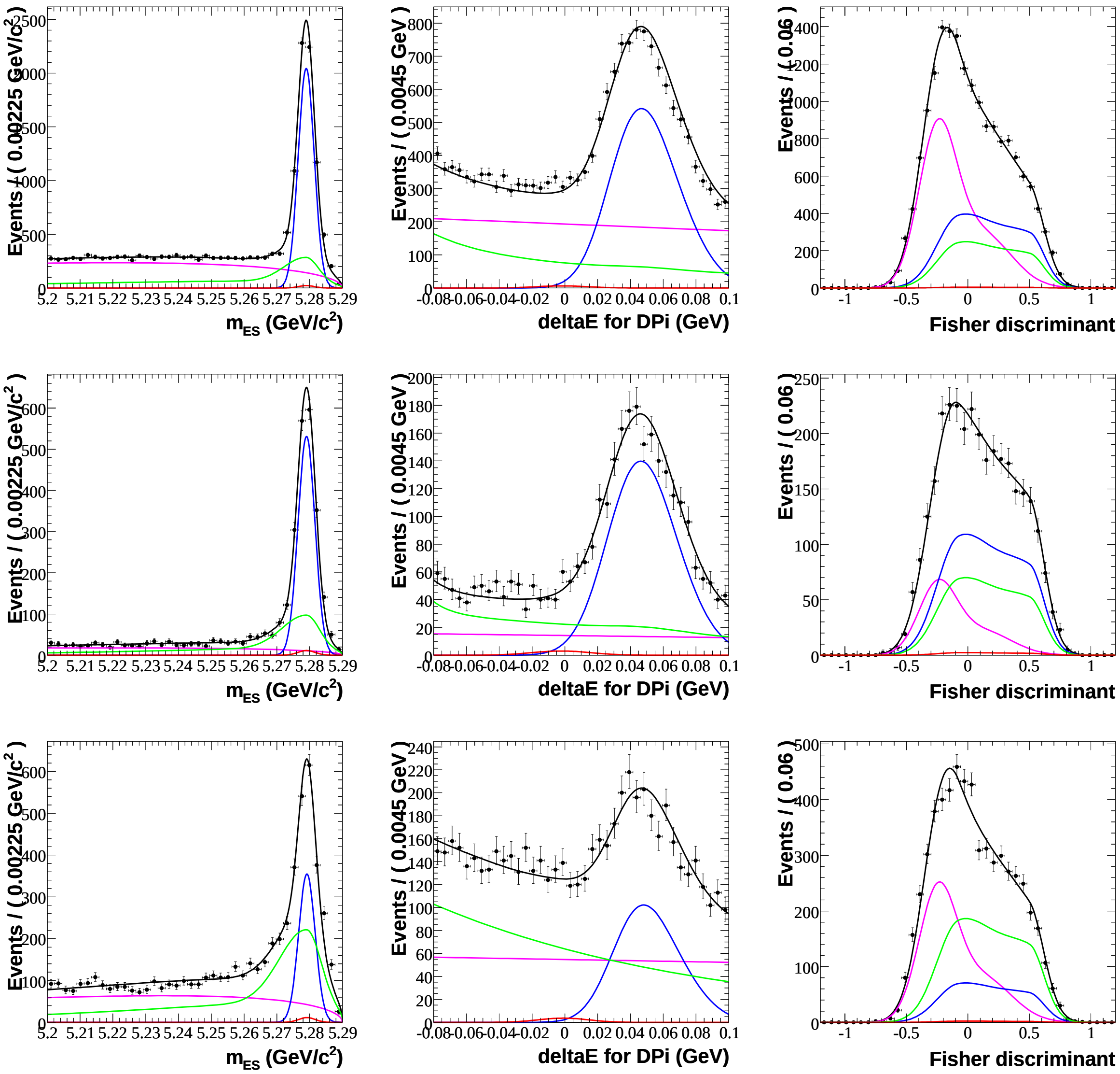

Figure 5.7: Distribution of $m_{\rm ES}$, ΔE and $\mathcal{F}$ for $B^- \to D^0\pi^-$ (top), $B^- \to D^{*0}\pi^-$, $D^{*0} \to D^0\pi^0$ (middle) and $B^- \to D^{*0}\pi^-$, $D^{*0} \to D^0\gamma$ (bottom), for $D^0 \to K^0_S\pi^+\pi^-$. The data are overlaid on the projection of the shapes fit described in the text. Also shown are the different components: signal (blue), DK (red), $\mathsf{B}\overline{\mathsf{B}}$(green) and cont (magenta).

Chapter 6

Measurement of γ in $B^- \to D^{(*)}K^-$ decays

6.1 Introduction

In the final chapter of this thesis the procedure to extract the CKM angle γ is presented. The Dalitz PDF is first presented, and then the modification necessary for $B^- \to D^{*0}K^-$and $B^- \to D^0K^{*-}$decay channels is explained. The sensitivity of analysis to γ is then discussed, and finally, the results and corresponding systematics are summarized.

6.2 The Dalitz PDF

A maximum likelihood fit technique is used to extract γ. As described in the Sec. 1.2.3, the PDF describing $B^- \to D^0 K^-$ pdf is defined as:

$$\mathcal{P}(m_\pm^2, m_\mp^2) = |f(m_\pm^2, m_\mp^2) + r_B e^{i(\delta_B \pm \gamma)} f(m_\mp^2, m_\pm^2)|^2, \tag{6.1}$$

where $m_\pm^2$ is the squared invariant mass of the $K_s\pi^\pm$, $f(m_\pm^2, m_\mp^2)$ is the $D^0 \to K_S^0\pi^+\pi^-$ Dalitz amplitude discussed in Sec. 4.5, and r_B and δ_B are the amplitude ratio and relative strong phase between $B^- \to \bar{D}^0 K^-$ and $B^- \to D^0 K^-$, respectively. In principle the observables γ, δ_B and r_B can be extracted using Eq. 6.1. However, there are several additional experimental complications:

- choices between cartesian or polar coordinates;
- modification of the PDF for D^*K decay;
- modification of the PDF for DK^* decay.[1]

Each point will be discussed here in detail.

6.2.1 Cartesian vs. polar coordinates

In Eq. 6.1, the *CP* parameters are written in terms of polar coordinates. Since r_B is by definition positive definite, it turns out the *CP* parameters are subjected to large

---

[1] The details can be found in appendix A.3

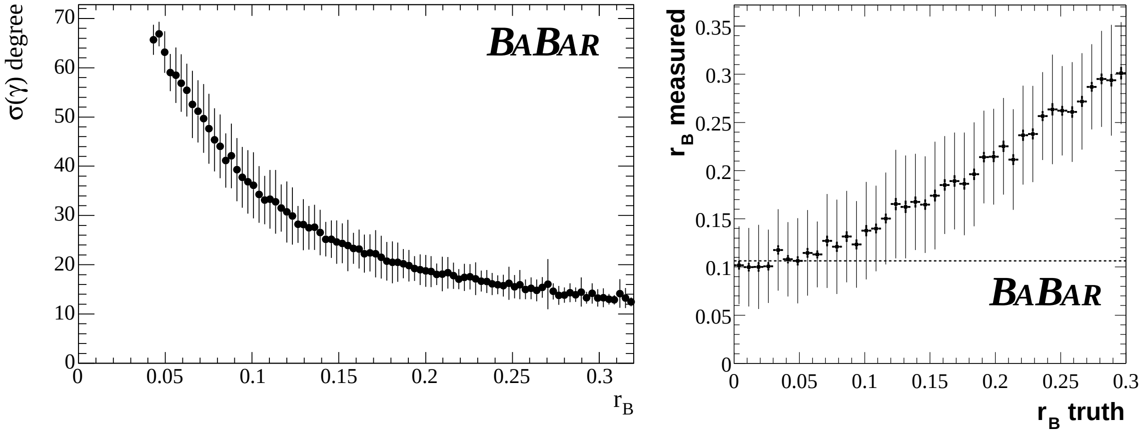

Figure 6.1: **Left:** Error on γ as a function of r_B. **Right:** r_B value obtained in the likelihood fit versus generated r_B. When the true r_B is small, the fit returns a biased estimate of r_B. The dashed line shows the theoretical estimate of r_B, which is roughly 0.1.

non-gaussian effects, where the fit returns a biased estimate of r_B. In addition, the errors on γ and δ_B strongly depen on the measured value of r_B. Figure 6.1 illustrates this effect, as well as the saturation effect on the measured value of r_B as a function of the true value. The origin of this effect is easily seen by considering the limiting case when $r_B \rightarrow 0$:(see Eq. 6.1) the terms involving γ are gone. Therefore, the error on γ increases with decreasing r_B.

This problem is solved by introducing the cartesian coordinates

$$x_{\pm} \equiv Re(r_{B\pm}e^{i(\delta\pm\gamma)}) \quad = \quad r_{B\pm}\cos(\delta \pm \gamma), \tag{6.2}$$

$$y_{\pm} \equiv Im(r_{B\pm}e^{i(\delta\pm\gamma)}) \quad = \quad r_{B\pm}\sin(\delta \pm \gamma). \tag{6.3}$$

The introduction of cartesian coordinate has several benefits. First, this particular basis has no physical boundaries, so the non-gaussian effect will not emerge. Second, cartesian coordinates are largely uncorrelated, while (r_B, δ, γ) are highly correlated. Third, it is much easier to combine results from different experiments in cartesian coordinates. Finally, direct *CP* violation has a simple geometric interpretation in cartesian coordinates, where the distance d between the measured (x, y) coordinates for B^+ and B^- is directly related to the weak phase γ:

$$d = \sqrt{(x_+ - x_-)^2 + (y_+ - y_-)^2} = 2r_B|\sin\gamma|. \tag{6.4}$$

The condition $d \neq 0$ indicates direct *CP* violation. In terms of cartesian coordinates, the PDF can be written as:

$$\begin{aligned}\mathcal{P}(m_\pm^2, m_\mp^2) \quad &= |f(m_\pm^2, m_\mp^2) + (x_\pm + iy_\pm)f(m_\mp^2, m_\pm^2)|^2 \qquad (6.5)\\ &= |f(m_\pm^2, m_\mp^2)|^2 + r_B^2|f(m_\mp^2, m_\pm^2)|^2 + \\ &2x_\pm Re[f(m_\pm^2, m_\mp^2)f^*(m_\pm^2, m_\pm^2)] + 2y_\pm Im[f(m_\pm^2, m_\mp^2)f^*(m_\pm^2, m_\pm^2)].\end{aligned}$$

6.2.2 Modification of PDF for D^*K events

As noted in Ref. [44], the PDF requires modification in the $B^- \to D^{*0}K^-$decay mode. because the strong phase δ_B^* depends on the D^* decay mode. Considering the neutral

D^* meson produced in B^- decay, denoted by $\tilde{D}^*$, we have:

$$\tilde{D}^* = D^{*0} + r_B^* e^{i(\delta_B^* - \gamma)} \bar{D}^{*0}. \tag{6.6}$$

Defining CP eigenstates of the neutral D^* system with the phase convention [2] $CP(D^{*0}) = \bar{D}^{*0}$, $CP(\bar{D}^{*0}) = D^{*0}$ leads to the following:

$$D_+^* = \frac{D^{*0} + \bar{D}^{*0}}{\sqrt{2}}, \qquad D_-^* = \frac{D^{*0} - \bar{D}^{*0}}{\sqrt{2}}, \tag{6.7}$$

and thus

$$D^{*0} = \frac{D_+^* + D_-^*}{\sqrt{2}}, \qquad \bar{D}^{*0} = \frac{D_+^* - D_-^*}{\sqrt{2}}, \tag{6.8}$$

Thus Eq. 6.6 can be written as

$$\tilde{D}^* = \frac{D_+^* + D_-^*}{\sqrt{2}} + r_B^* e^{i(\delta_B^* - \gamma)} \frac{D_+^* - D_-^*}{\sqrt{2}}. \tag{6.9}$$

We now consider D^* decays to the CP eigenstates $D\pi^0$ and $D\gamma$. The CP eigenvalue for the $D^* \to D\pi^0$ decay is, $\eta_{D^*} = \eta_D \times \eta_{\pi^0} \times (-1)^l$, where conservation of angular momentum requires $l = 1$. For the decay $D^* \to D\gamma$ we have $\eta_{D^*} = \eta_D \times \eta_\gamma \times (-1)^l$, and conservation of parity requires $l = 1$. Thus $\eta_{D^*} = -1 \times \eta_D$, and $D_\pm^* \to D_\mp\gamma$.

Next we consider the neutral D meson produced in the decay $B^- \to \tilde{D}^* K^-$, where

---

[2] The choice of CP phase convention does not affect observable quantities.

$\tilde{D}^* \to \tilde{D}\pi^0$,

$$\begin{aligned} \tilde{D} &= \frac{D_+ + D_-}{\sqrt{2}} + \frac{D_+ - D_-}{\sqrt{2}} \quad (6.10) \\ &= D^0 + r_B^* e^{i(\delta_B^* - \gamma)} \bar{D}^0, \quad (6.11) \end{aligned}$$

while the neutral D produced in the decay $\tilde{D}^* \to \tilde{D}\gamma$ is given by

$$\begin{aligned} \tilde{D} &= \frac{D_- + D_+}{\sqrt{2}} + r_B^* e^{i(\delta_B^* - \gamma)} \frac{D_- - D_+}{\sqrt{2}} \quad (6.12) \\ &= D^0 - r_B^* e^{i(\delta_B^* - \gamma)} \bar{D}^0 \quad (6.13) \\ &= D^0 + r_B^* e^{i(\delta_B^* + \pi - \gamma)} \bar{D}^0. \quad (6.14) \end{aligned}$$

Hence there is an effective strong phase shift of π between the two cases.

6.3 Sensitivity to γ accross the Dalitz plot

The sensitivity to γ over the Dalitz plot can be calculated by computing the 2^{nd} derivative of log-likelihood with respect to γ. Mathematically, one would write

$$\sigma^2(\gamma) = \frac{1}{\frac{d^2 \log(\mathrm{L})}{d^2\gamma}}, \qquad \text{sensitivity} \propto \frac{d^2 \log(\mathrm{L})}{d^2\gamma} \quad (6.15)$$

To evaluate the sensitivity, a large ensemble of pseudo experiments of Monte Carlo signal events is generated and the second derivative with respect to γ is evaluated

CP parameter	$B^- \to D^0\pi^-$	$B^- \to D^{*0}\pi^-$
x_-	-0.01142 ± 0.01458	0.01496 ± 0.02222
y_-	-0.01288 ± 0.01692	0.01777 ± 0.02791
x_+	0.02240 ± 0.01432	-0.02649 ± 0.02261
y_+	-0.01268 ± 0.01691	0.02646 ± 0.02374

Table 6.1: Fit results using data sample for the cartesian coordinates, for the $B^- \to D^0\pi^-$and $B^- \to D^{*0}\pi^-$ decay modes.

on an event-by-event basis. The result is shown in Fig. 6.2, where each event is weighted by the value of the second derivative of the log-likelihood with respect to γ. From Fig. 6.2 one can see that the highest sensitivity is coming from $K^*(892)$ doubly-cabibbo-suppressed(DCS) decays, $K^*(1430)$ DCS decay, and the $\rho(770)$ decay. However, both $K^*(892)$ DCS and $K^*(1430)$ DCS are highly suppressed, (see Sec. 4.7). Consequently, $B^- \to \rho(770)K^-$ gives the highest sensitivity to γ overall.

6.4 Fits to control samples

The fit procedure is tested on two large control samples: $D^{*-} \to D^0\pi^-$ from $c\bar{c}$ continuum events and $B^- \to D^{(*)0}\pi^-$. The $D^{*-} \to D^0\pi^-$ sample mimics a $B^- \to D^0K^-$ sample with r_B= 0. The $B^- \to D^0\pi^-$ sample is similar to $B^- \to D^0K^-$, but the corresponding value of r_B is expected to be approximately[3] 0.007. Table 6.1 shows the fit results, which are consistent with the expectations from fits to Monte Carlo samples.

---

[3] The value of r_B in $B^- \to D^{(*)0}\pi^-$ can be roughly estimated as $\frac{1}{3}\frac{|V_{ub}^*V_{cd}|}{|V_{cb}^*V_{ud}|}\sim$ 0.007 where $\frac{1}{3}$ accounts for color suppression.

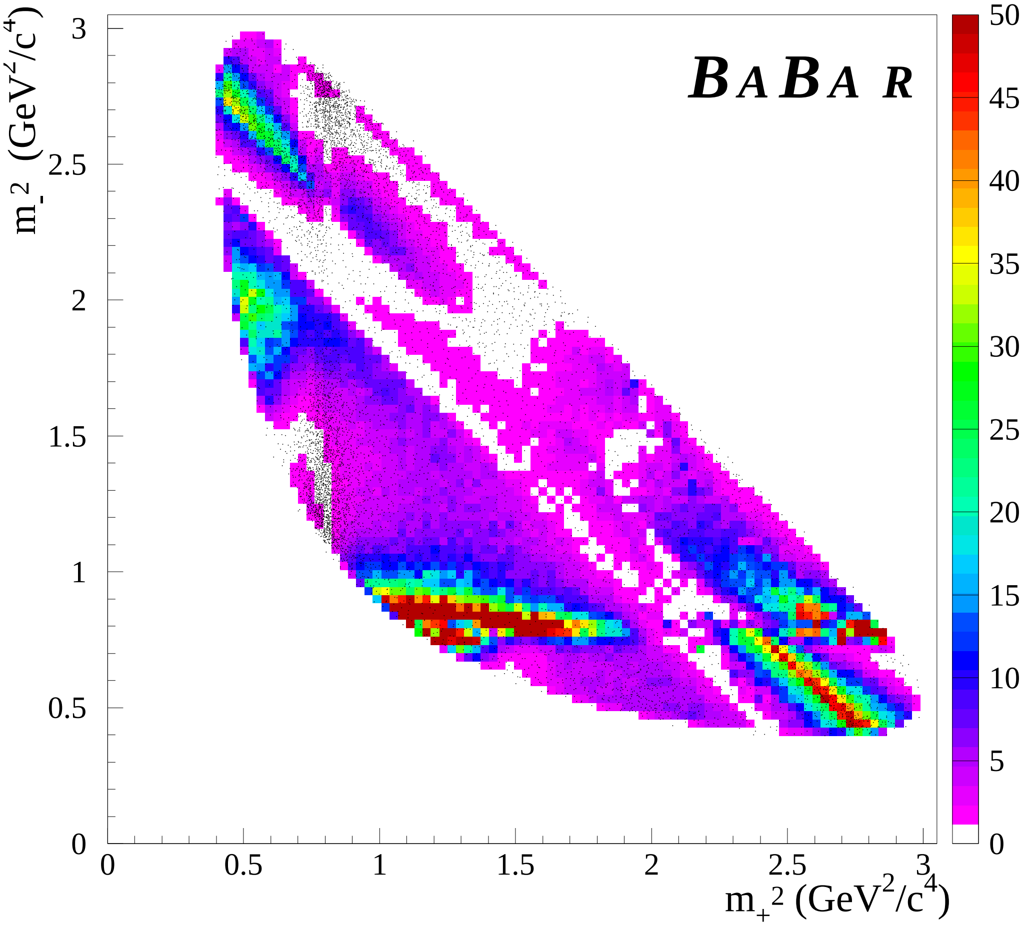

Figure 6.2: Sensitivity to γ across the Dalitz plot. Each event is weighted by the value of the second derivative of the log-likelihood with respect to γ. The black points correspond to the same events without any weighting.

CP parameter	$B^{\mp} \rightarrow \tilde{D}^{(*)0} K^{\mp}$
$x_- \equiv Re(r_{B-} e^{i\theta_-})$	$0.041 \pm 0.059 \pm 0.018 \pm 0.011$
$y_- \equiv Im(r_{B-} e^{i\theta_-})$	$0.056 \pm 0.071 \pm 0.007 \pm 0.023$
$x_+ \equiv Re(r_{B+} e^{i\theta_+})$	$-0.072 \pm 0.056 \pm 0.014 \pm 0.029$
$y_+ \equiv Im(r_{B+} e^{i\theta_+})$	$-0.033 \pm 0.066 \pm 0.007 \pm 0.018$
$x_-^* \equiv Re(r_{B-}^* e^{i\theta_-^*})$	$-0.106 \pm 0.091 \pm 0.020 \pm 0.009$
$y_-^* \equiv Im(r_{B-}^* e^{i\theta_-^*})$	$-0.019 \pm 0.096 \pm 0.022 \pm 0.016$
$x_+^* \equiv Re(r_{B+}^* e^{i\theta_+^*})$	$0.084 \pm 0.088 \pm 0.015 \pm 0.018$
$y_+^* \equiv Im(r_{B+}^* e^{i\theta_+^*})$	$0.096 \pm 0.111 \pm 0.032 \pm 0.017$

Table 6.2: *CP*-violating parameters $x_{\mp}^{(*)}$, $y_{\mp}^{(*)}$ obtained from the *CP* fit to the $B^{\mp} \rightarrow \tilde{D}^{(*)0} K^{\mp}$ samples. The first error is statistical, the second is the experimental systematic uncertainty and the third is the systematic uncertainty associated with the Dalitz model.

6.5 Results of CP parameters

Using an integrated luminosity of 316.3 fb^{-1}, we have performed a Dalitz plot analysis of $B^- \rightarrow D^{(*)0} K^-$, with $D^* \rightarrow D^0\pi^0, D^0\gamma$, $D^0 \rightarrow K_S\pi^+\pi^-$ decays, obtaining the following results (Summarized in Table 6.2). Here $\theta_{\pm}^{(*)} = \delta^{(*)} \pm \gamma$, with γ the CKM weak phase, $\delta^{(*)}$ the strong phase of the $B^- \rightarrow D^{(*)0} K^-$ decay, and ${r_B}^{(*)}$ the absolute value of the ratio of the corresponding $A(b \rightarrow u)$ and $A(b \rightarrow c)$ amplitudes, $r_B = |A(b \rightarrow u)/A(b \rightarrow c)|$. The first errors are statistical, the second are experimental systematics, and the third are due to the Dalitz model assumptions. Figure. 6.3 shows the Dalitz plot distribution for $B^{\mp} \rightarrow \tilde{D}^0 K^{\mp}$, $B^{\mp} \rightarrow \tilde{D}^{*0}(\tilde{D}^0\pi^0) K^{\mp}$, $B^{\mp} \rightarrow \tilde{D}^{*0}(\tilde{D}^0\gamma) K^{\mp}$, separately for B^- and B^+.

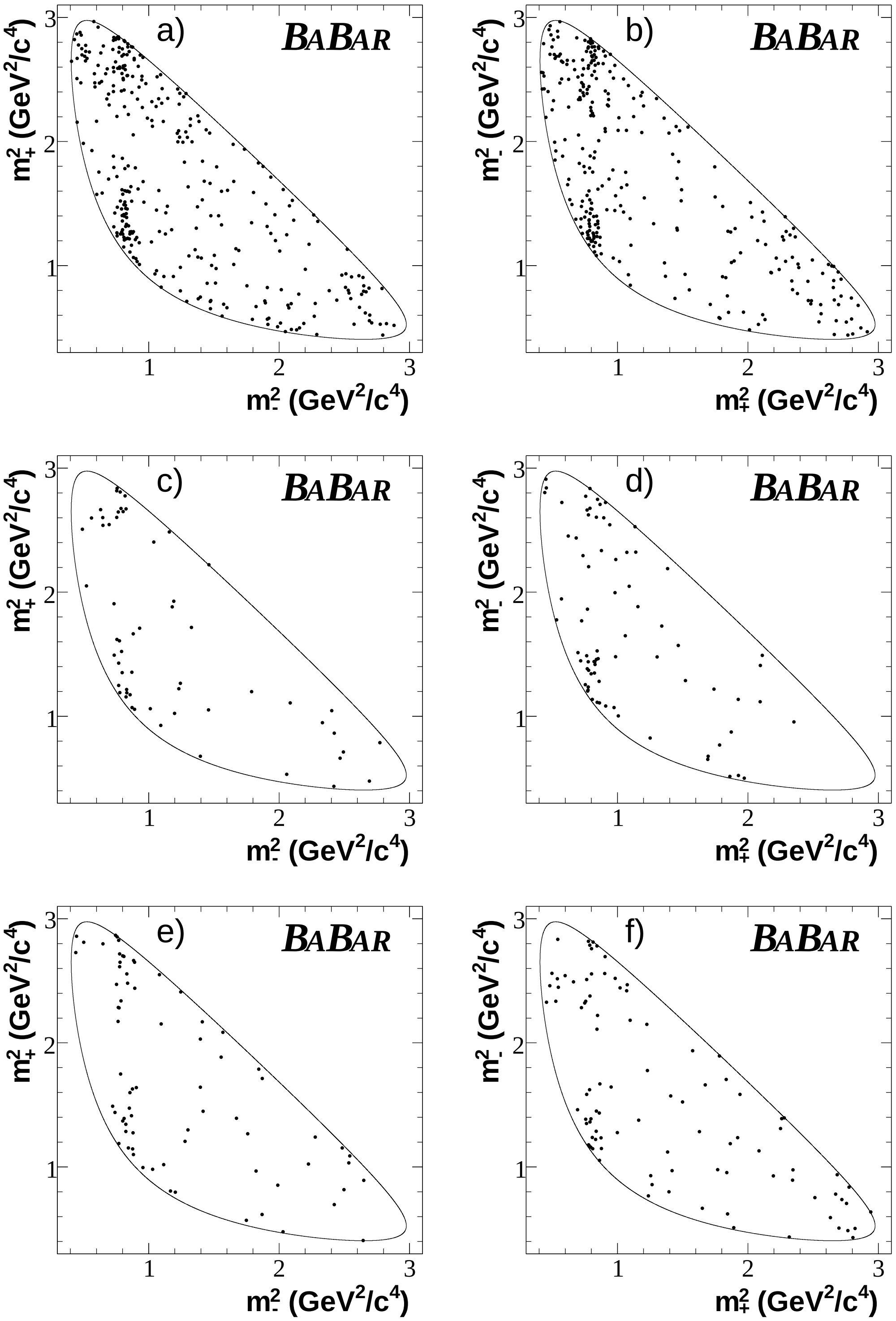

Figure 6.3: The $D^0 \to K_S^0\pi^+\pi^-$Dalitz distributions for (a,b) $B^\mp \to \tilde{D}^0K^\mp$, (c,d) $B^\mp \to \tilde{D}^{*0}(\tilde{D}^0\pi^0)K^\mp$, and (e,f) $B^\mp \to \tilde{D}^{*0}(\tilde{D}^0\gamma)K^\mp$, separately for (a,c,e)$B^-$ and (b,d,f)B^+. The requirements $m_{\rm ES} > 5.272$ GeV/c^2 and $|\Delta E| < 30$ MeV have been applied to reduce the background contamination.

CP parameter	$B^{\mp} \rightarrow \tilde{D}^{(*)0} K^{\mp}$
r_B	< 0.142
r_B^*	0.110 ± 0.090 (stat.) ± 0.019 (syst.) ± 0.024 (model)
δ_B	118 ±64 (stat.) ± 21 (syst.) ± 28 (model)
δ_B^*	-62 ±59 (stat.) ± 16 (syst.) ± 13 (model)
γ	92 ±41 (stat.) ± 10 (syst.) ± 13 (model) .

Table 6.3: *CP*-violating parameters $r_B, r_B^*, \delta_B, \delta_B^*, \gamma$ extracted from frequentist (Neyman) procedure in $B^{\mp} \rightarrow \tilde{D}^{(*)0} K^{\mp}$ samples. The first error is statistical, the second is the experimental systematic uncertainty and the third is the systematic uncertainty associated with the Dalitz model.

6.5.1 Frequentist interpretation

In order to extract $\gamma, r_B, \delta_B, r_B^*, \delta_B^*$, a frequentist (Neyman) procedure [20] has been adopted to interpret the measurement of the *CP* parameters $(x_{\mp}^{(*)}, y_{\mp}^{(*)})$ reported in Table 6.2 in terms of confidence regions on $\mathbf{p} = (\gamma, r_B, \delta_B, r_B^*, \delta_B^*)$. Using a large number of pseudo-experiments with probability density functions and parameters as obtained from the fit to the data but with many different values of the *CP* parameters, a multivariate Gaussian parameterization of the PDF of $(x_{\mp}^{(*)}, y_{\mp}^{(*)})$ as a function of $\mathbf{p}$ is constructed which takes into account the statistical and systematic correlations. For a given $\mathbf{p}$, the five-dimensional confidence level $\mathcal{C} = 1 - \alpha$ is calculated by integrating over all points in the fit parameter space closer (larger PDF) to $\mathbf{p}$ than the fitted data values. The one- (two-) standard deviation region of the *CP* parameters is defined as the set of $\mathbf{p}$ values for which α is smaller than 3.7% (45.1%). The corresponding one-standard-deviation values are listed in Table 6.3.

Figure 6.5 show the r_B–γ constraints for both $B^- \rightarrow D^0 K^-$and $B^- \rightarrow D^{*0} K^-$mode,

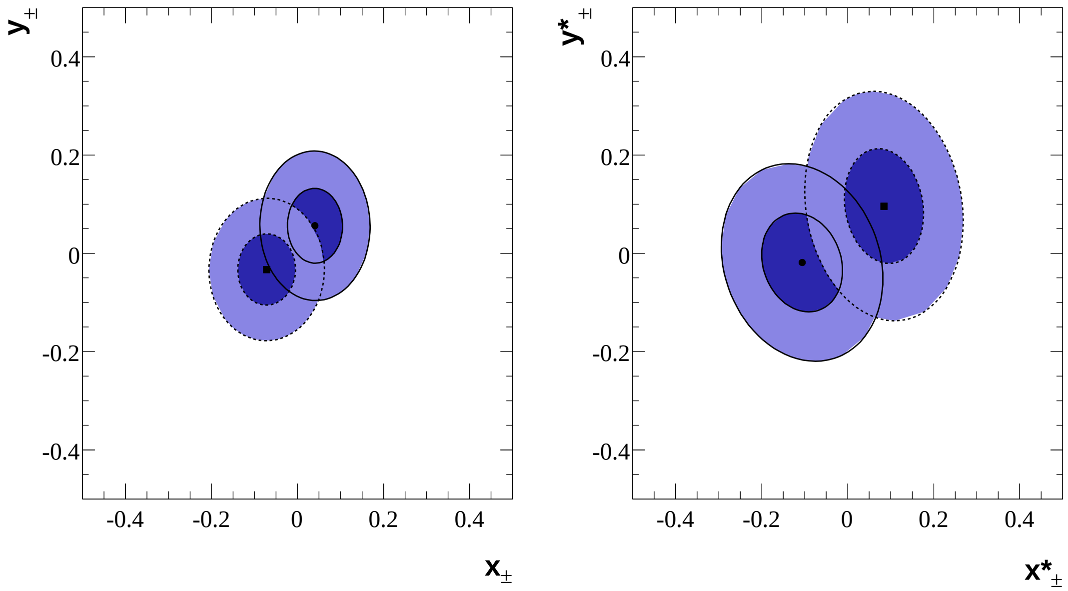

(a)

(b)

Figure 6.4: 39.3% (dark blue) and 86.5% (bright blue) 2-dimensional confidence-level contours in the $(x^{(*)}, y^{(*)})$ cartesian fit parameter space for $B^- \to D^0K^-$(a) and $B^- \to D^{*0}K^-$(b) events. Solid (dotted) contours are for B^- (B^+) decays.

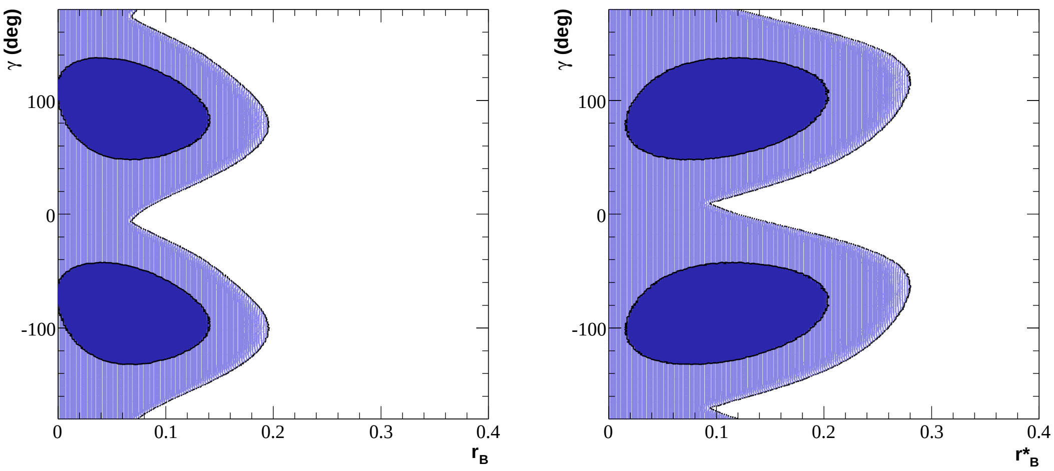

(a) (b)

Figure 6.5: Two-dimensional projections in the $r_B - \gamma$ and r_B^* planes of the five-dimensional one- (dark) and two- (light) standard deviation regions, for (a) $B^- \to D^0 K^-$and (b) $B^- \to D^{*0} K^-$events

including statistical and systematic uncertainties. The region of 1 (2)σ-equivalent 5D-ellipsoid corresponds to the one where $\alpha(\mathbf{p})$ is smaller than 3.7% (45.1%).

6.6 Experimental systematic uncertainties

In the following subsections each systematic uncertainty contribution in the cartesian coordinate space is described. Table 6.4 summarizes the main systematic uncertainties for the combined measurement of the $B^- \to D^{(*)0} K^-$modes. In all cases, each contribution to the systematic uncertainty is taken as the difference between the central values of the nominal and alternative fits.

Source	x_-	y_-	x_+	y_+	x^*_-	y^*_-	x^*_+	y^*_+
$m_{\rm ES}$, ΔE, $\mathcal{F}$ shapes	0.002	0.004	0.003	0.004	0.011	0.012	0.008	0.008
Real D^0 fractions	0.002	0.000	0.000	0.000	0.002	0.003	0.002	0.016
Fraction of right sign D^0's	0.008	0.002	0.002	0.002	0.005	0.005	0.001	0.022
Efficiency in the Dalitz plot	0.014	0.000	0.013	0.001	0.001	0.002	0.000	0.001
Background Dalitz shape	0.006	0.003	0.001	0.004	0.012	0.015	0.009	0.009
Dalitz amplitudes and phases	0.004	0.004	0.004	0.004	0.008	0.008	0.008	0.008
$B^- \to D^{*0}K^-$ cross-feed	0.000	0.000	0.000	0.000	0.004	0.001	0.004	0.004
CP violation in $D\pi$ & $B\overline{B}$ bkg	0.000	0.000	0.000	0.000	0.005	0.002	0.002	0.005
Total experimental	0.018	0.007	0.014	0.007	0.020	0.022	0.015	0.032
D^0 Dalitz model	0.011	0.023	0.029	0.018	0.009	0.016	0.018	0.017
Total	0.021	0.024	0.032	0.019	0.021	0.027	0.023	0.036

Table 6.4: Summary of the systematic error on the *CP* parameters $x_\mp$, $y_\mp$, $x^*_\mp$, and $y^*_\mp$.

6.6.1 General systematics from shape variables

$m_{\rm ES}$, ΔE and Fisher shapes

The effect of fixing the PDF shapes in the *CP* fit has been evaluated by performing a simultaneous fit varying the PDF shape parameters in additional to the *CP* parameters in cartesian coordinates. The fit is performed simultaneously to the $B^- \to D^{(*)0}K^-$and $B^- \to D^{(*)0}\pi^-$control sample, once with the shapes parameters fixed and again with the shapes varied. The systematic uncertainty is taken as the difference in quadrature of the statistical errors reported by the two fits.

$m_{\rm ES}$ endpoint

The $m_{\rm ES}$ endpoint in the ARGUS parameterization is fixed to 5.290 GeV/c^2 in the nominal fit. To account for its uncertainty we repeated the shapes and *CP* fits by varying its value by ±0.5 MeV/c^2.

Fraction of peaking $B\overline{B}$ background

Another potential systematic error is the estimation of the fraction of $B\overline{B}$ background peaking in ΔE. In the nominal fit, we use the values found in a large sample of $B\overline{B}$ Monte Carlo events where the two B mesons are allowed to decay according to their nautral branching fractions. We varied these fractions between 0 and 0.10 to account the systematics.

The fraction of $B\overline{B}$ background peaking in m_{ES} is left floated in the nominal fit, so the uncertainty is included in the statistical error. We have verified that the m_{ES} peaking fraction found in the data is consistent within errors with that found in the MC. The effect of fixing the parameterization (from the Monte Carlo estimate) for m_{ES} and ΔE was found to be negligible.

PEP-II boost

In the nominal fit we use a momentum-dependent ΔE PDF that relates on an event-by-event basis the ΔE for $B^- \to D^{(*)0}K^-$and $B^- \to D^{(*)0}\pi^-$events. The boost is determined online on-line at 10-minute intervals [18] using $e^+e^- \to \mu^+\mu^-$ events. An uncertainty due to the knowledge of the absolute value of the boost has been assigned by varying it ±0.5%. Again, the systematics was found to be negligible.

6.6.2 Background composition

Fraction of real D^0

The fraction of real D^0 has been estimated from data and Monte Carlo as explained in Sec. 5.2. The uncertainty due to the fraction of real D^0's in continuum background is estimated by varying this parameter within its statistical error from the D^0 mass fit on data, and independently using the central value from the data, and then repeating the CP fit. For $B\overline{B}$ background the estimate is performed by varying the fraction within its statistical error from the D^0 mass fit on data and taking the maximum variation.

Fraction of D^0 with correct flavor tagging

The fraction of right sign (RS) D^0 is taken from MC simulation. A value of 0.5 (no flavor-charge correlation) is assumed instead of the nominal values to estimate the systematic error.

6.6.3 Systematics from Dalitz shapes

Dalitz Plot efficiency

The reconstruction efficiency as a function of the point in the Dalitz plane has been evaluated and parametrized using a 3rd-order 2-dimensional symmetric polynomial function as described in Sec.5.5. To estimate the systematic error from the Dalitz efficiency, the nominal CP fit was repeated assuming a flat distribution instead of the nominal 3rd order polynomial parameterization.

Dalitz shape for combinatorial background

The Dalitz shape for combinatorial background (without any real D^0) from $q\bar{q}$ and $B\overline{B}$ background is taken from generic Monte Carlo after removal of the true D^0 component. The systematic uncertainty is estimated from the difference in the *CP* parameters using the shapes estimated from events in the D^0 mass window that lie in the $m_{\rm ES}$ sideband.

6.6.4 Other systematics

Cross-feed among the samples

Our monte carlo studies show that there is an overlap between the $D^0\pi^0$ and $D^0\gamma$ channels at the 2-3% level in the $B^- \to D^{*0}K^-$ modes. Also, to reduce the amount of cross-feed of $D^0\pi^0$ in $D^0\gamma$ we removed from the $D^0\gamma$ sample the common events with the $D^0\pi^0$ sample ($D^0\pi^0$ veto). The effect of neglecting the remaining 4.8 cross-feed events in the *CP* fit has been evaluated by introducing an additional background component to the $D^0\gamma$ PDF.

CP violating effect in $D\pi$ and $B\overline{B}$ background

To account for any bias due to a possible contribution from *CP* violating effects in $D\pi$ and $B\overline{B}$ backgrounds, we repeated the *CP* fit by introducing an independent set of $D\pi$ and $B\overline{B}$ cartesian parameters. In the case of the $D\pi$ background the fit was repeated using for $(x_\pm, y_\pm)$ and $(x^*_\pm, y^*_\pm)$ the values obtained by fitting the $B^- \to D^{(*)0}\pi^-$control samples. For $B\overline{B}$ background we allow them to float in data, as we do not have corresponding control samples.

6.6.5 Systematics from the Dalitz model

Statistical errors on Dalitz amplitudes and phases

The phases and amplitudes of the Dalitz model are fixed to the values found from the fit to the high statistics $D^{*+} \to D^0\pi^+_s$ sample. Although the effect coming from the statistical errors on the Dalitz amplitudes and phases should be very small, we estimated its effect by performing a simultaneous $B^- \to D^{(*)0}K^-$and $D^{*+} \to D^0\pi^+_s$ fit with all these parameters floated. The difference of central values are consistent with the quadratic difference of the statistical error.

Limited mass resolution

The nominal Dalitz model assumes perfect mass resolution. Given that all the resonances present in the $D^0 \to K^0_S\pi^+\pi^-$ decay are quite wide compared to the estimated mass resolution (about 4 MeV/c^2), the effect should be completely negligible. Only the $\omega(782)$ has an intrinsic width (8 MeV/c^2) comparable to the mass resolution, but the sensitivity of the *CP* parameters in this mode is suppressed. The studies show that the systematic uncertainty is neglectable in this case.

Dalitz model systematic uncertainties

The largest single contribution to the systematic uncertainties in the CP parameters comes from the choice of the Dalitz model used to describe the $D^0 \to K_S^0\pi^+\pi^-$decay amplitude. The breakdown of the model systematics is described in next section.

6.7 Dalitz model systematic uncertainties

To estimate the uncertainty arising from our choice of Dalitz model, eight alternative models have been considered. Our alternative models are constructed based on the following arguments:

- **$\pi\pi$ S-wave**

  The isobar model has two low-mass board σ scalars. The σ scalars are simply introduced in an ad-hoc way to improve the quality of the fit and their existence remains controversial. It is also well known that the isobar assumption violates the unitary condition. An alternative model is employed using K-matrix fit for $D^0 \to K_S^0\pi^+\pi^-$which requires that the $\pi\pi$ phase shift from $\pi\pi$ scattering data is consistent with the production environment. The model with $\pi\pi$ S-wave described by a K-matrix used as systematic uncertainty evaluation is described in Ref. [45].

- **$K\pi$ S-wave LASS/BW parameterization**

In *BABAR*, $D^0 \to K_s\pi^+\pi^-$ [46] and E791 [26] data favors similar mass and width for the $K^{*0}(1430)$ using BW lineshape, and we use this parametrization in the nominal fit. The $K\pi$ S-wave LASS parametrization is used as an alternative model. LASS parameterization was introduced to describe the observed strong interference between the resonant and non-resonant components. However, as described in Sec. 3.9, the background component of this LASS parametrization is process and parameterization-dependent, so the LASS model is used only as a cross check to determine the systematic uncertainty from the $K\pi$ S-wave.

- **Helicity model and Zemach Tensor**

  As described in Sec. 3.5.1, the use of helicity model vs. Zemach tensor is related to the description of angular distribution of decay products of resonances and is not well settled in the literature. We used the helicity model as our choice of nominal model, so we use the Zemach tensor as an alternative model evaluation of the systematic uncertainty.

- $K^*(892)$ **parameters**

  The $K^*(892)$ resonance is the dominant contribution in the Dalitz plot analysis of $D^0 \to K_S^0\pi^+\pi^-$and the uncertainty on its mass and width can affect the Dalitz model. The mass and width are varied within their experimental uncertainties according to PDG, and from a direct measurement using *BABAR* data as an alternative. For $K^*(892)$, the mass and width have also been measured in

$B^+ \to J/\psi K^{*+}$ decays using a partial wave analysis. The results are compatible with the values obtained in the $D^0 \to K_S^0\pi^+\pi^-$sample.

- **Blatt-Weisskopf penetration factors**

  Blatt-Weisskopf penetration factors are the phenomenological corrections to resonances accounting for the finite size of the meson. We obtained the systematic uncertainty by varying the level of the penetration barrier (radius) within a large interval, $R \in [0, 10]\,\mathrm{GeV}^{-1}$.

6.7.1 The procedure to determine the model systematics

A sample of $B^\mp \to DK^\mp$ and $B^\mp \to D^{*0}K^\mp$ signal events that is one hundred times larger than the measured signal yields in data is generated. To obtain the systematic uncertainty, alternative *CP* parameters are extracted by fitting the generated Dalitz plot distributions to one of the eight alternative models. We take as the systematic uncertainty of $(x_\mp, y_\mp)$ (similarly for $(x^*_\mp, y^*_\mp)$) associated with the i^{th} alternative model the difference between the *CP* parameters fitted using the alternative model $(x^i_\mp, y^i_\mp)$ and the nominal model $(x^0_\mp, y^0_\mp)$: $\Delta x^i_\mp = x^i_\mp - x^0_\mp$, $\Delta y^i_\mp = y^i_\mp - y^0_\mp$. The total systematic uncertainty is computed as the sum in quadrature of the contribution from the alternative models: $\Delta x_\mp = \sqrt{\sum_{i=1}^{8} \Delta {x^i_\mp}^2}$, $\Delta y_\mp = \sqrt{\sum_{i=1}^{8} \Delta {y^i_\mp}^2}$. The systematic uncertainties are summarized in Figs. 6.6 and 6.7. Surprisingly, most of the Dalitz model systematics are negligible apart from the $K\pi$ S-wave. This is most likely due to the large sensitivity in the $K\pi$ system while the nature of $K\pi$ S-wave is least understood.

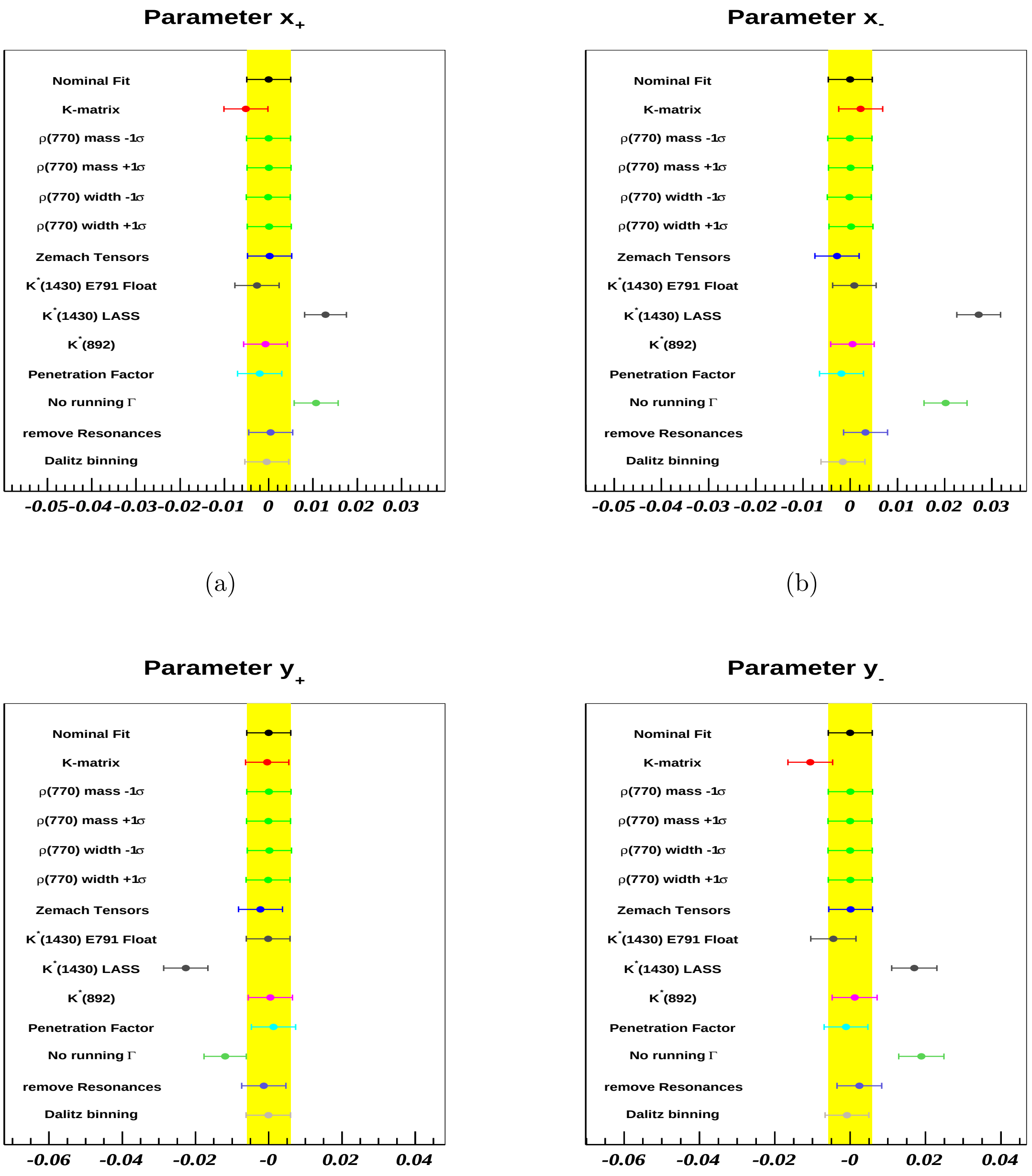

(a)

(b)

(c)

(d)

Figure 6.6: Breakdown of the residual of the $B^- \to D^0 K^-$ CP parameters fitting with the alternative Dalitz models with respect to the nominal model. The yellow vertical band shows the statistical error for the nominal model.

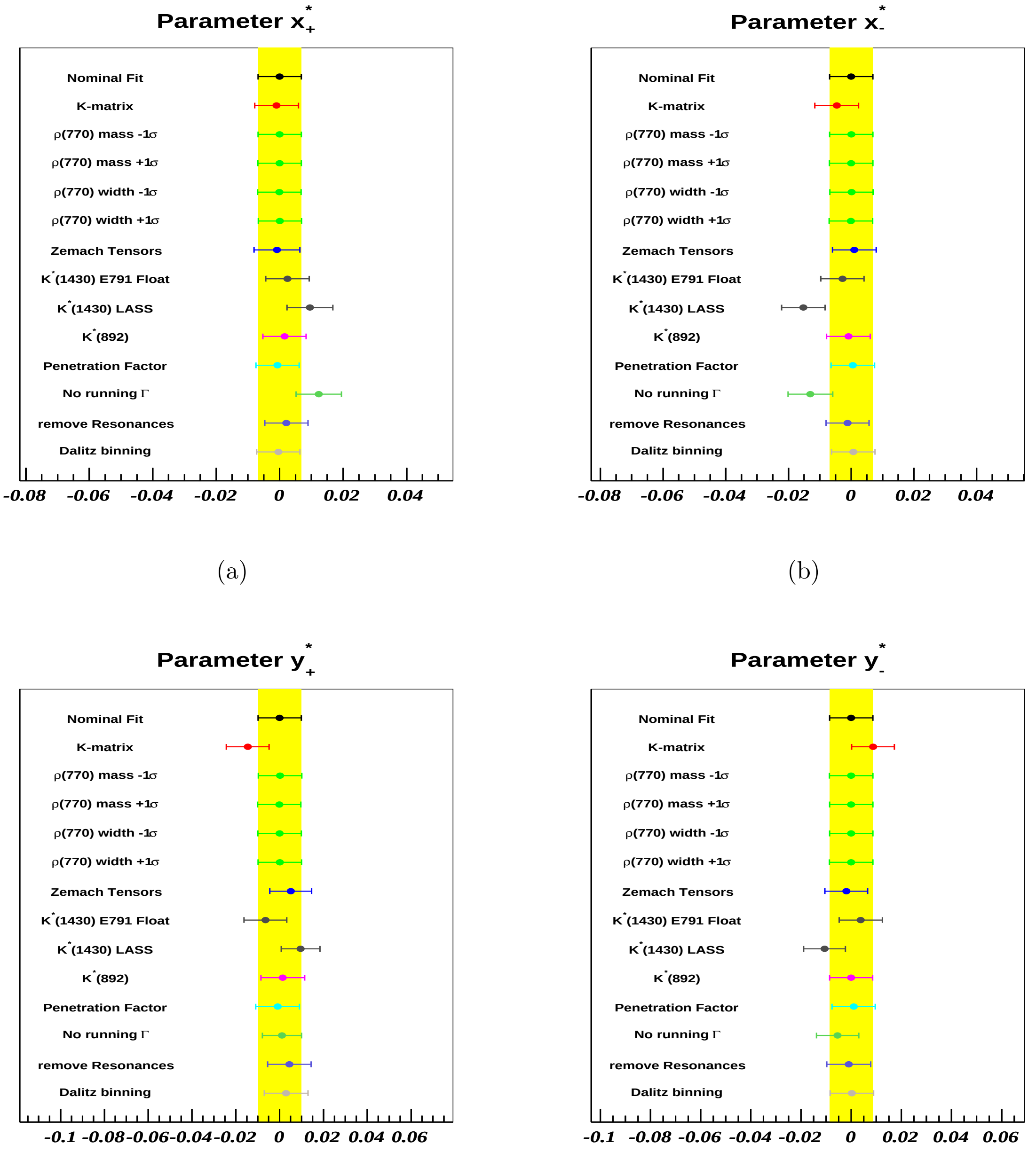

(a) (b)

(c) (d)

Figure 6.7: Breakdown of the residual of the $B^- \to D^{*0}K^-$ CP parameters fitting with the alternative Dalitz models with respect to the nominal model. The yellow vertical band shows the statistical error for the nominal model.

Chapter 7

Summary and Future Outlook

7.1 Constraint on the ($\bar{\rho}$, $\bar{\eta}$) plane

The results presented in Sec. 6.5 give a direct measurement of γ with better sensitivity than the GLW and ADS methods. The left in Fig. 7.1 shows a comparison of the total γ distribution of *BABAR* results from the Dalitz method and ADS+GLW methods separately, where it is seen that the main sensitivity comes from the Dalitz method. Figure 7.2 shows the constraint on the ($\bar{\rho}$, $\bar{\eta}$) plane using the angle measurements alone. Although the error is large compared to the measurements of β and α, the analysis technique reported in this thesis represents the first direct measurement of γ.

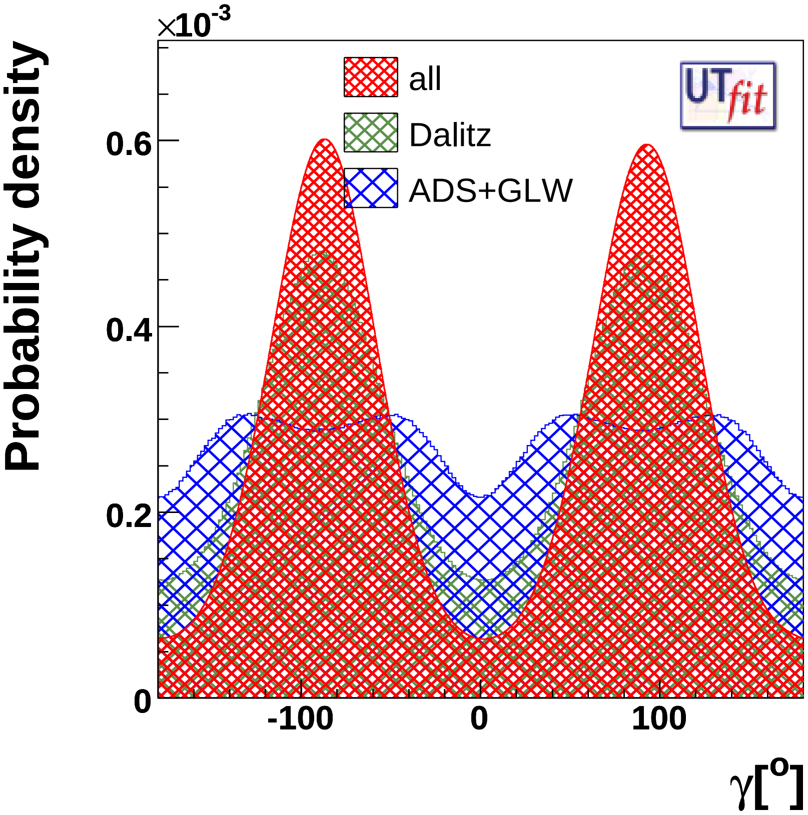

Figure 7.1: Comparison of the combined constrain on γ from *BABAR* results using the Dalitz and ADS+GLW methods alone.

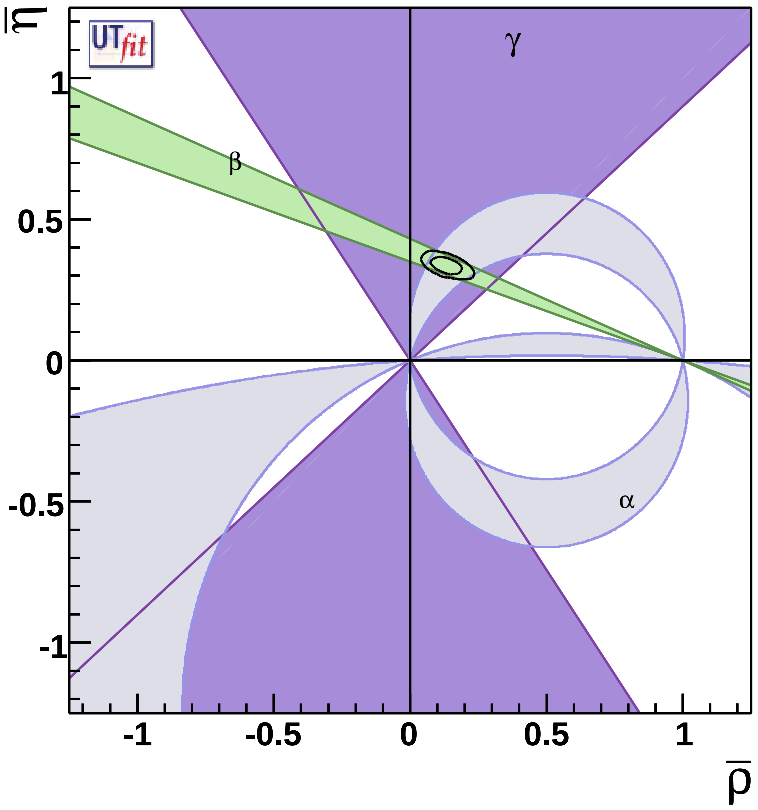

Figure 7.2: The world average bound on ($\bar{\rho}$, $\bar{\eta}$) from the CKM angle measurements alone.

7.2 Future outlook

Although both *BABAR* [38] and Belle [47][48] have measured γ using the $B^- \rightarrow D^0 K^-$Dalitz analysis, the current measurement of this angle is still dominated by statistical uncertainties. The next largest contribution to the error is coming from the Dalitz model. In this thesis the K-matrix model is developed to study the effect of the Dalitz model uncertainty on the $\pi^+\pi^-$ S-wave, which is the least understood component of the analysis. Figure 7.3 shows the projected errors on γ for both the Dalitz method alone and the combination of all methods. The points correspond to the values obtained from toy Monte Carlo simulations, and the curve is the smoothed extrapolation obtained from a fit assuming the error on γ scales likes $1/\sqrt{\int Ldt}$, where L is the integrated luminosity. The horizontal band is the Dalitz model uncertainty under the mild assumption that the error will be $\approx 6^\circ$. From the Monte Carlo simulation, the Dalitz model systematic uncertainty will not be a limiting factor, either for the Dalitz method alone or combination of all the methods.

7.2.1 Future improvements

There are several ways to improve the measurement of γ besides simply increasing the luminosity, which we list below:

- the model-independent approach;
- using $\Psi(3770) \rightarrow D\bar{D}$ from CLEO-c;

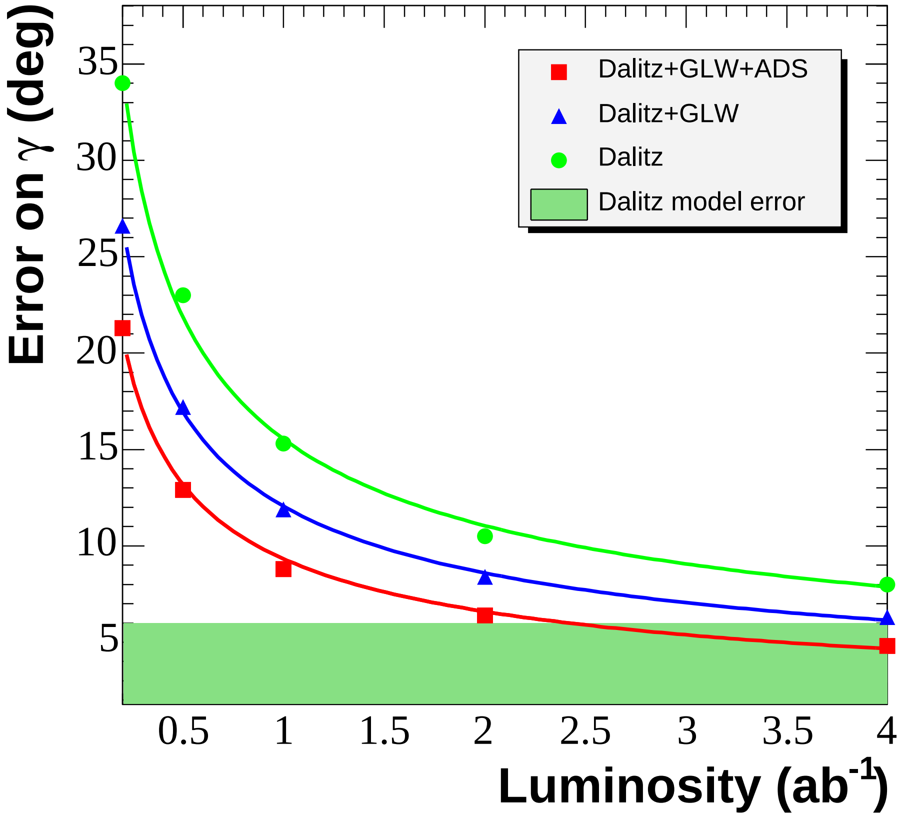

Figure 7.3: Projected errors on γ for the combination of several methods and all decay modes described in the text, assuming $r_B = 0.1$

- using $B_s \to D_s K$;

The model-independent approach

In the model-independent approach [17], allows γ to be extracted directly using $B^- \to D^0 K^-$ events without any model assumption of the Dalitz model by binning the Dalitz plot. Although this technique minimizes the model systematic uncertainty, it requires much larger data sets than are currently available at the B-factories.

Using $\Psi(3770) \to D\bar{D}$ from CLEO-c

CLEO-c [49] is a charm factory operating at the $\psi(3770)$, which primarily decays into $D\bar{D}$. The quantum correlations in the $\psi(3770) \to D\bar{D}$ system provide a unique way to determine the CP eigenstate by tagging the CP flavor of one of the D mesons. Studying the CP-tagged Dalitz plot allows a model independent determination of the relative D^0 and $\bar{D}^0$ phase at each point in the Dalitz plane.

Consider $D^0 \to K^0_S\pi^+\pi^-$ decay which proceeds through intermediate states that are $CP+$ eigenstates, such as $K^0_S f_0$, $CP-$ such as $K^0_S\rho$, and flavor eigenstates such as $K^{*-}\pi^+$. The Dalitz plots for $\psi(3770) \to D^0\bar{D}^0 \to S_+K^0_S\pi^+\pi^-$ and $\psi(3770) \to D^0\bar{D}^0 \to S_-K^0_S\pi^+\pi^-$ will be distinct, and the Dalitz plot for the untagged sample $\psi(3770) \to D^0\bar{D}^0 \to XK^0_S\pi^+\pi^-$ will be different from that observed with uncorrelated D mesons from continuum production at ~ 10 GeV. A simultaneous fit to $CP+$, $CP-$, and flavor tag samples with BW/K-matrix hybrid models can reduce the model-dependent systematic error on γ to a few degrees. Furthermore, a completely model-independent result can be obtained from a binned analysis of the CP-tag and flavor-tag Dalitz plots.

Using $B_s \rightarrow D_s K$

This is the analog of using time-dependent measurement of $B_d \rightarrow J/\psi K_S$ to measure the angle β [11][50]. Even though we could operate PEP-II at $\sqrt{s} = M(\Upsilon(5S))$, this method is still not feasible due to the small decay time difference between two B_s meson [51]. However, this method should be accessible in LHC_b [1], where the boost is large. This method is theoretically clean since it only involves tree-level decay amplitudes with negligible hadronic uncertainties.

7.3 Conclusion

In this thesis, γ is measured directly using a Dalitz plot analysis of $D^0 \rightarrow K^0_S \pi^+ \pi^-$ in $B^- \rightarrow D^0 K^-$ decays. Using a sample of 347 million $B\bar{B}$ events collected by the *BABAR* detector, the following value of γ is obtained:

$$\gamma = 92 \pm 41 \pm 11 \pm 12^\circ$$

where the first error is statistical, the second is the experimental systematic uncertainty and the third reflects the Dalitz model uncertainty.

Accurate measurements of the CKM angle γ currently require a Dalitz plot analysis of $D^0 \rightarrow K_S^0\pi^+\pi^-$, which has led to the need for a comprehensive study of hadron spectroscopy in both $\pi\pi$ and $K\pi$ system. In the first model the Dalitz plot amplitude is parameterized as a sum of Breit-Wigner resonances which requires two ad-hoc scalar resonances, σ and $\sigma^{'}$, to describe the data. This leads to large model uncertainty due to the controversial existence of the low mass scalar $\sigma(500)$. It is well known that the Breit-Wigner description, is only valid in the case of narrow, isolated resonances. As Breit-Wigner structure is not seen from the $\pi\pi$ scattering experiment, a proper treatment of $\pi\pi$ S-wave is needed.

This leads to a K-matrix formalism to describe the $\pi\pi$ S-wave. K-matrix has various advantages that it can handle strongly overlapping resonances and coupled channels can be handled simultaneously, which is indeed the case in the $D^0 \rightarrow K_S^0\pi^+\pi^-$ decay. This alternative parameterization is used to evaluate the contribution to the systematic uncertainty in the $\pi\pi$ S-wave, which is found to be 3°.

The measurement of the CKM angle γ helps us to understand the physics beyond the standard model. In the $B^- \rightarrow D^0K^-$ decay are dominated by tree-level process, any extension of standard model must fulfill the constraints in the $(\bar{\rho} - \bar{\eta})$ plane formed by the combination of γ and V_{ub}/V_{cb}, which are also dominated by tree-level processes. This helps theorist to identify the correct new physics model.

With higher and higher statistics the model independent approach will be feasible for the measurement of γ. In this perspective CLEO-c data will help to narrow down the model uncertainty.

Finally, hadron spectroscopy, in particular in scalar mesons, remains one of the long-standing puzzles despite the availability of high-statistics data. The existence of the $\sigma(500)$, $\kappa(800)$ remains controversial today. In this thesis, the relationship between the complex pole position of a resonance and its mass and width is explained, and an illustration of the fact that the Breit-Wigner parameters are highly model-dependent and should not be taken as fundamental properties of the resonance is included. From the author's perspective, the model-independent complex-pole position analysis of *BABAR* data should shed light on the existence of the $\sigma(500)$ and $\kappa(800)$ scalar resonances.

Appendix A

Miscellaneous Formulae

A.1 Breit-Wigner – partial wave phase shifts

More formally, the non-relativistic BW formula arises in the context of the partial wave expansion in scattering theory. The l-th partial wave is given by

$$a_l = e^{i\delta_l} \sin \delta_l = \frac{1}{\cot \delta_l - i}, \quad \text{(A.1)}$$

and when the phase shift δ_l is near $\pi/2$ at an energy E $\sim$ M, resonant scattering occurs. Define $M_R^2 = E(\delta = \pi/2)$ and expanding the partial-wave amplitude about the resonance energy:

$$\cot \delta(E) \approx \cot \delta(E_R) + (E - E_R)\tfrac{d}{dE} \cot \delta(E)|_{E=E_R} = (E - E_R)(-\frac{\Gamma}{2}), \quad \text{(A.2)}$$

where $\frac{\Gamma}{2}$ is defined as the first derivative of $\cot\delta$. From this we obtain the BW formula:

$$\cot\delta_l(E) = \frac{\frac{\Gamma}{2}}{(E_R - E) - i\frac{\Gamma}{2}}. \tag{A.3}$$

A.2 Gounaris-Sakurai(GS) parameterization

The propagator in GS parameterization can be written as:

$$\frac{1 + d \cdot \Gamma_R/m_R}{s - m_R^2 - \delta m^2(s) + i\, m_R \Gamma_R(s)}, \tag{A.4}$$

where

$$\delta m^2(s) \;=\; \Gamma_R \frac{m_R^2}{k_\pi^3(m_R^2)} \left[k_\pi^2(s) \left(h(s) - h(m_R^2) \right) + (\, m_R^2 - s)\, k_\pi^2(m_R^2) \left. \frac{dh}{ds} \right|_{s=m_R^2} \right] \tag{A.5}$$

and where $k_\pi(s)$ is the pion momentum in the resonance rest frame.

$$h(s) \;=\; \frac{2}{\pi} \frac{k_\pi(s)}{\sqrt{s}} \ln\left(\frac{\sqrt{s} + 2k_\pi(s)}{2m_\pi} \right) \tag{A.6}$$

with

$$dh/ds|_{m_R^2} \;=\; h(m_R^2) \left[(8k_\pi^2(m_R^2))^{-1} - (2m_R^2)^{-1} \right] \,+\, (2\pi m_R^2)^{-1}. \tag{A.7}$$

The parameter $d = f(0)/(\Gamma_R m_R)$ is the normalization factor and it is found to be [23]

$$d \;=\; \frac{3}{\pi}\frac{m_\pi^2}{k_\pi^2(m_R^2)}\ln\left(\frac{m_R + 2k_\pi(m_R^2)}{2m_\pi}\right) + \frac{m_R}{2\pi\, k_\pi(m_R^2)} - \frac{m_\pi^2 m_R}{\pi\, k_\pi^3(m_R^2)}. \tag{A.8}$$

This becomes the standard parameterization for $\rho(770)$ resonances.

A.3 Modification of PDF for DK^* events

Compared to $B^- \to D^{(*)0}K^-$, the decay $B^- \to D^0 K^{*-}$ is affected by an additional complication. Because the natural width of the K^{*-} is not small (∼50 MeV), interference with the non-resonant $B^- \to D^0(K\pi)^-_{\mathrm{non-K^*}}$ processes may not be negligible. This changes the relationships between the angle γ and the experimental observables, leading to additional modification of the PDF.

The amplitudes for the $B^- \to (D^0 X_s^-)_p$ and $B^- \to (\overline{D}^0 X_s^-)_p$ processes is given by

$$A(B^- \to (D^0 X_s^-)_p) = A_{cp} e^{i\delta_{cp}} \tag{A.9}$$

$$A(B^- \to (\overline{D}^0 X_s^-)_p) = A_{up} e^{i\delta_{up}} e^{-i\gamma} \tag{A.10}$$

$$A(D^0 \to f) = A_f e^{i\delta_f} \tag{A.11}$$

$$A(D^0 \to \bar{f}) = A_{\bar{f}} e^{i\delta_{\bar{f}}}\,, \tag{A.12}$$

where A_{cp}, A_{up}, A_f and $A_{\bar{f}}$ are real and positive. The index p indicates the position in the phase space of DX_s^-, and A_c, A_u, δ_c and δ_u generally vary as a function of p. The subscripts c and u refer to the $b \to c$ and $b \to u$ transitions, respectively. The amplitudes $A_{cp}e^{i\delta_{cp}}$ and $A_{up}e^{i\delta_{up}}e^{-i\gamma}$ generally include both the resonant $B^- \to D^0/\overline{D}^0K^{*-}$ processes and the non-resonant contributions. The amplitudes for the D^0 decay can generally include the case $D^0 \to$3-body (e.g., $D^0 \to K_S^0\pi^-\pi^+$). In this case $A_fe^{i\delta_f} = f(m_-^2, m_+^2)$ and $A_{\bar{f}}e^{i\delta_{\bar{f}}} = f(m_+^2, m_-^2)$, and now, A_f, $A_{\bar{f}}$, δ_f and $\delta_{\bar{f}}$ are functions of the Dalitz plot coordinates $m_\pm^2$, where m_-^2 and m_+^2 are the squared masses of the $K_S^0\pi^-$ and $K_S^0\pi^+$ combinations.

The amplitude for the process $B^- \to D[\to f]X_s^-$ can be written as

$$A(B^- \to (D[\to f]X_s^-)_p) = A_{cp}A_fe^{i(\delta_{cp}+\delta_f)} + A_{up}A_{\bar{f}}e^{i(\delta_{up}+\delta_{\bar{f}}-\gamma)}\,, \tag{A.13}$$

and the rate

$$\Gamma(B^- \to D[\to f]X_s^-) = \int dp \left(A_{cp}^2A_f^2 + A_{up}^2A_{\bar{f}}^2 + 2A_{cp}A_fA_{up}A_{\bar{f}}Re(e^{i(\delta_p+\delta_D-\gamma)})\right)\,, \tag{A.14}$$

where $\delta_p = \delta_{up} - \delta_{cp}$ and $\delta_D = \delta_{\bar{f}} - \delta_f$. The rate for the charge-conjugate mode is the one in Eq. A.14 with $\gamma \to -\gamma$. Analogously, the partial rates $\Gamma(B^- \to D^0X_s^-)$ and $\Gamma(B^- \to \overline{D}^0X_s^-)$ are

$$\Gamma(B^- \to D^0X_s^-) = \int dp\ A_{cp}^2\,, \tag{A.15}$$

$$\Gamma(B^- \to \overline{D}^0X_s^-) = \int dp\ A_{up}^2\,. \tag{A.16}$$

Following the same notation as in [52], we introduce the quantities r_s, k and δ_s, that will be useful in the following sections:

$$r_s^2 = \frac{\Gamma(B^- \to \overline{D}^0 X_s^-)}{\Gamma(B^- \to D^0 X_s^-)} = \frac{\int dp\ A_{up}^2}{\int dp\ A_{cp}^2}\,, \tag{A.17}$$

$$k e^{i\delta_s} = \frac{\int dp\ A_{cp} A_{up} e^{i\delta_p}}{\sqrt{\int dp\ A_{cp}^2\ \int dp\ A_{up}^2}}\,, \tag{A.18}$$

where $0 \leq k \leq 1$ for the Schwartz inequality and $\delta_s \in [0, 2\pi]$. In the limit of a $B \to$ 2-body decay, such as $B^- \to DK^-$, we have

$$\begin{aligned} & r_s \to r_B \equiv \frac{|A(B^- \to \overline{D}^0 K^-)|}{|A(B^- \to D^0 K^-)|}\,, \\ & \delta_s \to \delta_B \equiv \text{strong phase of } \frac{\mathrm{A(B^- \to \overline{D}^0 K^-)}}{\mathrm{A(B^- \to D^0 K^-)}}\,, \\ & k \to 1\,. \end{aligned} \tag{A.19}$$

In the case of the $D^0 \to K_S^0 \pi^+ \pi^-$ decay, $A_f e^{i\delta_f} = f(m_-^2, m_+^2)$ and $A_{\bar{f}} e^{i\delta_{\bar{f}}} = f(m_+^2, m_-^2)$. The amplitude for the process $B^\mp \to D[\to K_S^0 \pi^- \pi^+] X_s^\mp$ can be written as

$$A(B^\mp \to D[\to K_S^0 \pi^- \pi^+] X_s^\mp) = A_{cp} e^{i\delta_{cp}} f(m_\mp^2, m_\pm^2) + A_{up} e^{i\delta_{up} \mp \gamma} f(m_\pm^2, m_\mp^2)\,, \tag{A.20}$$

and the rate is

$$\begin{aligned}\Gamma(B^{\mp} \to D[\to K^0_S\pi^-\pi^+]X_s^{\mp}) &\propto |f_{\mp}|^2 + r_s^2|f_{\pm}|^2 + \\ &\quad 2kr_s\left\{\cos(\delta_s \mp \gamma)Re[f_{\mp}f^*_{\pm}] + \sin(\delta_s \mp \gamma)Im[f_{\mp}f^*_{\pm}]\right\} \\ &\equiv |f_{\mp}|^2 + r_s^2|f_{\pm}|^2 + \\ &\quad 2kr_s|f_{\mp}||f_{\pm}|\cos(\delta_s + \delta_D(m^2_{\mp}, m^2_{\pm}) \mp \gamma)\,,\end{aligned} \tag{A.21}$$

where $\delta_D(m^2_{\mp}, m^2_{\pm})$ is the strong phase difference between $f(m^2_{\pm}, m^2_{\mp})$ and $f(m^2_{\mp}, m^2_{\pm})$ and r_s, k and δ_s are defined in Eqs. A.17 and A.18. We have simplified the notation using $f_{\pm} \equiv f(m^2_{\pm}, m^2_{\mp})$ and $f_{\mp} \equiv f(m^2_{\mp}, m^2_{\pm})$. Let us stress that the parameterization given in Eq. A.21 includes both resonant and non-resonant $(K\pi)^{\mp}$ contributions, since the amplitudes in Eqs. A.9 and A.10 include both. The effective (and general) parameterization given in Eq. A.21 can be rewritten in terms of the cartesian coordinates

$$\begin{aligned}x_{s\pm} &= Re[kr_se^{i(\delta_s \pm \gamma)}]\,, \\ y_{s\pm} &= Im[kr_se^{i(\delta_s \pm \gamma)}]\,,\end{aligned} \tag{A.22}$$

as

$$\begin{aligned}\Gamma(B^{\mp} \to D[\to K^0_S\pi^-\pi^+]X_s^{\mp}) &\propto |f_{\mp}|^2 + r_s^2|f_{\pm}|^2 + \\ &\quad 2\left[x_{s\mp}Re[f_{\mp}f^*_{\pm}] + y_{s\mp}Im[f_{\mp}f^*_{\pm}]\right]\,.\end{aligned} \tag{A.23}$$

The measurement of γ in this analysis can be performed by extracting the terms proportional to r_s^2 and kr_s independently. It is accomplished by using Eq. A.24 and fitting simultaneously for $x_{s\mp}$, $y_{s\mp}$ and r_s^2. Since the experimental sensitivity to γ comes from the interference term (linear in r_s), we expect the effect of varying the r_s^2 factor to be quite small (as the terms quadratic in r_s are suppressed for r_s relatively small). This provides an easy way to extract directly the effective cartesian coordinates from data without any assumption about the non-resonant contribution and its interference with the resonant signal, with the additional advantage that both resonant and non-resonant decays contribute coherently to the sensitivity to γ.

Bibliography

[1] J. Rademacker, arXiv:hep-ex/0503001 (2005).

[2] J. H. Christenson, J. W. Cronin, V. L. Fitch, and R. Turlay, Phys. Rev. Lett. **13**, 138 (1964).

[3] R. N. Cahn, Rev. Mod. Phys. **68**, 951 (1996).

[4] L. Wolfenstein, Phys. Rev. Lett. **51**, 1945 (1983).

[5] H. Burkhardt et al., Phys. Lett. **B206**, 169 (1988).

[6] G. D. Barr et al., Phys. Lett. **B317**, 233 (1993).

[7] A. Alavi-Harati et al., Phys. Rev. Lett. **83**, 22 (1999).

[8] V. Fanti et al., Phys. Lett. **B465**, 335 (1999).

[9] B. Aubert et al., Phys. Rev. Lett. **93**, 131801 (2004).

[10] E. Barberio et al., arXiv:hep-ex/0603003 (2006).

[11] B. Aubert et al., Phys. Rev. Lett. **94**, 161803 (2005).

[12] K. Abe et al., arXiv:hep-ex/0507037 (2005).

[13] M. Bona et al., JHEP **07**, 028 (2005).

[14] M. Gronau and D. London., Phys. Lett. **B253**, 483 (1991).

[15] D. Atwood, I. Dunietz, and A. Soni, Phys. Rev. Lett. **78**, 3257 (1997).

[16] B. Aubert et al., Phys. Rev. **D72**, 032004 (2005).

[17] A. Giri, Y. Grossman, A. Soffer, and J. Zupan, Phys. Rev. **D68**, 054018 (2003).

[18] B. Aubert et al., Nucl. Instrum. Meth. **A479**, 1 (2002).

[19] R. H. Dalitz, Phil. Mag. **44**, 1068 (1953).

[20] S. Eidelman et al., Phys. Lett. B **592** (2004).

[21] E. M. Aitala et al., Phys. Rev. Lett. **86**, 770 (2001).

[22] S. Kopp et al., Phys. Rev. **D63**, 092001 (2001).

[23] G. J. Gounaris and J. J. Sakurai, Phys. Rev. Lett. **21**, 244 (1968).

[24] J. M. Blatt and V. F. Weisskopf, *Theoretical Nuclear Physics*, Dover Publications; New Ed edition, 1991.

[25] M. Ablikim et al., Phys. Lett. **B598**, 149 (2004).

[26] E. M. Aitala et al., Phys. Rev. Lett. **86**, 770 (2001).

[27] B.-S. Zou, arXiv:hep-ph/9611235 (1996).

[28] E. P. Wigner, Phys. Rev. **70**, 15 (1946).

[29] E. P. Wigner and L. Eisenbud, Phys. Rev. **72**, 29 (1947).

[30] R. Dalitz and S. Tuan, Ann Phys **10**, 307 (1960).

[31] I. J. R. Aitchison, CLARENDON-1-72 (1972).

[32] S. M. Flatte, Phys. Lett. **B63**, 224 (1976).

[33] D. Aston et al., Nucl. Phys. **B296**, 493 (1988).

[34] A. Rittenberg et al., Rev. Mod. Phys. **43**, S115 (1971).

[35] P. Soeding et al., Phys. Lett. **B39**, P104 (1972).

[36] M. Benayoun, H. B. O'Connell, and A. G. Williams, Phys. Rev. D **59**, 074020 (1999).

[37] B. Aubert et al., arXiv:hep-ex/0408088 (2004).

[38] B. Aubert et al., Phys. Rev. Lett. **95**, 121802 (2005).

[39] V. V. Anisovich and A. V. Sarantsev, Eur. Phys. J. **A16**, 229 (2003).

[40] J. M. Link et al., Phys. Lett. **B585**, 200 (2004).

[41] S. L. Adler, Phys. Rev. **137**, B1022 (1965).

[42] K. Abe et al., arXiv:hep-ex/0308043 (2003).

[43] H. Albrecht et al., Phys. Lett. **B241**, 278 (1990).

[44] A. Bondar and T. Gershon, Phys, Rev. D **70**, 091503 (2004).

[45] B. Aubert et al., arXiv:hep-ex/0507101 (2005).

[46] B. Aubert, arXiv:hep-ex/0607104 (2006).

[47] A. Poluektov et al., Phys. Rev. **D70**, 072003 (2004).

[48] A. Poluektov et al., Phys. Rev. **D73**, 112009 (2006).

[49] R. A. Briere et al., CLNS-01-1742 (2001).

[50] K. Abe et al., Phys. Rev. **D71**, 072003 (2005).

[51] A. Abulencia et al., arXiv:hep-ex/0609040 (2006).

[52] M. Gronau, Phys. Lett. **B557**, 198 (2003).